Universitat
Autònoma
de Barcelona

A Physics-Based Image Modelling of IVUS as a Geometric and Kinematics System.

A dissertation submitted by **Misael Darío Rosales Ramírez** at Universitat Autònoma de Barcelona to fulfill the degree of **Doctor en Informática**.

Bellaterra, July 29, 2005

Director: **Dra. Petia Radeva Ivanova**
Universitat Autònoma de Barcelona
Dept. Informàtica & Computer Vision Center

Centre de Visió
per Computador

This document was typeset by the author using $\LaTeX 2_\varepsilon$.

The research described in this book was carried out at the Computer Vision Center, Universitat Autònoma de Barcelona.

ISBN 84–922529–8–7

Printed by Ediciones Gráficas Rey, S.L.

A mi linda esposa Any,
a mis hijos Victor Hugo y Rosa María.

A los que siguen creyendo y apoyan a nuestros países latinoamericanos y a los que aun no creyendo en ellos, dan espacio para cultivar los signos modernos de sus ansiadas libertades.

Agradecimientos

Deseo agradecer a la Universidad de los Andes, Mérida Venezuela el apoyo económico que ha sustentado parte de esta investigación favoreciendo la formación científica de su planta profesoral. A la dirección del Centre de Visió per Computador en la persona del Dr. Juanjo Villanueva quien, con su lucha permanente, hace posible la existencia de este importante centro de investigación y desarrollo. A la Dra. Petia Radeva por su gentileza, dedicación, profesionalismo y especial entrega en estos años de trabajo mutuo. Al Grupo de Hemodinámica del Hospital Universitario "Germans Trias i Pujol" de Badalona, España, mi especial agradecimiento a la Dra. Josepa Mauri por permitirme agregarle a su agenda algunas tareas más, como si no tuviera ya suficientes, permitiéndome además el uso de su laboratorio. Asimismo al Dr.: Oriol Rodríguez por su cooperación en el diseño y consecución de algunos montajes experimentales. A mis amigos del CVC David Rotger, por su amistad y ayuda siempre oportuna, a Debora Gil por sus objetivas y acertadas críticas, a Fernando Vilariño, Oriol Pujol, Aura Hernández, David Masip, Jaume Amores, Agnés Borràs y Francesc Tous. Al personal del CVC en especial a Montse y a Pilar, a Raquel y a Joan Masoliver, a Ainhoa y Mari Carmen. A mis amigos de Cerdanyola, Gabriel Quiroz, Consuelo y Manolo, a Paquita, Antonio y Maribel, a Oscar y a Celeste, a todos ellos, por su solidaridad y amistad.

A mi hermosa familia y amigos de Venezuela por su sincera y siempre abnegada amistad así como a su larga y justificada espera. Deseo dar las gracias a *mi suegra Josefina*, por estar cerca de nosotros cuando más la hemos necesitado, distanciándose de su tierra para ocupar su tiempo en nosotros y en sus adorados nietos.

A mi linda esposa Any por su espera, solidaridad y su calma además de permitirme quererla tanto, a *Victor Hugo y Rosa María*, por sacrificar sin saberlo, hermosos tiempos de su niñez para alimentar estos saberes que son bastante ajenos a sus alegrías.

A los dueños de estos días y noches de paciencia y de sosobra, quienes soportan con esperanza y calma una intervención quirúrgica, por quienes todos estos apuntes y muchos otros estarán plenamente justificados, aunque nunca sabrán que les estoy eternamente agradecido, porque todas las secuencias de IVUS que he usado en esta tesis fueron extraídas de su arterias coronarias, a ellos quiero expresar mis más sinceras gracias,..., ***a los que padecen del corazón.***

Resumen

El uso de imágenes de UltraSonidoIntraVascular (IVUS) para la extracción de información cuantitativa sirve de gran ayuda en el diagnóstico y tratamiento de vasos arterioscleróticos. En la actualidad, esta clase de análisis es realizado por los médicos en forma semi-empírica, sin tomar en cuenta los principios que rigen la generación de la imagen, de la misma manera que tampoco se toma en cuenta la evolución temporal de la pared del vaso. Este hecho empobrece el uso de esta técnica, debido a que el análisis y la interpretación de las imágenes se basa sólo en los valores de los niveles de gris y en el comportamiento morfo-geométrico estático de la pared del vaso. Tomando en cuenta esta carencia técnica y conceptual, hemos dividido esta tesis doctoral en cuatro vías de investigación: La primera, está referida al trabajo experimental, que tiene como objetivo justificar nuestras hipótesis principales. En segundo lugar, hemos desarrollado e implementado un modelo básico de simulación con el propósito de obtener datos IVUS en forma sintética. En tercer lugar, hemos desarrollado una nueva metodología general que nos permite estimar desde el punto de vista del catéter el comportamiento cinemático de la pared del vaso y finalmente hemos propuesto un modelo genérico que permite obtener la reconstrucción geométrica del vaso en 2.5D.

El trabajo experimental fue hecho *in vitro* con corazones de cerdo y de ternera, enfocándose principalmente a estudiar la micro-arquitectura de la pared del vaso y su modificación geométrica debido a parámetros externos. Hemos analizado por separado y desde el punto de vista de imágenes IVUS, la evolución morpho-geométrica de la pared del vaso en los cortes longitudinales, debido a la presión pulsátil radial y a una rotación externa inducida al corazón de experimentación. El análisis dinámico realizado *in vitro* fue extrapolado a una muestra de 30 casos clínicos llevados a cabo por el Laboratorio de Hemodinámica del "Hospital Universitari Germans Tries i Pujol" de Badalona-España en cooperación con Boston Scientific-USA.

En lo que se refiere al modelo de simulación para obtener data IVUS 2D, está basado en los principios básicos de transmisión y recepción de ondas de sonido de alta frecuencia, al penetrar éstas radialmente una estructura arterial simulada. Hemos hecho una validación extensiva, comparando imágenes simuladas y reales, contrastando con la opinión de expertos quienes han delineado manualmente la configuración real de las capas del vaso. Para este propósito, definimos procedimientos que permiten extraer parámetros cuantitativos para medir similitudes globales y locales en las imágenes obtenidas. El modelo tiene diferentes utilidades. Primero, expertos médicos, así como investigadores en el área de visión, pueden generar imágenes simuladas con el objetivo de observar diferentes estructuras arteriales de interés clínico y compararlas con la distribución de niveles de gris en imágenes reales. Segundo, investigadores y médicos pueden usar nuestro modelo para aprender y comparar la influencia de los diferentes parámetros físicos en la formación de imágenes IVUS. En tercer lugar, este modelo puede servir para generar grandes bases de datos sintéticas bajo diferentes condiciones y parámetros de adquisición, para ser usadas en la validación de la robustez de técnicas de procesamiento de imágenes.

La tercera área de investigación que hemos abordado en esta tesis doctoral, ha sido el desarrollo de un modelo geométrico y cinemático, que tiene como propósito estudiar la evolución de la pared de las arterias coronarias desde el punto de vista del catéter. El modelo está basado en resultados experimentales los cuales demuestran que la evolución de la pared arterial en una secuencia de IVUS, puede ser modelada asumiendo dos contribuciones principales, que provienen de diferentes razones físicas: la primera contribución, es causada por propiedades geométricas intrínsecas de la arteria y la segunda contribución proviene de la dinámica oscilante del ventrículo. Estas contribuciones gobiernan en mayor grado la apariencia de los perfiles de la pared arterial en las vistas longitudinales. Usando estas afirmaciones, hemos generado las estrategias metodológicas con el propósito de estimar y suprimir las distorsiones dinámicas de las secuencias de IVUS.

La nueva formulación conceptual nos permite separar las contribuciones geométricas que dependen de la arquitectura intrínseca de la pared del vaso de las contribuciones dinámicas procedentes del movimiento del corazón. Finalmente, y dado que esta separacion es posible, hemos generado las bases fundamentales para la reconstrucción 2.5D del vaso desde el punto de vista del catéter, solamente haciendo uso de datos de IVUS. Esta metodología también podría usarse como una técnica alternativa que permite estimar la dinámica del corazón dado que el modelo contiene en forma explícita los parámetros necesarios para cuantificarla. En este sentido, se provee en esta tesis de una nueva posibilidad que permite potenciar la técnica IVUS como herramienta de exploración y de diagnóstico médico.

Abstract

Extraction of quantitative information from **I**ntra**V**ascular **U**ltra**S**ound (IVUS) images is very helpful for the diagnosis and treatment of atherosclerotic vessels. At the moment, this kind of analysis is carried out manually by physicians without taking into account the ultrasonic signal principles of the image grey level generation and the temporal evolution of vessel wall. This fact leads to a simplified use, analysis and interpretation of IVUS images based only on the grey level values of image pixels and vessel wall static morpho-geometric behavior. In this sense, this PhD thesis has been divided in four research ways: First one, experimental work, that has as objective to justify our principal hypothesis. Second one, we developed a basic simulation model, with the purpose to obtain IVUS data in a simulated way. Third one, we developed general methodology that allows to estimate from catheter point of view the vessel wall kinematics behavior. Finally we proposed a generic model to obtain 2.5D IVUS vessel reconstruction.

The experimental work was done *in vitro* using pig and calf healthy heart and was focused on the vessel wall micro-architecture analysis studying its temporal evolution when external parameters were varying. We have analyzed separately from IVUS images point of view (using longitudinal cuts), the vessel wall morpho- geometric evolution, due to radial pulsatile pressure and an induced external rotation done to the experimentation heart. The dynamical analysis that was done *in vitro* was extrapolated to a study sample of 30 clinical cases studied by ”Hospital Universitari Germans Tries i Pujol” of Badalona Spain in cooperation with Boston Scientific USA.

In the second research way, we developed an IVUS simulation model to obtain 2D IVUS data based on the basic transmission and reception properties of high frequency sound waves, when these radially penetrate a simulated arterial structure. We discuss an extensive validation, comparing simulated and real images, and contrasting the expert opinion respect to the manually delineation of real vessel layers, to test its usability. To this purpose, we define procedures to extract quantitative parameters that permit to measure the global and local similarity of the images obtained. The model has different utilities: Firstly, medical expert and computer vision researchers can generate simulated IVUS images in order to observe different arterial structures of clinical interest and their grey level distribution in real images. Secondly, researchers and doctors can use our model to learn and to compare the influence of different physical parameters in the IVUS image formation. Third, this model can generate large database of synthetic data under different device and acquisition parameters to

be used to validate the robustness of image processing techniques.
In the third research line, we develop a geometric and kinematic model in order to study the evolution of coronary artery wall from catheter point of view. The model is based on experimental results which demonstrate that the evolution of the arterial wall, can be modelled assuming two principal contributions that come from different physical reasons. The first one, a systematic contribution caused by geometric intrinsic arterial properties and the second one, an oscillating contribution that comes from ventricle dynamics. These contributions govern in major degree the profiles appearance of arterial wall in longitudinal views. Using these assumption we generate the methodological strategies in order to estimate and suppress IVUS dynamical distortions. The new conceptual formulation allows to separate geometric contribution that depends on intrinsical vessel wall micro-architecture from dynamical contribution that comes from heart movement. Finally, being possible this separation, we generated the fundamental basis to $2.5D$ vessel reconstruction from catheter point of view, only using IVUS data. This methodology can be used as alternative technique to evaluate the dynamic of the heart, due to the fact that model dependence has explicitly the parameters to be estimated. In this way, we provide in this PhD thesis a new possibility that allows to give new potential to the IVUS technique as an exploratory and medical diagnostic tools.

Contents

List of Tables

List of Figures

Chapter 1

Introduction

The arteriosclerotic cardiovascular diseases [1] increase their incidence in vertiginous form, reaching after half-full of the decade of the fifties the first place like cause of mortality in the industrialized countries, place that at the moment occupies over the cancer and the accidents. In effect, the arteriosclerotic diseases, in general (infarct to miocardio, angina of chest, accidents cerebrovascular, and arterial diseases of the legs and arms) have caused, and continue causing, more deaths and consultations in the rooms of emergency and doctor's offices that any other disease in this century, including the AIDS. The coronary arterial diseases are developed due to a narrowing (stenosis) of the walls of the coronary arteries, caused by the accumulation of fibrotic material and calcium crystals [8]. The development of this type of plaque normally takes in humans between 15 and 20 years to form. There exist complicated injuries, which generate the formation of thrombus, the rupture of the plaque can be considered an important mechanism of the acute coronary syndromes. An imminent problem that happens if the arteries narrow too much due to the stenosis is that the blood flow diminishes in significant form. A total occlusion can take place by the maintained increase of a stenosis but also it can become serious due to a thrombosis. The result can be an infarct. The introduction in the field of the medical image of the **I**ntra**V**ascular **U**ltra**S**ound (IVUS) [9, 33] as an exploratory technique has made a significant change to the understanding of the arterial diseases and individual patterns of diseases in the coronary arteries. Although the coronary angiography [10, 34] provides with 2D information about the coronary anatomy, serving as guide in the operations, it is limited when not allowed to access to the mechanism of the disease, composition and extension of the same. On the contrary IVUS technique visualizes the cross-section (Fig. 1.1) of the artery allowing an evaluation of the plaque as well as of the different layers from the arterial wall. The IVUS image [8, 10, 34] provides qualitative (Fig. 1.2) information about: The causes and severity of the narrowing of the arterial lumen, distinction of thrombus of the arteriosclerotic plaque, recognition of calcium deposits in the arterial wall, unexpected evaluation of the awaited changes and complications in the coronary arteries after an intervention as angioplasty, evaluation and diagnose of coronary arterial aneurysms, diagnose of fissures

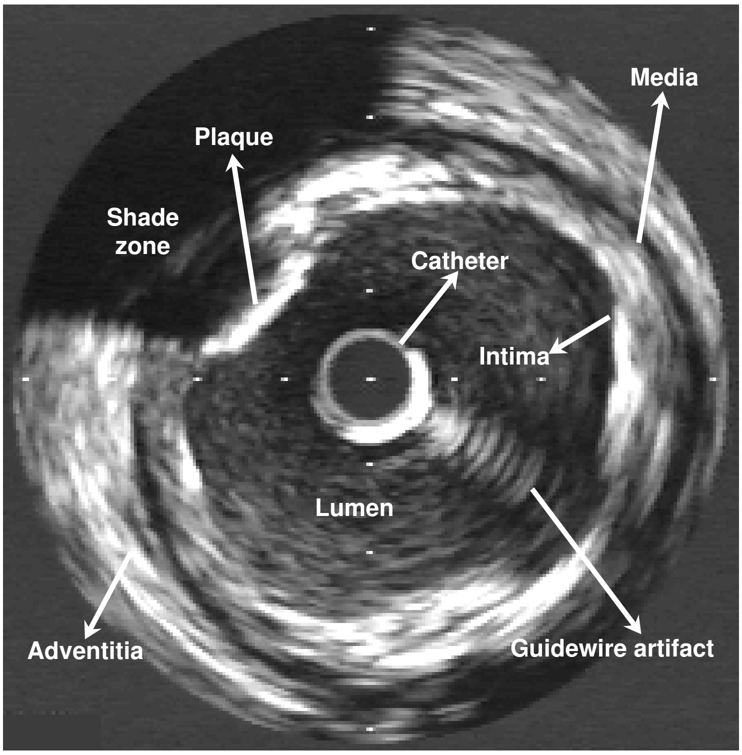

Figure 1.1: Typical 2D IVUS image indicating the location of the principal morphological arterial structures and artifacts.

of arterial coronary plaques: determination and location, dimensions, type (eccentric and concentric) and composition of the arteriosclerotic plaque.

1.1 Present Limitations of IVUS Technique.

The main roll of IVUS technique is to serve as a guide in the interventional procedures allowing to measure the cross-section of the artery. The precision in the measurements of distance is subject to the following potential sources of error [28]:
a) Incorrect identification of the surface and the sections to be measured. Although the vessel and the interface defining the wall vessel have sufficiently good acoustic in most of the cases, still in several cases the identification of the surface and differentiating tissues can result difficult. When improving the radial resolution, it could improve the detection of contours, this would reduce the error. These errors can in some cases be systematic and lead to an overestimation of the dimensions. This could get considerably worse if the irregularities of the vessels are very pronounced.
b) Assumption that the sound speed is constant in the arterial structure. The second kind of problem related to assuming the constant speed of the sound at 1540 m/seg,

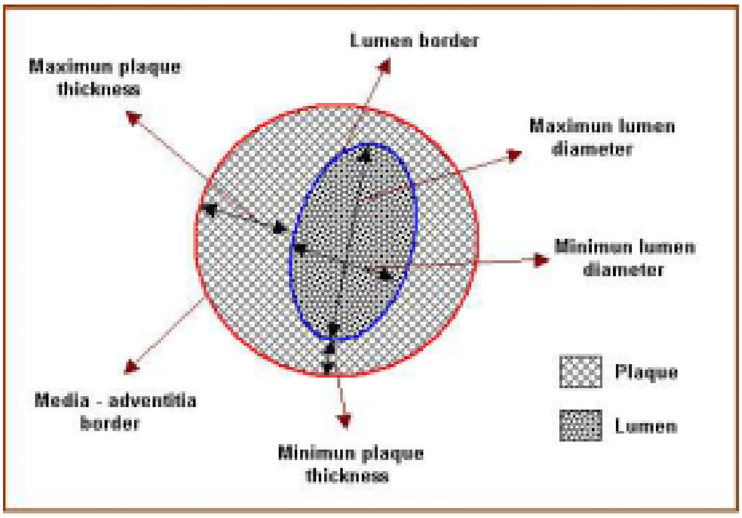

Figure 1.2: Geometric parameters of an artery that make possible to measure by means of Intravascular Ultrasound.

is systematic and small of the order of 1 to 2%, which brings as a consequence the propagation of the error to the location of each one of the structures in study.
c) Artifacts caused by inhomogeneities in the rotation of the catheter and pronounced reverberations generated by very acute irregularities of the vessel. The appearance of some artifacts such as the inhomogeneities in the rotation of the catheter, has influences on the quality of the image. The absence of beams, when the catheter stops momentarily, brings as a consequence a propagation of errors in the tangential direction of the image.
d) The IVUS images characterization is performed by the medical doctors using only perceptual information that not take into account physical aspect related to the ultrasound beam tissue interaction.
e) Impossibility to obtain row data using IVUS information, due to the transducer pressure has been transformed into intensity values. The row data play a very important role to evaluate textural information used in plaque characterization and is the principal data to evaluate tissue elastic properties [46].
f) Impossibility to locate spatially the catheter. The impossibility the locate the catheter with respect to a specific axis of coordinates makes impossible any attempt of three-dimensional representation of the vessel only with IVUS technique. For example: spatial location of the effective section of the lumen and location of plaque and the reconstruction in the lengthwise direction of the vessel are still an open problem of investigation [28].
g) Impossibility to evaluate dynamic parameters, different from the single static characterization using the grey levels. First achievements are related to IVUS elastography [46] which purpose is to propose a technique for tissue characterization. h) Dynamical image distortion such as IVUS rotation images, caused by heart movement, increment the difficult to evaluate quantitative measures in longitudinal views.

1.2 Thesis Goal.

The general goal of this thesis is as follows:

1 To study the vessel wall dynamic behavior using the IntraVascular UltraSound technique. The specific work can be divided in three groups:

  - To develop and perform a physical model in order to obtain IVUS data in a simulated way.
  - To generate and develop a geometric and kinematic model in order to study from catheter point of view, the temporal and spatial evolution of coronary artery wall.
  - To generate the methodological strategies in order to estimate and suppress IVUS dynamical distortions.
  - To generate the methodology to study the 2.5D IVUS vessel reconstruction.

1.3 Thesis Motivation and Contributions.

At the moment, the IVUS images analysis is carried out manually by physicians without taking into account the ultrasonic signal principles of the image grey level generation and the temporal evolution of vessel wall. This fact leads to a simplified use, analysis and interpretation of IVUS images based only on the grey level values of image pixels and vessel wall static morpho-geometric behavior. Some of the limitations of IVUS technique (See section 1.1) can be attenuated through algorithms of static and dynamics image processing; the limitations due to a suboptimal location of the borders of the arterial structure can be improved with new algorithms of segmentation and dynamical interpretation of the sequences. The question is how to develop robust algorithms that can solve these problems analyzing the artifacts with their multiple appearance in IVUS images. Having a complete set of patient data to present all variances of artifact appearance in images would mean to dispose of a huge amount of patient cases. For these reasons, we developed in this PhD thesis the following contributions:

Our Contribution: *IVUS Simulation Model.*

A first efficient solution to improve the IVUS image interpretation is to develop a simulation model for IVUS data construction so that synthetic data is available in order to "train" image processing techniques. In this way, different appearance of artifacts can be designed to assure a robust performance of image processing techniques. Differences in IVUS data are caused not only by different morphological structures of vessels but also by different parameters that influence the formation of IVUS images. The images depend on the IVUS apparatus calibration as well as interventional devices, small differences in parameters can lead to different grey-level appearance that can be interpreted in a different way by physicians. Having a simulation model

for IVUS data can be useful to train medical staff as well as can play an important role in designing and testing new interventional devices. Finally, we think that the combination of some parameters and their influence in image formation can be of unquestionable importance for all personnel involved in the understanding of IVUS data and taking the final decision for diagnosis and intervention of vessel lesions.
In order to fulfill these objectives we have as first step to understand the Intravascular Ultrasound as a technique. Therefore, a physical model will be proposed in order to obtain in a simulated form the corresponding IVUS data. An exhaustive investigation should be done about following issues: Biological tissue ultrasound interaction, technical aspects related to the physical and mechanical properties of the transducer ultrasound, transducer emission pattern radiation, ultrasound emission/reception protocol, radial and tangential resolution dependence, mechanical dependence, emission and reception distortions that influence the final IVUS image. We have contributed in the generation of synthetic IVUS images developing particular strategy in the following topics:

1. The generation of ultrasound pulse.
2. The creation of a basic model that emulates the interaction between ultrasound and scatterers.
3. The construction of an adequate spatial geometry that simulates the vessel structure.
4. The production of 2D IVUS images.

1. **The Generation of Ultrasound Pulse.** A variety of different methods [12, 15, 16, 17, 18] has been employed to generate the ultrasound pulse. We use the more simple impulse function $\Gamma(t, \delta)$ approximated by a Gaussian, which envelopes the transducer intensity distribution [17] at central frequency 30, 40 to 50 Mhz and a band width Δf at $10MHz$, as typical IVUS values used by Boston Scientific equipment. As interaction model between biological tissue and ultrasound beam we have used a reflection model [12, 13, 14, 15, 16] that only takes into account the wave reflection. In the frequency ranges used by IVUS techniques, Raleigh diffraction effects and lateral wave dispersion can be negligible [16], without having a negative influence on the final IVUS images appearance. Taking into consideration this assumption, the ultrasound emitter/receiver can be considered punctual-localized and it only radiates in forward direction. Therefore, the lateral signal emition/reception is negligible.

2. **The creation of a basic model that emulates the interaction between ultrasound and scatterers.**
   Tissue and Ultrasound Interaction. In order to consider textural information that comes from biological tissue, the exponential intensity decay model [45] of ultrasound absorption has been assumed. This model considers explicitly the ultrasound frequency, the radial decaying dependence of ultrasound beam

intensity and the scatterers number dependent on the ratio of grain, particle size or the scatterer number located along the ultrasound beam path. In this way, the simulated IVUS data has local information about scatterer size and its density. This information is very important in image descriptor selection that can be used in future work by inverse problem to tissue characterization validation.

3. **The construction of an adequate spatial geometry that simulates the vessel structure.**
   Scatterers Distribution and Vessel Wall Structure. The spatial generation and physical characterization of scatterers corresponding to blood and vessel wall tissue play a very important role in the IVUS images generation model.

   - **Blood Scatterers Representation**. In our model we define a clear interphase spatial separation between blood and vessel wall tissue scatterers using their density as the main physical characterization parameter. Fontaine and coworkers [13] have carried out an exhaustive investigation in red blood cells to demonstrate the positive dependence between the signal reflection amplitude of ultrasound and geometrical spatial aggregation of blood cells. According to this study using static blood conditions, a red blood cell aggregate model should be necessary in order to introduce textural properties in our model simulation. However the IVUS data signal is generated by blood in movement, which means that the red blood cell aggregates have not been taken into account giving as result an aleatory behavior on spatial location and temporal evolution of the blood scatterers. Therefore, in our model we assume that the blood scatterers can be represented as "voxel" of different sizes with a random spatial distribution. Each "voxel" is considered as an individual independent entity, that contains N elemental scatterers. The maximal "voxels" number to be simulated is calculated using the maximal IVUS axial and tangential resolution, avoiding unnecessary calculation which will not appear in the final image. We use the heuristic: "*To simulate only what is susceptible to be seen, using the maximal resolution we can provide.*" This strategy allows us to represent a great number of particles per "voxel", making a treatable problem from a computational point of view. Also, using a standard PC we can simulate one image per second that represents $\approx 10 \times 10^8$ $cells/mm^3$, the same simulation condition can be used approximately 10 minutes by standard simulation programs [45].
     The scatterers blood simulation in our model have a great importance. However, the major emphasis should be done by the vessel wall generation.
   - **Vessel Wall Representation**. The vessel wall in our model is treated as an abrupt change on the scatterer's size and density, which is due to a physical interphase apparition, that makes that the ultrasound intensity increases in a localized spatial region. From a morphological point of view, the vessel wall can be interpreted only as a boundary between blood and

tissue, that coincides perfectly with the image segmentation point of view. However, from a physiological point of view the vessel wall belongs to the cardiovascular irrigation system, and therefore governed by the ventricle dynamics (See Appendix C). In this thesis, we admit as valid these two research ways. Furthermore, the vessel wall simulation can be considered as a static and isolated entity, that the vessel wall, blood pressure and heart dynamics are supposedly independent.

A first objective of this study is to generate static IVUS images, and a second objective is to study IVUS sequences from a dynamical point of view, taking into account the morpho-geometric temporal and spatial evolution of the vessel wall.

4. **The production of 2D IVUS images.** The static simulation of vessel wall in our model has been oriented to describe two fundamental aspects in image segmentation: The first one is to know the main ultrasound physical parameters that emphasize the lumen-vessel interphase. In this way, we study the beam ultrasound frequency as responsible of radial resolution and the beam intensity that produces a good structure visibility. Second one is to know the influence of filtering and image protocol on 2D image appearance.

Our Contribution: *Vessel Wall as Geometric and Kinematics System.*

In this PhD thesis, we introduce a new conceptual formulation that permits us to separate geometric contribution that depends on intrinsical vessel wall micro-architecture from dynamical contributions that come from heart movement. In Fig. 1.3 we can see the main factors that influence the vessel wall shape evolution. Geometric factor such as: Vessel architecture, catheter trajectory and local vessel pathologies can be observed in static IVUS image condition, but, in order to observe vessel ventricle-interaction, catheter point of view influence and blood pulse dependence, a temporal analysis is necessary. This formulation is based on experimental results, that demonstrate that by an IVUS sequence, there are two contributions to the vessel wall shape evolution. Firstly, when the catheter remains stopped (See Fig. 1.4 (a)) we can observe a periodic behavior that comes from ventricle dynamics. In this case, the vessel wall morpho-geometric quantities repeat their values each heart cycle, only the pulsatile heart movement can be observed. When the catheter initializes the pullback (See Fig. 1.4 (b)), the morpho-geometric measures change systematically according to the vessel wall geometrical characteristics, namely, their torsion and curvature. Therefore, the second contribution is due to a systematic contributions that depend on the vessel geometry. If it is possible to separate the geometric contribution from dynamics contribution, this analysis could be the fundamental basis to 3D vessel reconstruction only using IVUS data and could be an important advance in vessel wall dynamics estimation such as to introduce an alternative technique to estimate local heart dynamics [47]. In this analysis, we assume that the morpho-geometric vessel properties are responsible for the systematic contribution, namely: the anatomic and

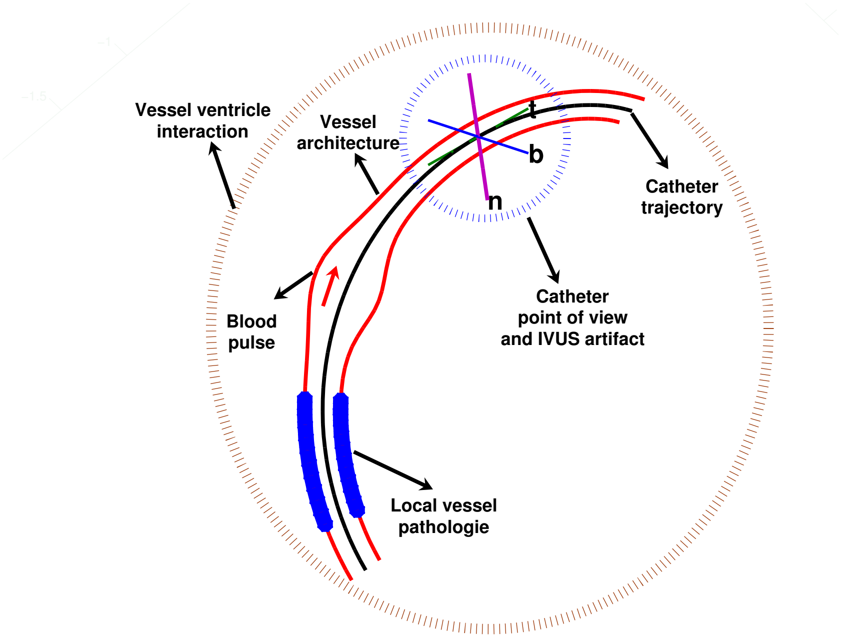

Figure 1.3: The main factors that influence the vessel wall shape evolution.

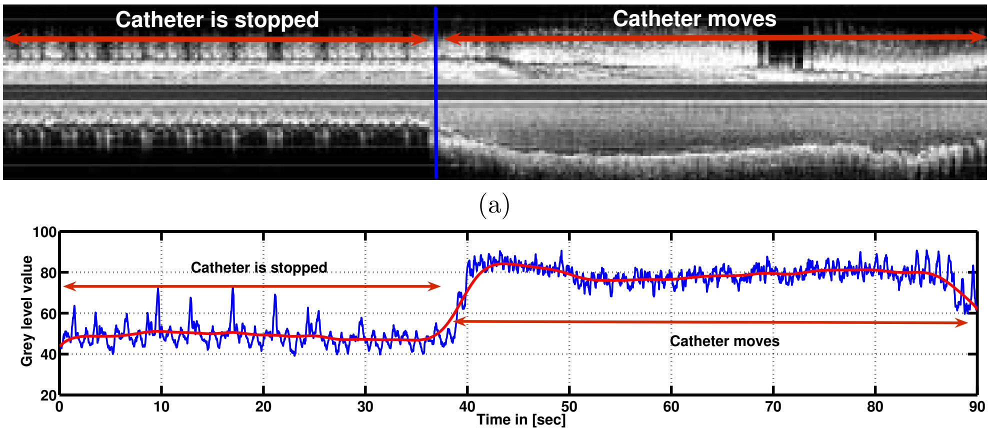

(a)

(b)

Figure 1.4: IVUS longitudinal cut of a coronary artery (a). Mean grey level corresponding to the inferior lumen border (b).

geometric configuration of the vessel layer, its micro and macro architecture, layers density and mechanical properties in transverse direction. The influence of the intrinsical vessel properties such as torsion and curvature, on the systematic behavior of the vessel wall shape evolution of an IVUS sequence, plays an important role in this work. This properties should be taken into account in order to model the vessel wall, which structure is a very complex system [53] due to anisotropic material properties and the ventricle dynamics contribution (See Appendix C) [38].

Our Contribution: *IVUS Kinematics Suppression.*

The IVUS allows to visualize and to obtain measurements on the cross sections of arteries. Nevertheless any volumetric 3D study of vessel segments requires the analysis of longitudinal views. Each IVUS plane visualizes the cross-section of the artery allowing, among others the assessment of different vessel plaques (thrombus of the arteriosclerotic plaques and calcium deposits) and the determination of morpho-geometric parameters [8, 10, 34]. 3-D IVUS is obtained by assembling in a stack 2-D IVUS images acquired during an automatic pullback of the catheter. 3-D IVUS is of great clinical interest as it allows to evaluate and quantify atherosclerotic plaque on arterial distensibility [62], to follow-up the plaque and lumen after intervention [61], and to guide the selection of an optimal interventional procedure [68]. However, artifacts introduced by the image periodic motion due to cardiac dynamics troubles accurate assessment of morphological structures along the data sequence and, thus, limits the 3-D IVUS imaging applicability to interventional procedures. Vessel displacement and rotation in IVUS images are the main image sequence artifacts introduced by cardiac dynamics [63, 64, 65, 66] and 3-D shape of the vessel [2]. Their effect in 3-D IVUS images has been described [2, 54, 35, 28, 69, 49, 63, 67] as a "saw-tooth-shaped" longitudinal appearance of the vessel wall that decreases precision in volumetric measurements. Usually, the sinusoidal wavy pattern of the vessel wall (see Fig.1.5(a)) due to the heart dynamics and blood pulsation troubles the vessel wall detection and analysis of vessel structures along the sequence. If we project the grey-level pixels in the temporal direction (longitudinal vessel direction) of the IVUS sequences, we can observe that salient features usually representing the calcium and fibrous plaque and adventitia-media borders describe a trajectory of semi-rotation of a ring around a stick (in this case, the catheter) (Fig.1.5(b)). The most disturbing phenomenon induced by vessel periodic motion is that the displacement invalidates any point correspondence along the sequence as, given a fixed angle in the short-axis IVUS image, points from different temporal frames do not correspond to the same vessel wall segment. A usual strategy used to minimize the impact of the above described artifacts is to synchronize sequence acquisition with heart dynamics. This can be achieved by either ECG-gated devices [49] or by an image-based ECG-gated 3-D IVUS [50]. In the first case, a special ultrasonic device performing the catheter pullback at the same systolic peak is required and the acquisition time significantly increases. In the second case, one discards all frames between two consecutive systolic peaks, thus, running the risk of loosing valuable information. Keeping all frames and aligning them suppressing their rotation and displacement would allow to get reliable radial measurements during the whole cycle related to the estimation of the elastic properties of the vessel. Alternatively, reconstructing the path using biplane angiography [70, 2] could alleviate the geometric distortions due to the position and angular rotation of the catheter by tracking the Frenet triangle according to the vessel tortuosity, although in this case, image rotation due to heart dynamics is not considered. The goal of this work is to

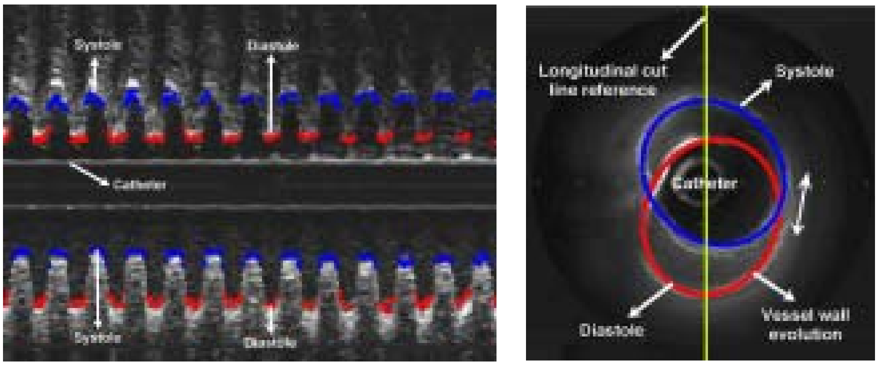

(a) (b)

Figure 1.5: Sinusoidal shape in a longitudinal cut (a) and grey level shift in cross sectional view (b)

estimate and remove the displacement-rotation effect using only IVUS imaging and without loosing any image data in order to improve the longitudinal vessel visualization and measurements in standard IVUS acquisitions (without the need of any additional devices for ECG-gating). Our hypothesis is that the vessel wall motion in IVUS images is due to two main factors: a systematic contribution caused by vessel wall geometry and a dynamical periodic contribution due to the heart pulsatile contraction influence. This decomposition of the vessel profiles serves to model the vessel dynamics and determines a robust procedure for vessel motion suppression. Aiming to correct rigid transformation the vessel wall is approximated by an elliptical model that is tracked in IVUS frames to estimate its rotation and translation. The elliptical approximation [52] is computed on a rough segmentation of salient vessel structures using a Neural Network algorithm [30]. An advantage of strength of our strategy is that it does not need of a precise segmentation of vessel structures in order to correct vessel motion. The set of reported experiments includes vessel motion simulations and validation of vessel dynamics suppression in real data of 30 patients. Our results reveal suppression of rigid transformation up to 98% in synthetic data and up 86% in real data.

Our Contribution: *Towards Vessel Reconstruction.*

The vessel wall reconstruction has been a very important problem in modern cardiology. The more used 3D reconstruction technics such as angiography that use stereographic images to estimate externals views of spatial vessel wall location [2, 3, 4, 5, 6, 7], has been used with IVUS modality, allowing external and internal vessel wall point of view when this two complementary modalities are simultaneously used. The vessel wall morpho-geometric quantification, such as volumetric plaque quantification, in diagnostic and post-treatment evaluation, justified amply the actual effort in 3D reconstruction. The 3D vessel wall reconstruction only using IVUS images, represents a great methodological challenge, that should allow to extract from IVUS data, the morpho-geometric vessel wall parameters and give the possibility to obtain vessel torsion and curvature. However, our first purpose is to obtain an approximated geometric vessel wall $2.5D$ description when the heart dynamical influence is suppressed. We introduce a very simple elliptical model to describe the vessel wall behavior assuming the z coordinate in longitudinal direction. Also in this first step vessel curvature and torsion will not be taking into account. This description can be considered acceptable by straight vessel, where the vessel curvature and torsion can be negligible.

This PhD thesis has been divided in 6 chapters.

- **Chapter 1**. contains this introduction.
- **Chapter 2** gives a thesis background.
- **Chapter 3.** discuss a basic model to obtain 2D IVUS images simulation.
- **Chapter 4** gives a general exposition over the vessel wall dynamic evolution from catheter point of view and the general geometric and dynamic model is analyzed.
- **Chapter 5** gives the basic methodological strategies that allows us an approximation to 2.5D vessel reconstruction.
- **Chapter 6** present the conclusions and future lines.

Chapter 2

Thesis Background

In order to understand the internal and external factor that influences an IVUS sequence temporal evolution, we assume that the vessel wall interaction can be considered as a dynamic and geometric system that has a deterministic physical [39] behavior (Fig. 1.3). The static factors that depend on anatomic, geometric and intrinsical mechanical vessel properties can be used to describe 2D static IVUS images. The dynamical factors due to influence of blood pressure, vessel wall-ventricle interaction and catheter point of view can be used to describe the temporal evolution of vessel wall shape in an IVUS sequence. The IVUS sequences can be studied as a result of the assembly and the interaction of these entities.

One of the disadvantages of vessel wall characterization based on the dynamic parameters extracted from IVUS sequences is that it is not possible to measure locally the blood pressure due to technical reasons because it is not possible to use simultaneously the IVUS catheter and the pressure transducer at the same time and at the same spatial position. A lot of effort in research to obtain the radial deformation of vessel wall is limited only to *in vitro* studies. The main disadvantage in technical applications in *in vivo* studies of elastography and palpography is the local blood pressure quantification [46]. The IVUS technique permits us to explore *in vivo* the vessel wall kinematics, but the radial deformation on the image not only depends on the blood pressure variation, but also depends on the artifact produced by oscillating obliquity induced by the ventricle pulsatile dynamics. Any effort to obtain in situ vessel wall elastic properties using IVUS sequences should emphasize on the suppression of dynamical deformation that are blood pressure independent.

In order to justify the principal assumption used in this thesis, in next section we explore several experiments, carried out with an *in vitro* healthy heart of a pig and an healthy heart of a calf. Crick S. [72] and coworkers have performed a qualitative analysis of porcine and human cardiac anatomy. From this gross examination and dissection of hearts using macrophotography, they found several potentially significant similarities exist between porcine and human hearts. For example, elastic behavior of coronaries arteries between porcine and human heart are quantitatively comparable.

2.1 *in vitro* Experiments.

Current research from a discrete element theory point of view [29], has developed a constitutive model, that takes into consideration, mechanical and geometrical properties of vessel wall. However, this research has demonstrated that the media has a tensile strength, in the transverse direction, equal to the combined strength of all layers (intima and adventitia) [37, 29]. This result can be used to propose a simple model of vessel wall, assuming that it can be modelled as an elastic tube [36]. The dynamic behavior of the vessel wall is due to the dynamic ventricle, the pulsatile blood flow and the geometric properties that come from media layer, which is the more important layer responsible on the vessel wall shape evolution when the radial blood pressure change.

We assumed that the vessel wall can be geometrically modelled as a circular fiber oriented in longitudinal vessel direction, which mechanical and geometric properties in radial direction depend on media layer properties and the dynamics properties depend on the heart dynamics behavior.

In order to justify this bimodal analysis, we will discuss in the next section, different experimental setup that can help to understand the genesis of vessel wall shape dynamics. These experiments have been focused on the purpose of generating a simple model that allows to generate synthetic IVUS data. The experiments have been organized as follows:

1. Vessel wall morpho-geometric properties.
2. Vessel wall dynamic shape temporal evolution.

1.1.- **Vessel wall morpho-geometric properties.** This study has been carried out in cooperation with the Department of Pathological Anatomy, Veterinary Faculty, UAB . This experiment was performed using a 4-month-old healthy pig heart. The coronary arteries were removed and 1.5-2 cm long cylindrical segments were identified and dissected. The segments were rapidly and carefully mounted using cylindrical wood adaptors and immediately were submerged in liquid paraffine that was posteriorly solidified. Longitudinal cuts of $5\mu m$ were done, the Malory and Hasson [48] tinction were used in order to observe the elastic and muscular fiber present in the vessel wall. Figure 2.1 shows a healthy longitudinal cut image and its corresponding magnified 2X (See Fig. 2.2) (a)) and $10X$ (Fig. 2.2) (b)) . We can observe the three layer configuration intima, media and adventitia. This images shown the vessel wall three layers configuration that are responsible of the vessel elastic recuperation. The real objective of this first exploration was to observe the vessel macroscopic architecture in longitudinal direction and to explore its typical dimensions. Using this longitudinal cut was impossible to detect any helicoidal fiber configuration, therefore we performed a more exhaustive study using high resolution optical micro-photographies.

1.2.- **Vessel wall micro-architecture.** This investigation was realized in the Microscopy Laboratory by Science Faculty, UAB. This experiment was performed

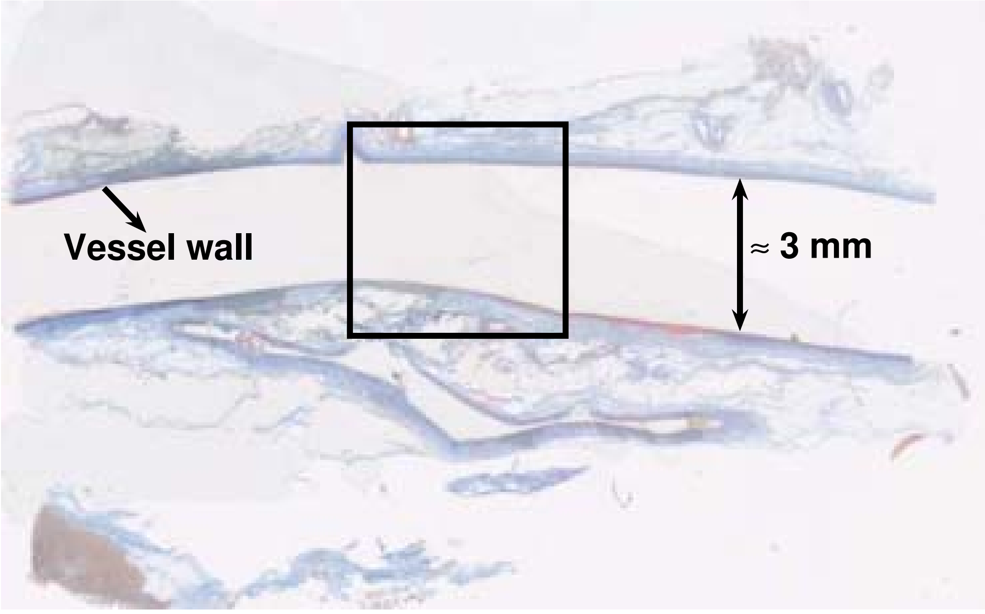

Figure 2.1: Longitudinal cut of a pig coronary artery.

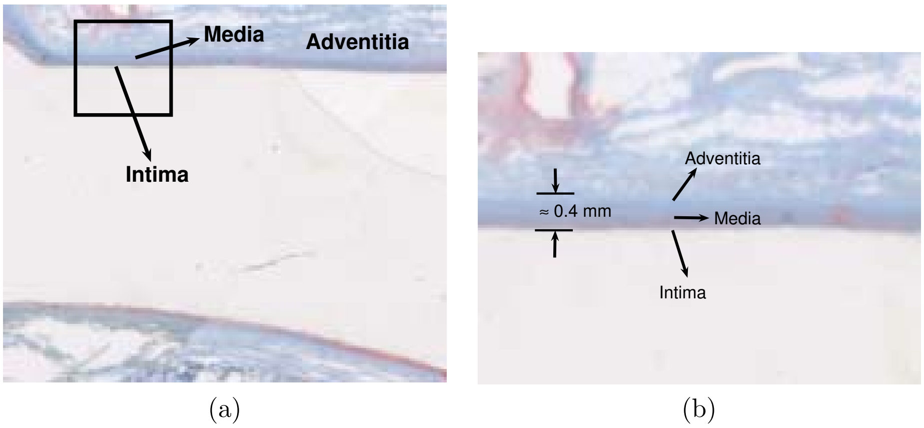

(a) (b)

Figure 2.2: Longitudinal cut of a pig coronary artery augmented 5X (a) and 10X (b) from Fig. 2.1.

using a healthy heart of calf (See Figure 2.3 (a)). The coronary tree (See Figure 2.3 (b)) was carefully removed from the heart. Cylindrical segments 1.5-2 cm long were identified and removed. All segments were mounted using cylindrical wood adapters (See Fig. 2.4 (a)). The segments were coking during 3 hours and placed in a physiological salt solution. In order to observe the media layer, the

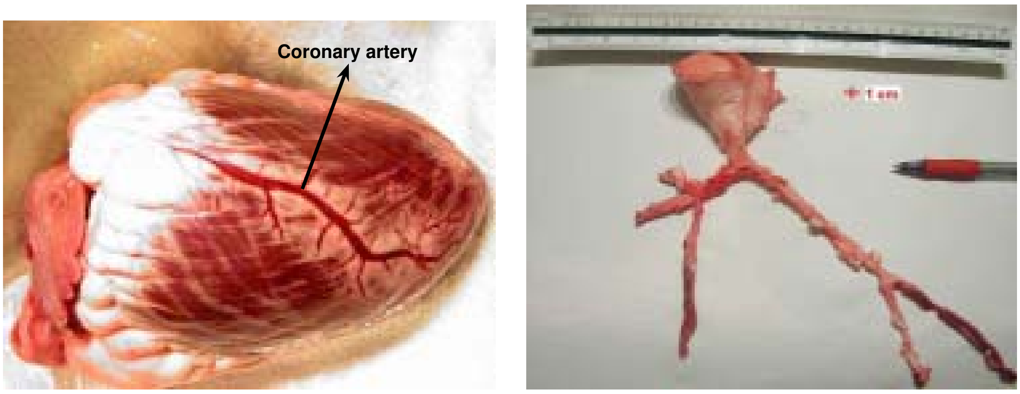

(a) (b)

Figure 2.3: Healthy heart of a calf used in the experiment (a). Tree coronary (b)

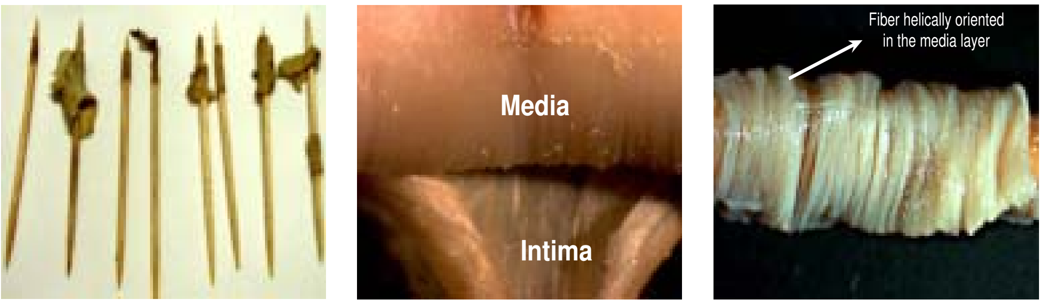

(a) (b) (c)

Figure 2.4: Cylindrical artery segments mounted in a wood adapters (a). Intima and media layers dissection (b). Helically fiber arrangement in media layer (c).

artery segments were inverted and mounted using cylindrical wood adapters, in this manner the intima was carefully removed (See Fig. 2.4 (b)) also the media fiber configuration can be perfectly observable (See Fig. 2.4 (c)).
In figures 2.5 we can observe a helically fiber configuration oriented in vessel wall axial direction that finally covers totally the artery. The vessel wall micro-architecture and the elastic properties that depend on this configuration has been used in the constitutive model described by [29]. However, how the fiber configurations affect the IVUS image appearance, there is no report today. This investigation way can play a very important role to study the vessel wall elastic properties, due to the media layer is the major responsible in the mechanical recuperation of an artery.

1.3.- **Media fiber configuration and dynamical effects.** The dynamical effects of media layer fiber orientation on the vessel wall shape dynamics temporal evolution in IVUS images, has not been reported today. We did a simple experiment to demonstrate, that applying a pulsatile pressure $\overrightarrow{P}(t)$ in an helicoidal

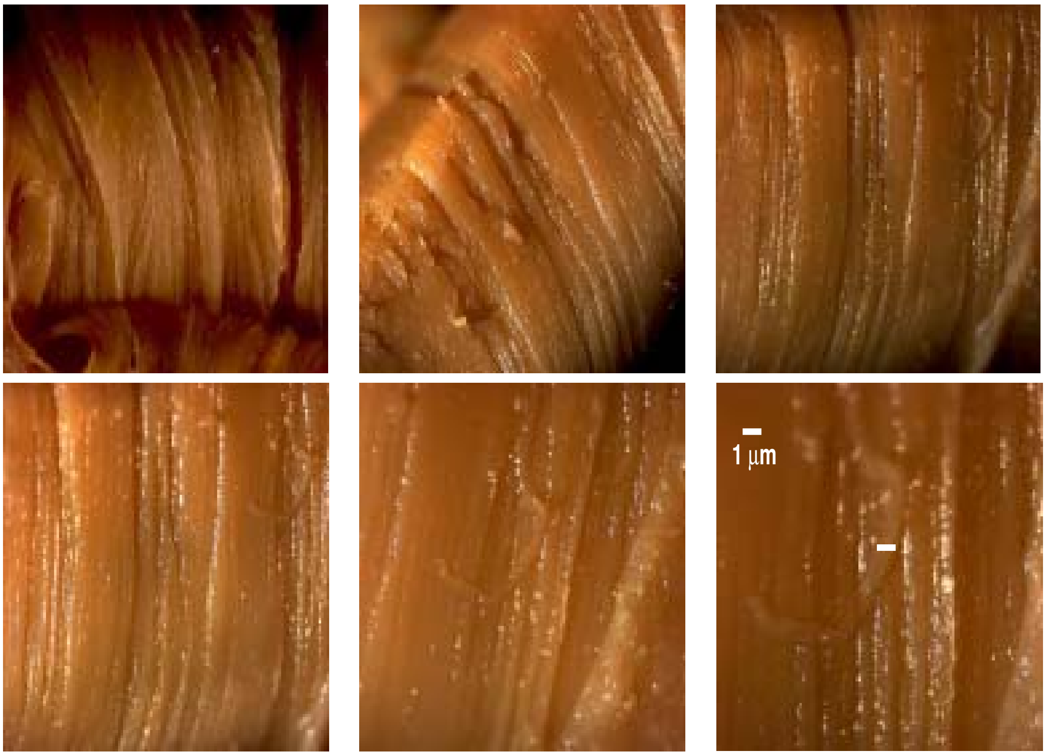

Figure 2.5: High resolution images from media arrangement fiber of a calf coronary artery. We can observe that the fiber diameter is $\approx 1\mu m$.

configuration of elastic fiber that covers longitudinally an elastic tube, it generates a local rotation movement on the tube wall, having as rotational center the tube longitudinal axis. The experimental setup at t=0, is shown in figure 2.6. At time $t = 0$ at static conditions, the constant pressure profile Po is applied (Fig. 2.6 (a1)) to an helicoidal elastic fiber configuration that represents the media layer, which covers a tubular membrane that represent the intima layer (Fig. 2.6 (a2)). We can observe a reference point $P1$ at $\alpha = \alpha_0$ angular position. At time $t > 0$ (Fig. 2.7 (a1)) the pulsatile pressure pulse $\overrightarrow{P}(t)$ at velocity $\overrightarrow{V}$ along tube axis, begins to inflate the tubular membrane. Due to the helicoidal fiber configuration, the instantaneous and local deformation $\overrightarrow{r}(t)$, generates a tangential strength whose torque is given by, $\overrightarrow{\tau} = \overrightarrow{r}(t) \times \overrightarrow{P}(t)$, originating a local rotational movement given by, $\overrightarrow{\ddot{\alpha}} = \overrightarrow{\tau}/I$, that has as rotational axis the longitudinal tube axis, where I is a constant that depends on tube/fiber inertial properties and $\overrightarrow{\ddot{\alpha}}$ the angular acceleration of reference point $P1$ [36]. When the pressure pulse $P(t)$ disappears the $P1$ angular position comes back to the initial position α_0. The temporal $P1$ angular position is governed by the Hook's law, given by $\alpha(t) = K_\theta F_\theta(t)$. Where K_θ is the tangential elastic constant that depends on the tube/fiber configuration properties and F_θ is the local tangential

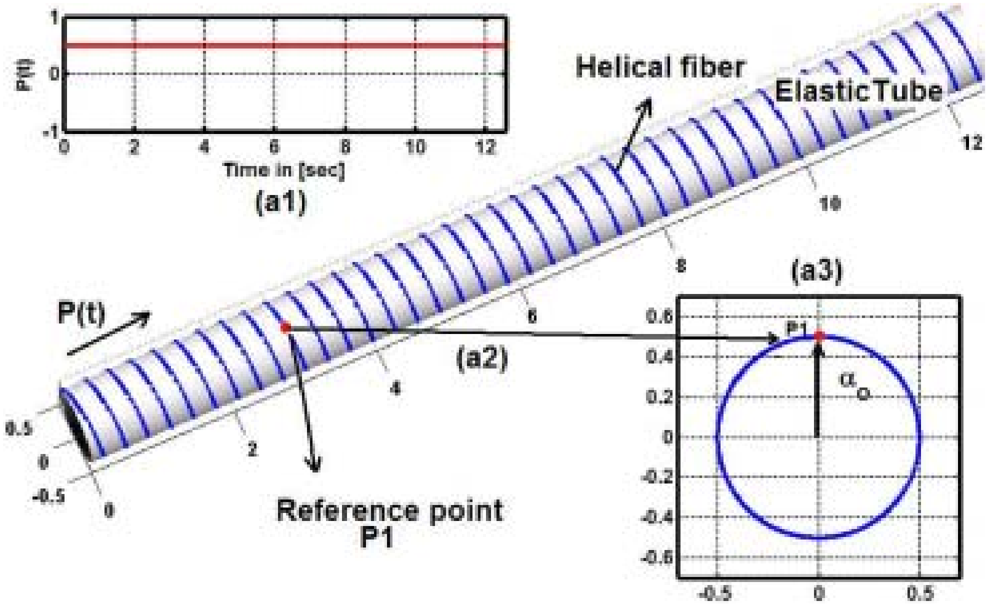

Figure 2.6: Vessel wall rotational dynamics at time $t = 0$. Pressure pulse evolution P(t) in (a1). An elastic tube cover by helically elastic fiber (a2), the reference point (P1) is shown. The position of reference point (P1) at $\alpha = \alpha_0$, is observed in a cross sectional point of view (a3).

strength component. Using typical values of F_θ and K_θ [36], we can determine the angular deformation $\Delta\alpha$ by a free artery, being this $\Delta\alpha \approx 6^{\underline{o}}$. Note that the artery is fixed to the ventricle surface, therefore the angular deformation should be smaller as $\Delta\alpha << 6^{\underline{o}}$. Also, this mechanism is responsible of small vessel wall tangential deformation, but its valuation is very important since gives an important information on the vessel wall intrinsical properties.

1. **Heart dynamics versus fiber configuration.** With the purpose of separating and quantifying the contributions due to fiber configuration from dynamical contributions originated by the heart dynamic, we performed an experiment using an *in vitro* heart (See experimental setup Fig. 2.8). A healthy calf heart of 5 months submerged in salt solution at $\approx 37^{\underline{o}}$, was used to this propose. A right coronary artery was water inflated at constant diastolic pressure Pd at 80 $mmHg$ and a pulsatile systolic pressure between $(80 \leq Ps(t) \leq 1500)$ $mmHg$ at 1Hz of frequency. Due to the vessel wall radial deformation by pressure in the range between 80 to 140 $mmHg$ (normal human blood pressure values) is very small, we incremented the systolic pressure range in order to observe in better condition the pressure influence on the vessel wall radial deformation. An IVUS pullback was made simultaneously in order to obtain the vessel wall dynamic due to the pressure inflation. The diastolic pressure was measured by the barometer $B1$ and the sinusoidal systolic pressure $Pd(t)$ was measured by the barometer $B2$. The oscillating systolic pressure emulates the blood pressure

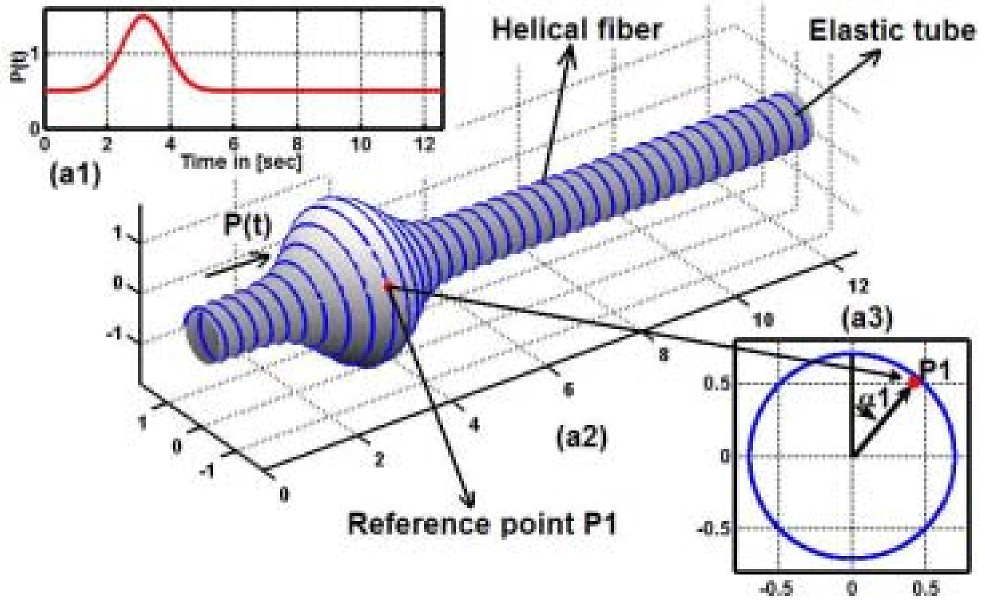

Figure 2.7: Vessel wall rotational dynamics at time $t > 0$. The pressure pulse evolution (a1) inflate progressively the elastic tube (a2), that is cover by helically elastic fiber. Due to tangential strength, the reference point (P1) change at angular position $\alpha = \alpha_1$ (a3).

pulse. Figure 2.8 (b) shows an obtained cross sectional image using this experimental setup. A longitudinal vessel cut can be observed in figure 2.8 (c). We can observe a vessel wall radial ”tooth-appearance” due to the pulsatile pressure inflation.

2. **Induced external heart rotation**. In order to observe only the influence of heart rotation on the vessel wall longitudinal IVUS appearance, we have externally induced a pulsatile heart rotational movement at ≈ 1 Hz and ≈ 50 degrees of amplitude. Figure 2.9 (up) shows a longitudinal IVUS cut only using pulsatile inflation and Fig. 2.9 (down) shows a longitudinal cuts when an external induced heart rotation is applied.

3. **Rotation profile.** In order to estimate the IVUS image rotation only due to the radial inflation we used a constant diastolic Pc pressure at 80 $mmHg$ and a pulsatile systolic pressure $Pd(t)$ from 80 to 1500 $mmHg$ at 2.3 Hz. A pullback of 4500 images corresponding to ≈ 15 cm vessel long was made. The sequence was segmented by Neural Network procedure (See section 4.3.1) and the rotation profile was estimated using the procedure described by section 4.3.2. An elliptical approximation (Fig. 2.8 (b)) to the vessel wall was made in order to study the temporal evolution of lumen area, which was determined using the minor (a) and major (b) ellipse axis, as $A = \pi ab$. The rotation profile is shown in Fig 2.10 (b). The median and standard deviation values of rotation profiles

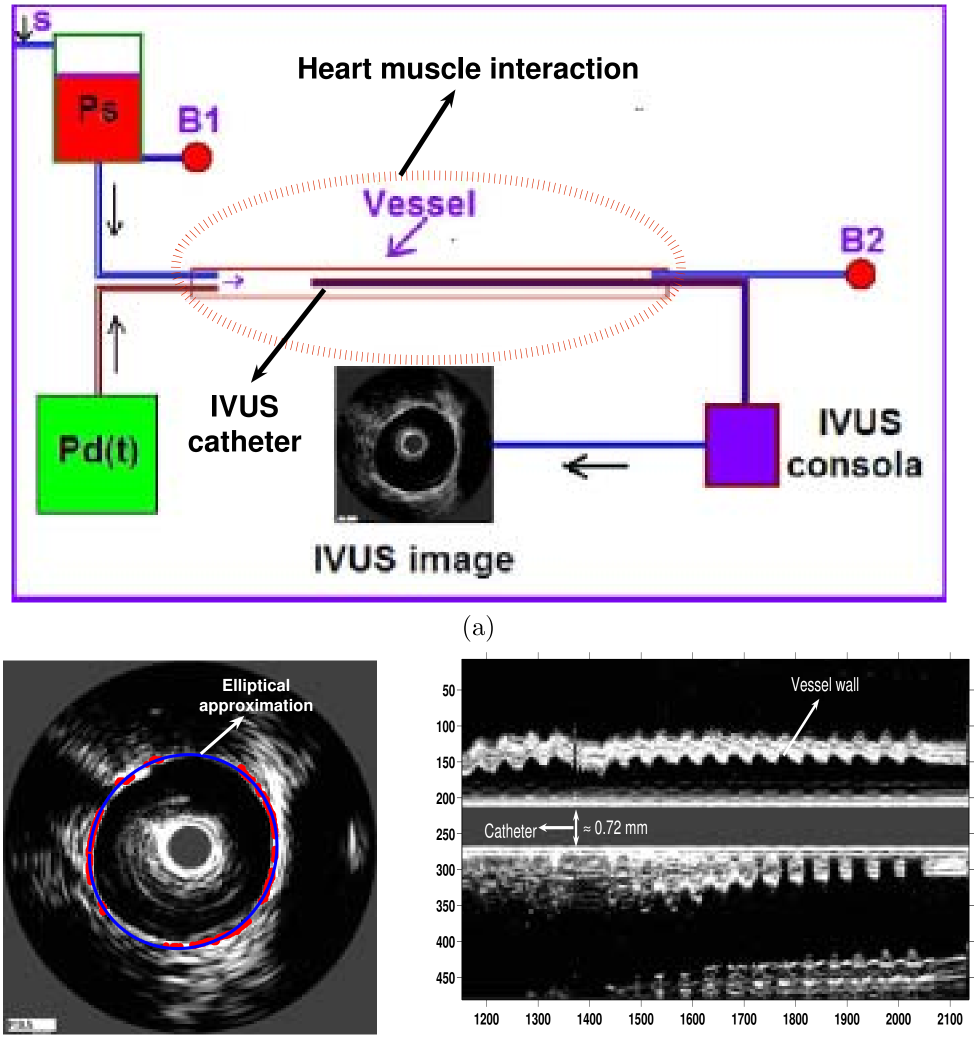

(a)

(b) (c)

Figure 2.8: Experimental setup (a). Vessel cross sectional image (b) of a calf healthy coronary artery, and its corresponding longitudinal IVUS cut (c).

($\mu = 0.1 \pm 6$) degrees, come from different factors: Inadequate segmentation, pulsatile spurious heart movement that can influence the rotation profile, small oscillating catheter movement due to the pulsatile mechanism that generates the pulsatile diastolic pressure and the mechanism (See 2) caused by the micro-fiber configuration.

Since the IVUS image rotation that comes from radial inflation is too small, we assume that the rotation due to fiber configuration can be negligible at

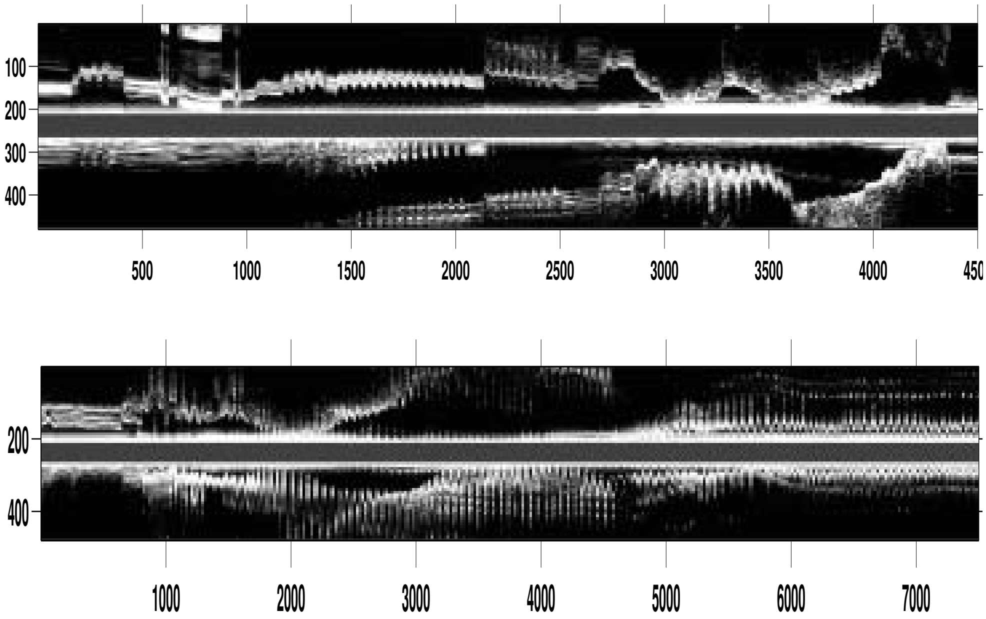

Figure 2.9: Longitudinal cut of healthy calf artery using only inflation (up). Using only induced external heart rotation (down).

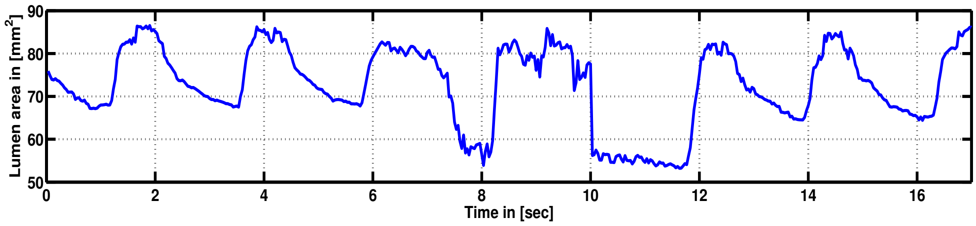

(a)

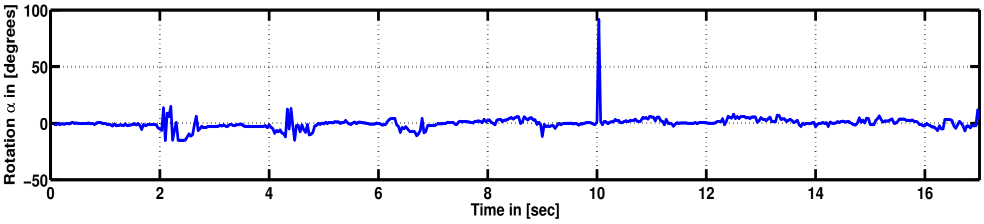

(b)

Figure 2.10: Lumen area temporal evolution of a calf coronary artery at pulsatile pressure from 80 to 1500 $mmHg$ (a). The vessel wall rotation profile (b).

pressure ranges from 80 to 140 $mmHg$, therefore, the vessel wall border can be modelled as a simple and isotropic membrane model [57, 58]. This result is very important in our geometrical vessel wall model construction since the vessel wall can be studied locally as an elliptical approximation only taken in to account its elastic membrane properties.

Other important result is the elastic constant κ that can be determined by the relation $\kappa = \Delta A/\Delta P$, where ΔA is the relative variation of lumen area and ΔP is the gradient pressure [19, 59, 57, 58]. In our experiment we used $\Delta P \approx (1500-80) \approx 1420$ $mmHg$. From figure 2.10 (a) we can see that $\Delta A \approx 20$ mm^2, using this result $\kappa \approx 0.014$ $mm^2/mmHg$. Assuming a linear elastic behavior we can hope that in the interval 80 to 140 $mmHg$ the relative variation of lumen area is approximately $\Delta A = \kappa \Delta P \approx 0.014 \times 60 \approx 0.84$ mm^2. That is approximately a 4% of the relative variation respect to the total vessel lumen, we assume that this variation can be negligible. This result is very important in our research, since, we can modell the IVUS vessel wall dynamic appearance from catheter point of view as independent from blood pressure, and only the rigid transformation: rotation plus translation that come from heart dynamics are taken into account (See Chapter 5).

Chapter 3

A Basic IVUS Image Model

3.1 Technical Aspects of the IVUS.

The images of ultrasound [46] are based on the reception and transmission of the high frequency sound waves. The transmitted wave propagates through the material until striking the reflecting object. The reflected wave returns and is received by the transducer. The time between the transmission and the reception of the wave is directly related to the distance between the source and the reflector. The advantage of the ultrasound is that it can travel through the water and of the smooth tissue. Additionally, the ultrasound is inoffensive at the used levels of energy for the generation of the image. A standard configuration of IVUS acquisition images consists of three components: Fig. 3.1 show a scheme of catheter with a piezoelectric transducer miniaturized, the pull-back unit and the console to reconstruct the images. IVUS catheter has a rank of measures that oscillates between 2,9 to 3,5 F (0,96 to 1,17 mm) of diameter. The quality of the image depends on the operation frequency, being this of the order of 20 to 50 MHz, the lateral resolution is approximately of the order of 113 μm and the axial resolution is of the order of 80 μm [11]. The IVUS images acquisition process, is initiated when the catheter is manually (guided by the angiography) inserted within the artery (Fig. 3.1 (a)). The catheter pullback is made at linear constant velocity (usually 0.5 mm/s) and constant angular velocity of 1800 rev/min. The pivoting transducer sends a radially focused beam of ultrasound and receives its corresponding echoes. The obtained radial lines for different transducer angular positions are adequately processed, giving as a result a 2D cross section artery image (Fig. 3.1 (d)). The sequence can be shown as a longitudinal sequence, which gives a longitudinal artery cut (Fig. 3.1 (e)). The resolution of a ultrasound image is directly related to the ultrasound signal frequency, high frequencies allow to obtain better resolution. Nevertheless, when increased the frequency, the attenuation of the waves of ultrasound increases while penetrating the biological tissue. The typical frequencies of the IVUS technique are in the rank of 20 to 50 MHz, with inferior resolutions of 50 μm.

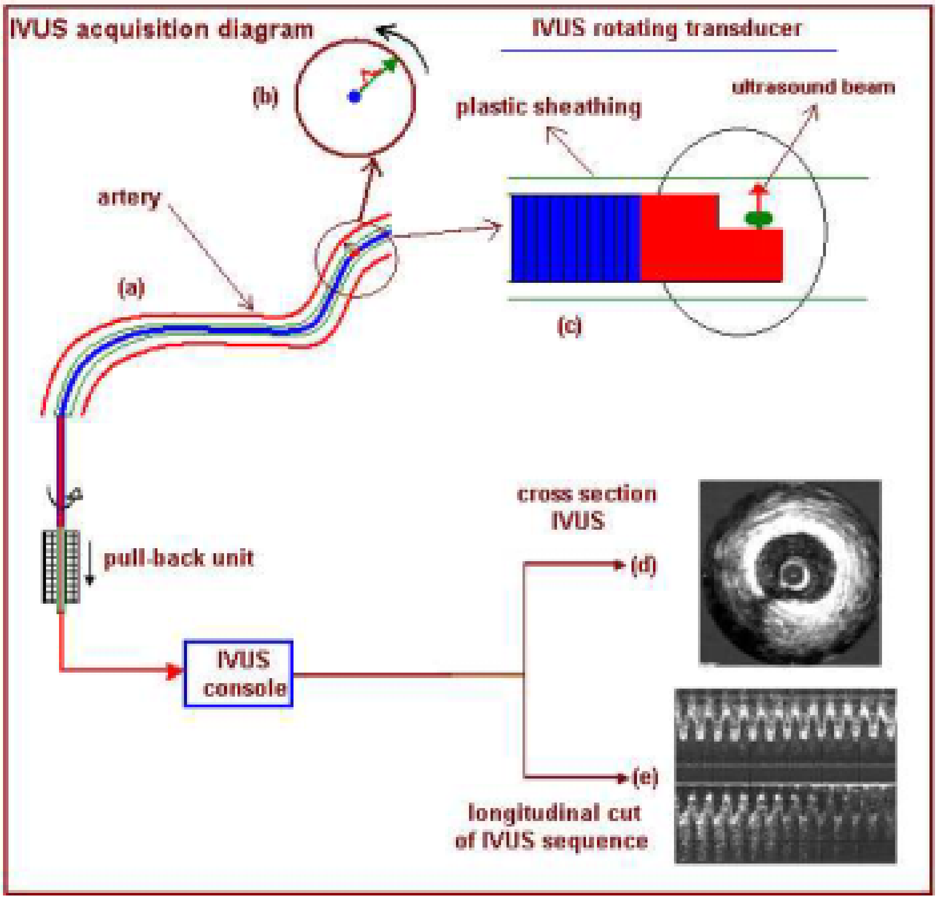

Figure 3.1: The IVUS catheter is manually positioned within the artery (a), it is extracted by a pullback unit at a constant linear velocity and rotated at a constant angular velocity. The information is transformed by the IVUS console as unique cross section artery grey levels image (d) or a longitudinal image sequence (e).

3.2 IVUS Model Objectives and Methodology.

Correct image processing needs of understanding image formation, grey level meaning, artifact causes, the averaging and the motion of the dynamics structures effects in the image. The generation of simulated IVUS images investigate four important objectives:

1. The generation, processing and visualization of the data in the format that the doctors use.
2. The exploration of some of the artifacts generated by the averaging of the beams.

3. The smoothing and treatment of the images to generate sufficient data for the validation of image processing algorithms.

4. Comparison of data generated by the image formation model to the real data.

The general methodology assume that the IVUS images can be obtained in a simulated form, from a simple physical model based on the transmission and reception of high frequency sound waves, when these radially penetrate a simulated arterial structure (Fig. 3.2). We assume for this model that the waves are emitted by a transducer located in the center of the artery, and that these waves propagate radially through the blood and the arterial structures (intima, media and adventitia), being reflected progressively by them. The reflected waves or echoes that return are received by the transducer, that now behaves as a receiver. The time between the emission and the reception of the waves is directly related to the distance between the source and the reflector (Fig. 3.3). The echo amplitude that is function of the time, is transformed on grey scale and later to penetration depth, so the radial coordinate is determined. If we place a rotatory transducer, make a registry of the corresponding echoes for each angular position of the transducer and combine all the lines obtained from different positions, as a result we will be able to obtain a simulated 2D image of the structure in study. The 3D IVUS simulated can be generated as a sequence of n-planes generated independently, taking into account the arterial deformation caused by the blood pulsatile pressure.

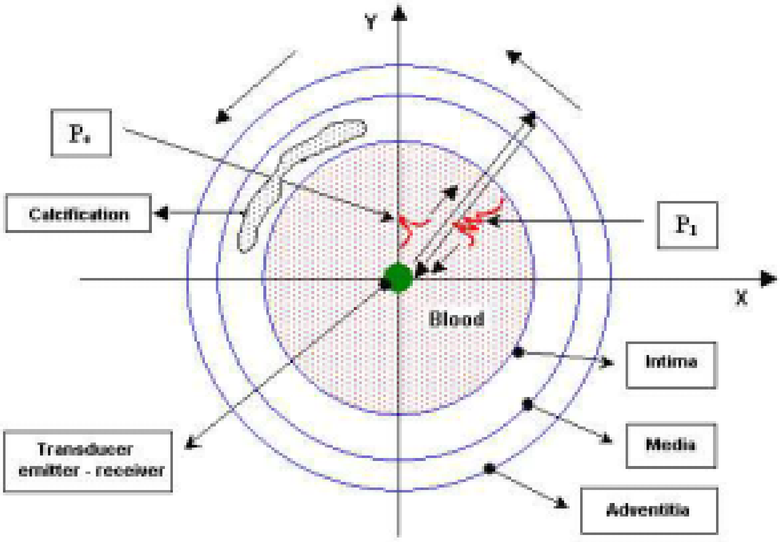

Figure 3.2: The disposition of the simulated arterial structures (blood, intima, media and adventitia) and calcification are illustrated. The ultrasound rotatory transducer which emits the pulse P_0 and receives pulse P_1 has been placed at the coordinate center.

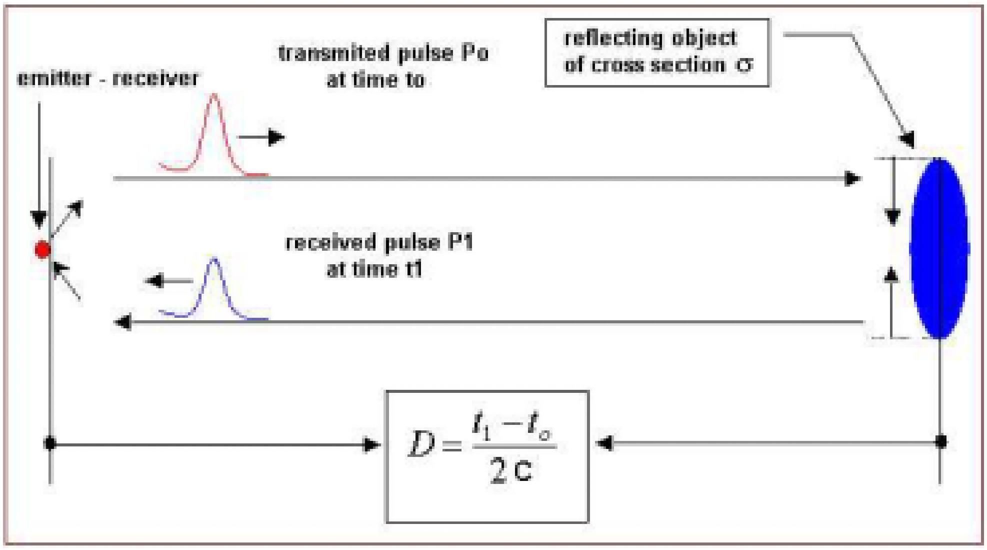

Figure 3.3: The determination of the distance D between the emitter/receiver and the reflecting object is done from the difference of time between the transmitted pulse P_0 and the received pulse P_1 assuming that the pulse speed c is constant.

3.3 Formal Definition of the Image Model.

Let us consider a ultrasound pulse P_0 that is emitted at time t_0 with speed c from the point with coordinates (r_0, θ_0, z_0) (Fig. 3.4), and that interacts with the scatterer located at the position, (R, Θ, Z) with the spatial distribution of the differential backscattering cross-section, $\sigma(R, \Theta, Z)$. The reflected pulse P_i for the i-th scatterer is an exact replica [12] of the transmitted sound pulse P_0 that will return to the point (r_0, θ_0, z_0) at time $(t_i - t_0)$ and will be out of phase temporarily with respect to the pulse P_0 by time difference $\delta = t_i - t_0$ between the emitted pulse at t_i and the received pulse at t_0. The time delay δ is given by:

$$\delta = \frac{2|R|}{c} \tag{3.1}$$

$$\overrightarrow{R} = \overrightarrow{r} - \overrightarrow{r_0} \quad , \quad \overrightarrow{r} = x\widehat{i} + y\widehat{j} + z\widehat{k} \quad , \quad \overrightarrow{r_0} = x_0\widehat{i} + y_0\widehat{j} + z_0\widehat{k}$$

We choose a coordinate system (X, Y, Z) with respect to the emitter/receiver position:

$$\overrightarrow{X} = (x - x_0)\widehat{i} \quad , \overrightarrow{Y} = (y - y_0)\widehat{j} \quad , \overrightarrow{Z} = (z - z_0)\widehat{k}$$

and the corresponding cylindrical coordinates given by

$$|R| = \sqrt{X^2 + Y^2 + Z^2} \quad , \Theta = \arctan(Y/X)$$

where $X = |\overrightarrow{X}|$, $Y = |\overrightarrow{Y}|$ and $Z = |\overrightarrow{Z}|$
Assuming the Born approximation [13, 14], the ultrasound reflected signal $S(t, \tau)$ for a

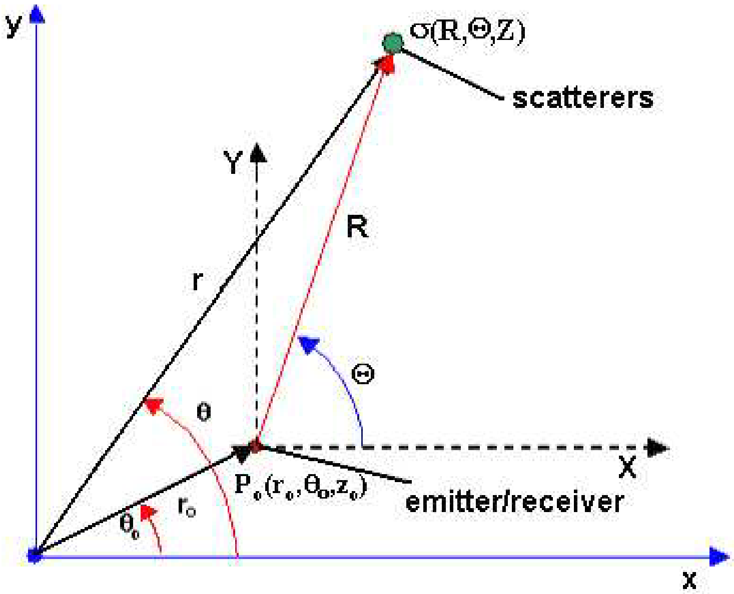

Figure 3.4: Coordinates system used with the corresponding ultrasound emitter/receiver and the scatterers localization.

finite set of N reflecting scatterers with coordinates (R, Θ, Z) and spatial distribution of the differential backscattering cross-section $\sigma(R, \Theta, Z)$ is given by:

$$S(R, \Theta, Z, t, \tau) = \sum_{i=1}^{N} \sigma_i(R, \Theta, Z)\Gamma_i(t, \tau) \tag{3.2}$$

where N is the number of scatterers, $\sigma_i(R, \Theta, Z)$ is the spatial distribution of the Differential Backscattering Cross-section (DBC) of the ith scatterer located in position (R, Θ, Z), $\Gamma_i(t, \tau)$ is the transducer impulse function and τ is the delay time which leads to constructive and destructive contributions to the received signal. The Born approximation implies that the scattered echoes are weak compared to the incident signal and it is possible to use the principle of superposition to represent the wave scattered by a collection of particles by adding their respective contribution.

3.3.1 The Ultrasound Pulse.

We consider a planar transducer that is mounted inside an infinite baffle, so that the ultrasound is only radiated in the forward direction. We assumed that the transducer is excited with uniform particle velocity across its face [15, 16]. According to the coordinates system illustrated in the far field circular transducer pressure $P(r, \theta, t)$ (Fig. 3.6) can be written as:

$$P(r, \theta, t) = j\frac{\rho_0 cka^2 v_0}{2r}\left[\frac{2J_1(ka\sin(\theta))}{ka\sin(\theta)}\right]exp(j(wt - kr)) \tag{3.3}$$

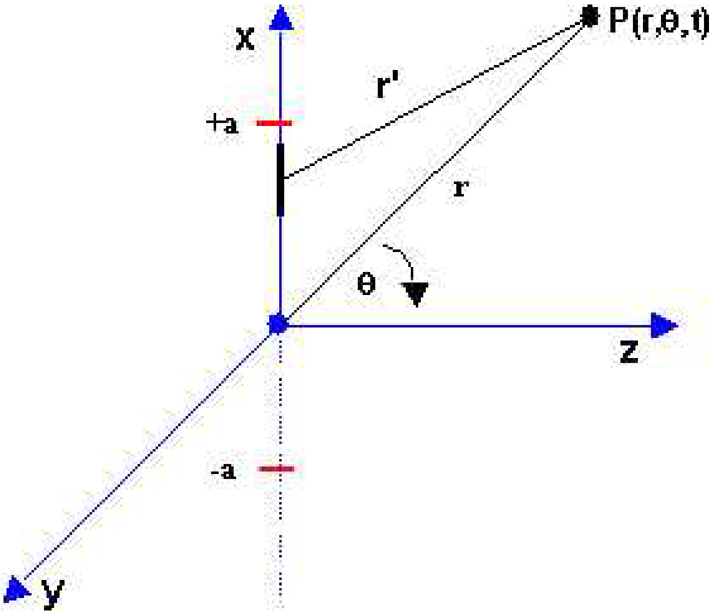

Figure 3.5: Geometrical variables used for the calculations of the pressure distributions $P(r, \theta, t)$ for a planar circular transducer of radius, a.

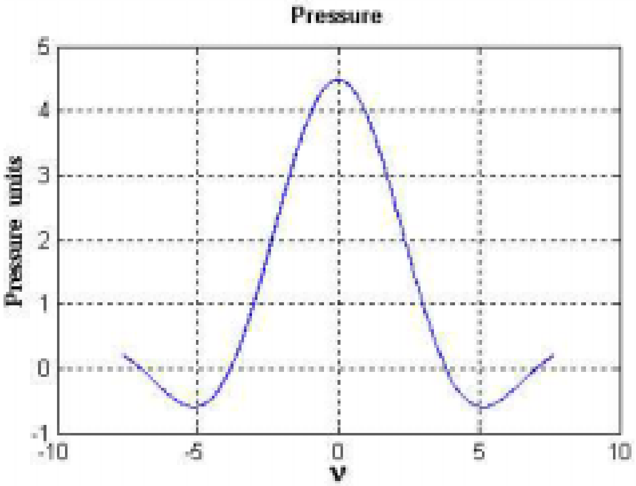

Figure 3.6: Transducer pressure distribution.

where t is the time, ρ_0 is the medium propagation density, c is the sound speed for biological tissue, (typically $c = 1540 m/s$), v_0 is the radial speed at a point of the transducer surface, a is the transducer radius, $\overrightarrow{k}$ is the propagation vector, defined as $k = |\overrightarrow{k}| = 2\pi/\lambda$, λ the ultrasound wave length, defined as $\lambda = c/fo$, f_0 ultrasound

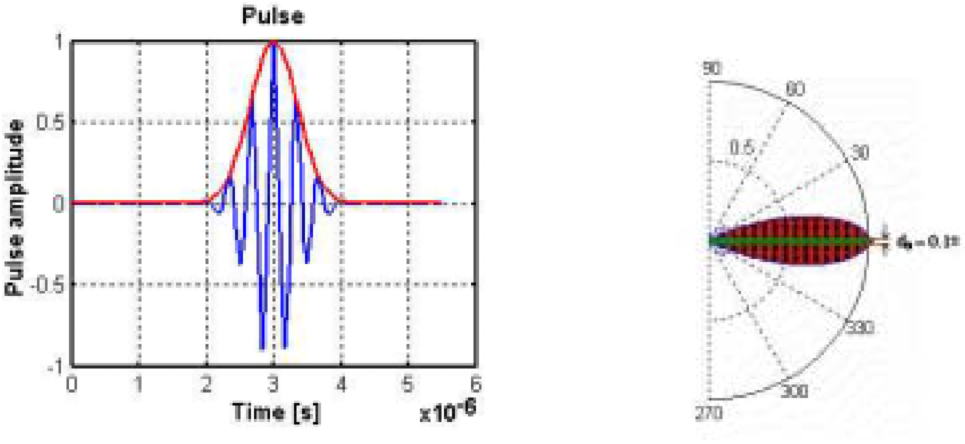

(a) (b)

Figure 3.7: Typical ultrasound pulse and its gaussian envelope (a). The transducer pattern radiation (b).

frequency, $\omega = 2\pi f_0$ and $J_1(x)$ is the first class Bessel function. Fig. 3.6 shows a graphics of the pressure as a function of ν, where $\nu = ka\sin(\theta)$. In some applications, particularly when discussing biological effects of ultrasound, it is useful to specify the acoustic intensity [18]. The intensity at a location in a ultrasound beam, I is proportional to the square of the pressure amplitude, P. The actual relationship is:

$$I(r,\theta,t) = \frac{P(r,\theta,t)^2}{2\rho c} \tag{3.4}$$

Again, ρ is the density of the medium and c the speed of the sound. The impulse function $\Gamma(t,\delta)$ is generally approximated [17] by a Gaussian (Fig. 3.7 (a)) which envelopes the intensity distribution given by:

$$\Gamma(t,\delta) = I(r,\theta,t)\exp\Big(-\frac{(t-\delta)^2}{2\sigma^2}\Big) \tag{3.5}$$

where σ is the pulse standard deviation. We consider that the beam is collimated by $\theta = \theta_a$. In our model only the corresponding interval $d\theta \approx 0.1^{\circ}$ is used that corresponds to the transducer lateral resolution zone (Fig. 3.7 (b)). Hence Eq. (3.2) in the transducer coordinate system is based on a discrete representation of the tissue of individual scatterer elements with given position and DBC with respect to the transducer coordinates given by:

$$S(R,\Theta,Z,t,\delta) = C_0\sum_{i=1}^{N}\frac{\sigma_i(R,\Theta,Z)}{|R_i|}\Gamma(t,\delta) \tag{3.6}$$

where δ is given by Eq. (3.1), $\Gamma(t,\delta)$ is the impulse function given by Eq. (3.5). If we consider only the axial intensity contributions, C_0 can be written as [16]:

$$C_0 = \frac{\rho_0 c k^2 v_0^2 A}{8\pi} \tag{3.7}$$

where A is the transducer area.

3.4 Principal Features of IVUS Data.

3.4.1 Image Resolution.

The resolution is the capacity that has a technique or an instrument to separate in time and/or space two events or objects [16]. At the moment, most of the efforts in the design of new transducers are centered in improving the spatial and the temporal resolution. Unfortunately most of the medical applications demand that the transducers are smaller to increase the resolution but it diminishes their capacity to explore to greater tissues depth. For the IVUS techniques, the resolution plays a very important role since most of the structures to visualize directly depend of these parameters.

Axial Resolution.

The axial resolution is the capacity that the ultrasound technique has to separate the spatial position of two consecutive scatterers through its corresponding echoes [15, 16, 18]. In Fig. 3.8 a ultrasound pulse P_1 that has a width d_1 frontally affects a linear scatterer array at distance d_{oi}. Each one of the echoes forms a "train"

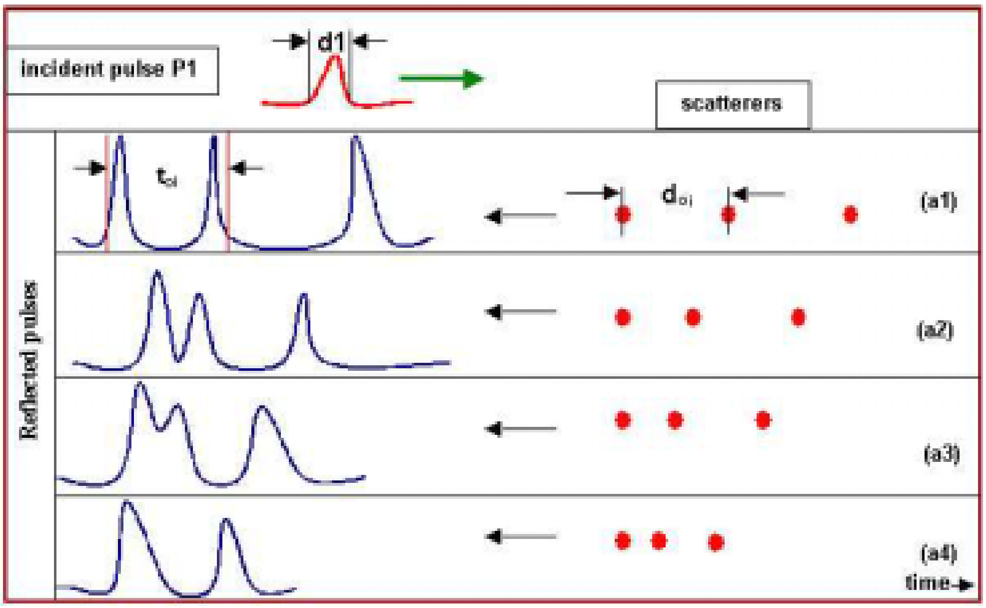

Figure 3.8: A ultrasound pulse, P_1 that has width, d_1 frontally affects a linear scatterer array placed at distance d_{oi}.

of pulses temporally distanced according to the equation $t_{oi} = 2|R_i|/c$, being R_i the ith relative emitter/scatterer distance and c the pulse propagation speed. The progressive distance reduction of the linear scatterers, given by $(a_1, ..., a_4)$ (Fig. 3.8) and $(b_1, ..., b_4)$ (Fig. 3.9), reduces the time between the maximums of the "trains" pulses. There exists a critical distance width d_t from which the pulses that arrive at the receiver are superposed, not being able, therefore, to discriminate or to separate individually the echoes produced by each scatterer. In Fig. 3.9 one can observe, that the resolution can be improved by diminishing the pulse width d_t, which is equivalent to increasing the frequency of the emitted pulse. The axial resolution of this technique depends essentially on two factors: **the ultrasound speed** c and **pulse duration** d_t. The functional dependency between the spatial resolution, the frequency and the ultrasound speed propagation is given by:

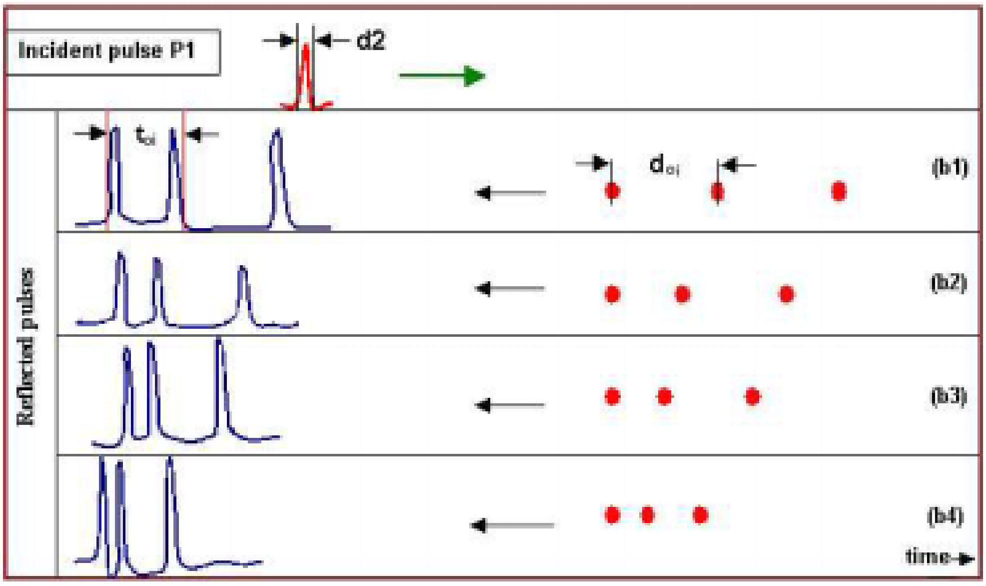

Figure 3.9: We can see that the progressive distance reduction of the linear scatterers, from $(a_1, ..., a_4)$ (Fig. 3.8) to $(b_1, ..., b_4)$ reduces the time difference between the maximums of the "train" pulses. The maximums can be separated reducing the pulse width from d_1 (Fig. 3.8) to d_2, this is equivalent to an increase in the pulse frequency.

$$d_r = cd_t = cT = \frac{c}{f} \tag{3.8}$$

where d_r is the axial resolution, c is the ultrasound speed for biological tissues, d_t is the pulse width, T is the period of ultrasound wave and f is the ultrasound frequency. For the IVUS, the typical values are: $c = 1540$ m/seg and $f = 30$ MHz the axial resolution is approximately: $d_r = 1540/(30 \times 10^6) = 0.05$ mm $\approx 50\mu m$ and the relative error of the axial resolution is given by:

$$\frac{\Delta d_r}{d_r} = \left|\frac{\Delta c}{c}\right| + \left|\frac{\Delta f}{f}\right| \tag{3.9}$$

The axial resolution dependency versus the ultrasound frequency is visualized in Fig. 3.10.

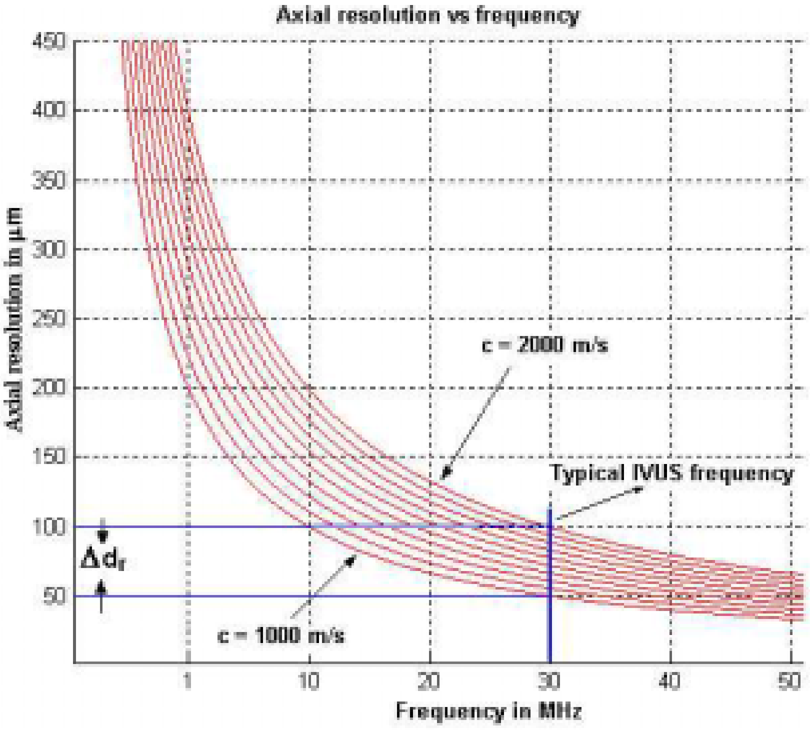

Figure 3.10: The functional dependency between the axial resolution and the ultrasound frequency for a rank of typical ultrasound speeds in biological tissue. The typical IVUS ($30MHz$) frequency as well as the tolerance in the axial resolution Δd_r are emphasized.

Angular Resolution.

The angular resolution is the capacity to discern two objects or events located in the tangential direction [15, 16, 18] and depends on the ***Beam width.*** The beam width depends on the transducer effective emission area (Fig. 3.11). The Fig. 3.12 shows the standard dimensions of typical IVUS ultrasound transducer. The tangential or lateral resolution of a ultrasound emitter of diameter, D that emits by frequency f is

Material	**Sound speed** (m/s)
Fat	1460
Aqueous humor	1510
Liver	1555
Blood	1560
Kidney	1565
Muscle	1600
Lens of eye	1620
Average	1553

Table 3.1: Sound speed in selected tissues [18]

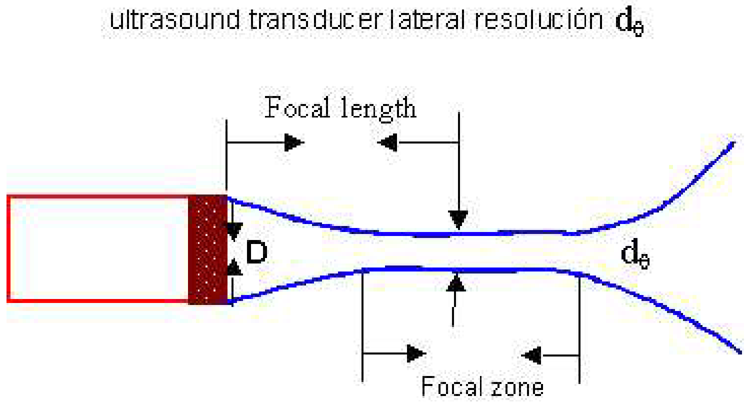

Figure 3.11: The focal length and the focal zone of a ultrasound transducer are indicated. The transducer lateral resolution d_θ is a function of its diameter, D and the emission frequency, f.

given by:

$$d_\theta = 1.22\frac{\lambda}{D} \ , \ d_\theta = 1.22\frac{c}{D}\frac{1}{f}$$

and the focal distance (focal length) F is given by:

$$F = \frac{1}{4}\frac{D^2}{\lambda} \tag{3.10}$$

where $\lambda = c/f$ and D is the transducer diameter. For a typical transducer of 30 MHz, $c = 1540$ m/seg and transducer dimensions given in Fig. 3.12, the lateral resolution is $d_\theta \approx 0.10^{\circ}$ and the focal length is $F = 2$ mm.

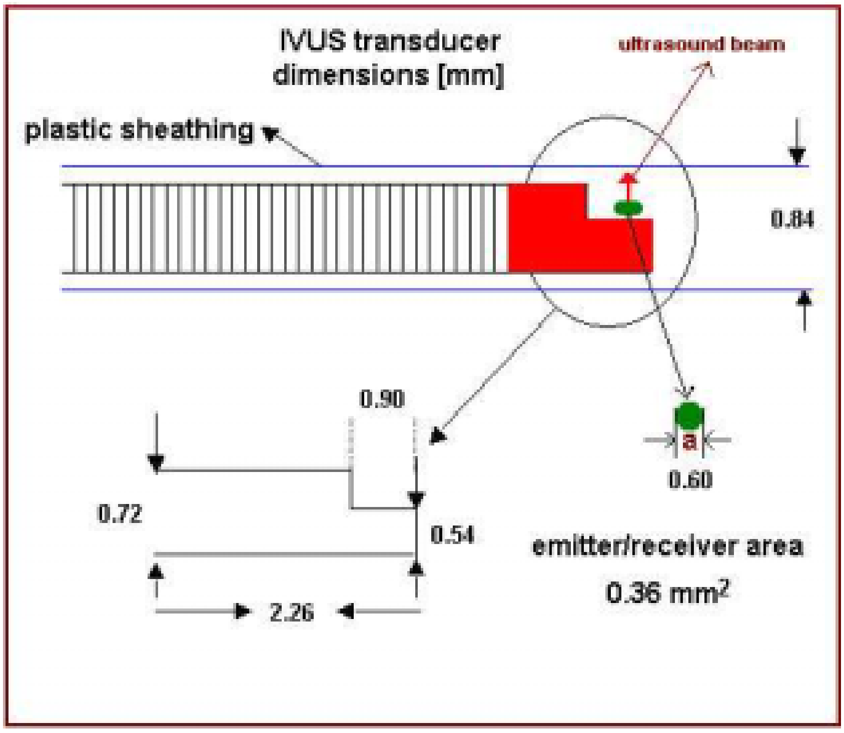

Figure 3.12: Typical IVUS transducer dimension used by Boston Sci.

3.4.2 The Beam Intensity.

The beam ultrasound intensity, as a function of the penetration depth and the ultrasound frequency, is given by [15, 16, 18]:

$$I(r) = I_0 exp\big(-\zeta(N_\theta) r f\big) \tag{3.11}$$

where I_0 is the beam intensity at $r = 0$ and the coefficient, ζ gives the rate of diminution of average power with respect to the distance along a transmission path [45]. It is composed of two parts, one (absorption) proportional to the frequency, the other (scattering) dependent on the ratio of grain, particle size or the scatterer number N_θ located along the ultrasound beam path (See section 3.5.2). Since the attenuation is frequency dependent, a single attenuation coefficient only applies to a single frequency. The attenuation coefficient of ultrasound ζ is measured in units of dB/cm, which is the log relative energy loss per travelled centimeter. In biological soft tissues, the ultrasound attenuation coefficient is roughly proportional to the ultrasound frequency (for the frequency range used in medical imaging). This means that the attenuation coefficient divided by the frequency (unit $dB/MHz \times cm$) is nearly constant in a given tissue. Typical soft tissue values are 0.5 to 1.0 $dB/MHz \times cm$. In our model we assumed that the attenuation coefficient α is only dependent on the scatterer number in the length way beam. Fig. 3.13 shows the beam intensity dependence vs penetration depth for several typical frequencies used by IVUS.

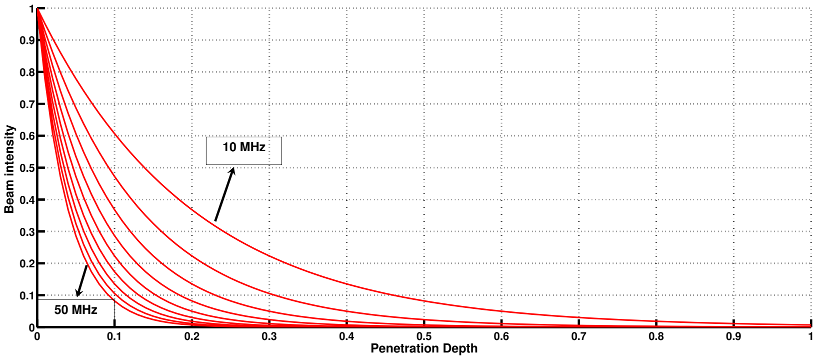

Figure 3.13: Ultrasound beam intensity versus the penetration depth for several frequencies (10 to 50 MHz).

3.4.3 Ultrasound Beam Sweeping Criterion.

Let us explore a criterion that assures that all the return echoes reach the transducer before it moves to the following angular position. Let us define β as the ratio between transducer diameter, D and length arc, ϵ (Fig. 3.14):

$$\beta = \frac{D}{\epsilon} \tag{3.12}$$

where D is the transducer diameter and ϵ is the arc segment swept by the beam, between two angular consecutive positions. Note that:

$$d_\theta = \omega d_t \ , \quad d_t = 2\frac{R}{c} \ , \quad \epsilon = R d_\theta \tag{3.13}$$

Taking into account these definitions, β can be rewritten as:

$$\beta = \left(\frac{r}{R^2}\right)\left(\frac{c}{\omega}\right) \tag{3.14}$$

where r is the transducer radius, R is the maximum penetration depth, c is the ultrasound speed and ω is the transducer angular speed. The parameter β implies that the transducer area is β times the sweeping area for the rotatory beam and the maximal depth penetration. This assures that a high percentage of echoes incomes to the transducer before it changes to the following angular position. We can determine parameter β by calculating the frequency by which the ultrasound pulse should be emitted. Fig. 3.15 shows the dependence between parameter β and the transducer angular velocity for several typical velocities in biological tissues. We emphasize the typical IVUS transducer angular velocity. Fig. 3.16 gives the relation between the sample frequency ($f_m = 1/d_t$) and the typical IVUS transducer angular velocity ω.

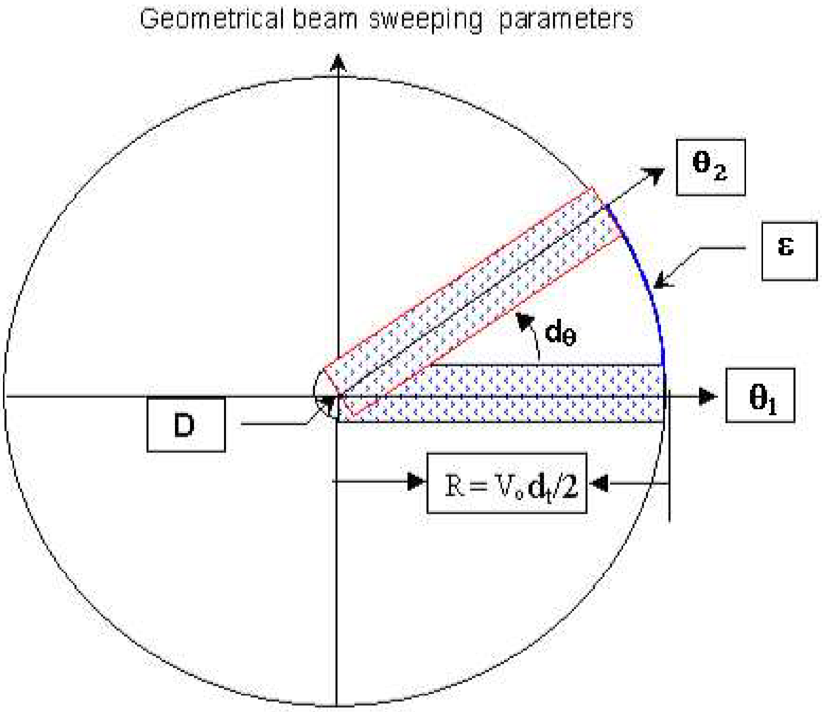

Figure 3.14: A rotatory transducer emits a radially focused beam. Angular positions, θ_1 and θ_2 define a segment of arc ϵ which can be calculated from the speed of rotation and the speed of propagation of the ultrasound beam.

3.4.4 Determining the Scatterer Number of Arterial Structures.

1) The **Red Blood Cells (RBC's) number** swept by the ultrasound beam (Fig. 3.17) can be estimated taking into account the plastic sheathing dimensions of the transducer (Fig. 3.12) and the typical arterial lumen diameter. The scatterer number contained in a sweeping beam volume is given by the difference between the sweeping lumen arterial volume, V_a and the plastic sheathing transducer volume, V_t.

$$V_b = V_a - V_t = \pi a(D^2 - D_M^2)/4 \tag{3.15}$$

where D and D_M are the arterial lumen and the sheathing transducer exterior diameters respectively, and a is the effective emission diameter of the transducer. Typical arterial lumen diameter of coronary arteries is $D \approx 3mm$ [48, 19]. From Fig. 3.12 we can see that $D_M \approx 0.84mm$ and $a = 0.60mm$. Using Eq. (3.15) we obtain for the sweeping volume of the transducer beam approximately $V_b \approx 3.91mm^3$. The RBC's can be approximated by spherical scatterers having volume of $87\mu m^3$ [20], which corresponds to a radius of $2.75\mu m$ (diameter, $d_g = 5.5\ \mu m$). Considering a typical hematocrit concentration [21] of 35% we can estimate the RBC's number by the

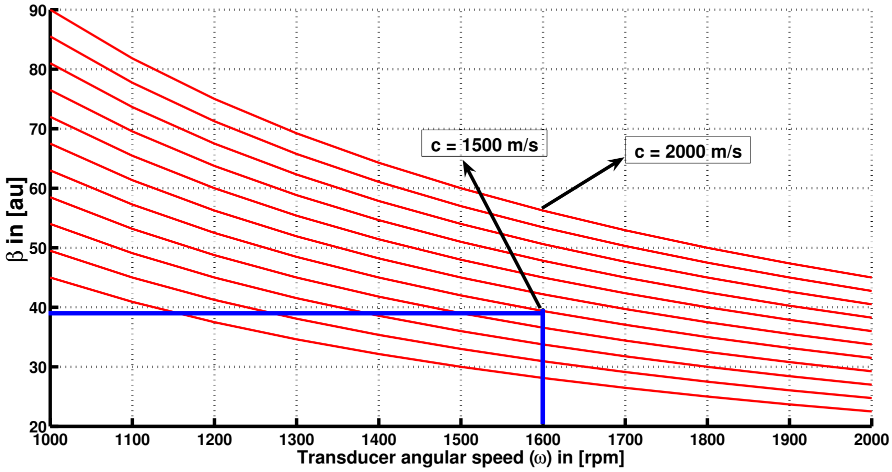

Figure 3.15: Functional dependence between parameter, β and transducer angular speed,(ω)

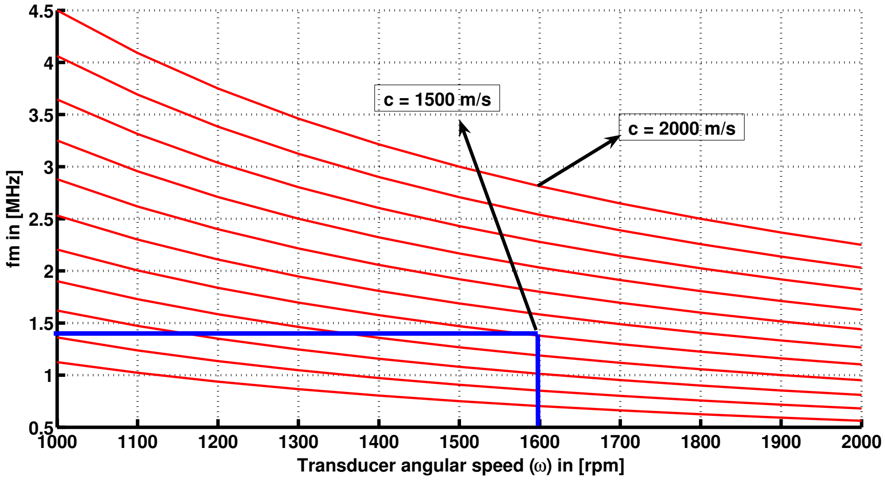

Figure 3.16: Functional dependence between the sample frequency (fm) and the transducer angular speed, (ω).

beam sweeping volume. The RBC's sweeping volume is $V_{rbc} = 1.36\ mm^3$, and the typical human RBC's number is approximately $N \approx 4.1 \times 10^6\ cells/mm^3$ [21]. Thus, the RBC's number by the sweeping volume is $N_0 \approx 5.61 \times 10^6$ cells. The maximal axial resolution at $40MHz$ is approximately $d_r = 38\mu m$, at this resolution we can observe the order of $d_r/d_g \approx 7$ RBC's. If we take the scatterers as perfect spheres with radius d_r at maximal axial resolution, we would have of order of 1.37×10^7 scatterers to be simulated. This quantity of RBC's scatterers is not possible to estimate with the actual computer possibilities. In order to generate quantities of scatterer

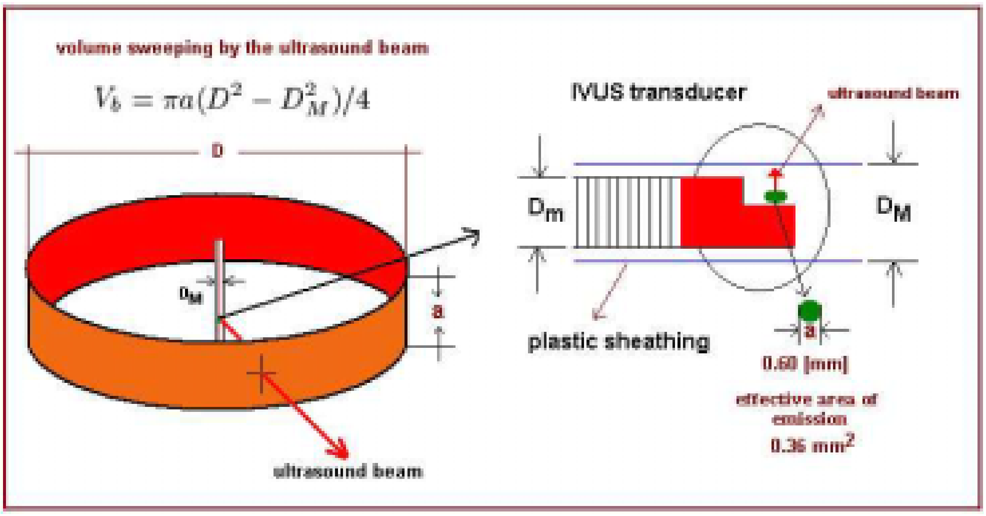

Figure 3.17: The scatterers volume for each arterial structure can be calculated taken into account the total volume V_b swept by the ultrasound beam.

possible to emulate, we generate scatterers groups namely "voxel" [13]. In Table 3.2, the most important numerical data used by this simulation model are summarized. The minimal structure dimensions able to be measured by an IVUS image at 40 MHz

feature	**≈ values**
Arterial diameter	$D = 3$ [mm]
Sheathing transducer diameter	$D_M = 0.84$ [mm]
Transducer diameter	$a = 0.60$ [mm]
Sweeping volume by the beam	$V_b = 3.91$ $[mm^3]$
RBC volume	87 $[\mu m^3]$
Hematocrit concentration	35 %
RBC volume by 35 % of V_b	1.36 $[mm^3]$
Typical human RBC number	$N = 4.1 \times 10^6$ $[cells/mm^3]$
Maximal axial resolution at 40 MHz	$d_r = 38$ $[\mu m]$
IVUS image resolution	$(1/25) \approx 0.04$ $[mm/pixel]$
Minimal voxel volume	6.4×10^{-5} $[mm^3]$
Total RBC voxel	360 [voxels]
RBC voxel to be emulated	1.5×10^4 [voxels]

Table 3.2: Important features and the corresponding approximated values used in this simulation model.

is 1/25 $[mm/pixel] \approx 0.04$ mm. We take this dimension to estimate the minimal "voxel" volume. For the RBC's, $V_0 = 0.04 \times 0.04 \times 0.04 \approx 6.4 \times 10^{-5}$ mm^3. The total number of RBC's per voxel is $N_t = V_0 \times N \approx 360$ $cells/voxel$. Now, we can calculate the total RBC's "voxel" number $N_{rbc} = N_0/N_t \approx 1.5 \times 10^4$ *voxels* for the sweeping volume by the ultrasound beam. This "voxel" number is even computer intractable. Therefore, we must consider that the typical structure dimensions able to be measured by IVUS image are greater than 0.04 mm. A well contrasted image structure by IVUS begins from 0.06 mm. Using these "voxel" dimensions, $V_0 = 2.14 \times 10^{-4} mm^3$, the total "voxel" number is $N_t \approx 880$ $[cells/voxel]$ and the RBC "voxels" number is approximately $N_1 \approx 6200$ [voxels]. An example of RBC's "voxel" number used in this simulation is given in table 3.3.

2) **The intima, media and adventitia**. The numerical values necessary for the evaluation of the scatterer number for the intima, media and adventitia were taken from results of L. T. Perelman et. al [22], that give the typical nuclear cells size $l(\mu m)$ distribution for human cells. The "voxel" number for each layer was computed taken into account the typical dimensions of intima, media and adventitia of a normal artery.

3) **The voxel number for the sheathing transducer** was calculated taking into account the minimal scatterers able to be observed at maximal resolution when the frequency is fixed at $40MHz$, a typical IVUS frequency. From Fig. 3.12 and Fig. 3.17, the transducer sweeping volume is $V_t = \pi a(D_M^2 - D_m^2)/4$, where, $a \approx 0.60$ mm is the transducer diameter, $D_M \approx 0.84$ mm and $D_m \approx 0.72$ mm are the exterior and interior transducer sheathing diameters respectively. Using these dimensions: $V_t \approx 0.08$ mm^3. The sheathing "voxel" number N_0 can be calculated as $N_0 = V_t/V_0$, where $V_t \approx 0.08$ mm^3 is the sheathing volume by the beam and $V_0 = 4\pi d_r^3/3$ is formed by the minimal spherical scatterers with radius $d_r = c/f$ able to be measured when the frequency f and the ultrasound speed c are known. Taken typical values for $c = 1540$ m/s and frequency 40 MHz, $V_0 \approx 2.39 \times 10^{-4}$ mm^3, thus $N_0 \approx 370$ "voxels".

3.5 Simulation of IVUS Image.

3.5.1 Generation of the Simulated Arterial Structure.

Considering the goal of simulating different arterial structures, we can classify them in 3 groups: Tissue structures, non tissue structures and artifacts. The spatial distribution of the scatterer number with a given DBC, $\sigma(R, \Theta, Z)$ at point $(R_, \Theta, Z)$ has the following contributions:

$$\sigma(R, \Theta, Z) = A(R) + B(R, \Theta, Z) + C(R) \tag{3.16}$$

where A(R), B(R,θ,Z) and C(R) are the contributions of tissue structures, non tissue structures and artifacts respectively.

1. ***Tissue scatterers***. These are determined by the contribution of the normal artery structures, corresponding to: *lumen, intima, media and adventitia.* Fig. 3.18 shows a k-layers spatial distribution of the scatterers for a simulated arterial image. These scatterers are simulated as radial gaussian distributions [23] centered in the average radius R_k and having standard deviation η_k corresponding

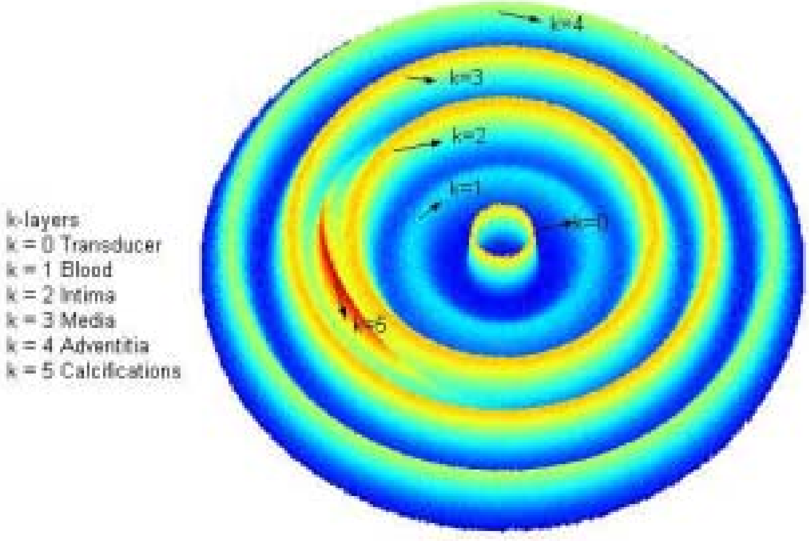

Figure 3.18: A plane of k-layers simulated artery. The scatterer numbers are represented by the height coordinate in the figure.

to each arterial structures. Tissue scatterers are represented by:

$$A(R) = \sum_{k=1}^{k_0} \frac{a_k}{\eta_k} \exp\Big(- \frac{(R - R_k)^2}{2\eta_k^2} \Big) \tag{3.17}$$

where a_k is the maximal number of scatterers at $R = R_k$, k is the k-th radial simulated tissue layer and R_k is the radial layer average position.

2. ***Non tissue scatterers***. These contributions can be originated by structures formed by spatial calcium accumulation, which are characterized because the DBC density is greater than the rest of the arterial structures. They are simulated by a gaussian distribution in the radial, angular and longitudinal arterial position of the simulated structure:

$$B(R, \Theta, Z) = \sum_{l=1}^{l_0} \sum_{m=1}^{m_0} \sum_{n=1}^{n_0} \frac{b_l c_m d_n}{\beta_l \gamma_m \nu_n} F(R, \Theta, Z)$$

$$F(R, \Theta, Z) = \exp\left(-\frac{1}{2} \Big(\frac{(R - \overline{R}_l)^2}{\beta_l^2} + \frac{(\Theta - \overline{\Theta}_m)^2}{\gamma_m^2} + \frac{(Z - \overline{Z}_n)^2}{\nu_n^2} \Big) \right)$$

where (l, m, n) correspond to the radial, angular and longitudinal axes directions, (l_0, m_0, n_0) are the structures number in radial, angular and longitudinal direction, (b_l, c_m, d_n) are the scatterer numbers that have a maximum at $R = R_l, \Theta = \Theta_m$ and $Z = Z_n$, $(\beta_l, \gamma_m, \nu_n)$ are the radial, angular and longitudinal standard deviation and (R_l, Θ_m, Z_n) are the radial, angular and longitudinal average position.

3. ***Artifacts scatterers.*** In our model we consider the artifact caused by the sheathing transducer:

$$C(R) = \frac{a_0}{\alpha_0} \exp\Big(- \frac{(R - R_0)^2}{2\alpha_0^2} \Big) \tag{3.18}$$

where a_0 is the scatterers number that has a maximum at $R = R_0$, α_0 is the artifact standard deviation and R_0 is the artifact radial average position.

3.5.2 1D Echogram Generation.

To obtain an 1D echogram, a ultrasound pulse is generated by Eq. (3.5) and it is emitted from the transducer position. The pulse moves axially through scatterers (Fig. 3.19 (a)), its intensity distribution decreases (Fig. 3.19 (b)), with the penetration depth and the scatterers numbers on the ultrasound way according to the Eq. (3.11). The echo amplitude is registered by the transducers (Fig. 3.20) as a signal function of time $S(t)$ (Eq. 3.19). The value is transformed to penetration depth replacing $t = x/c$ and normalized to grey scale. The spatial distribution of cross section scatterers, σ is generated by using Eq. (3.16). Fig. 3.19 shows the simulations of N scatterers located in $(R_i, \Theta_a \leq \Theta_j \leq \Theta_b)$.

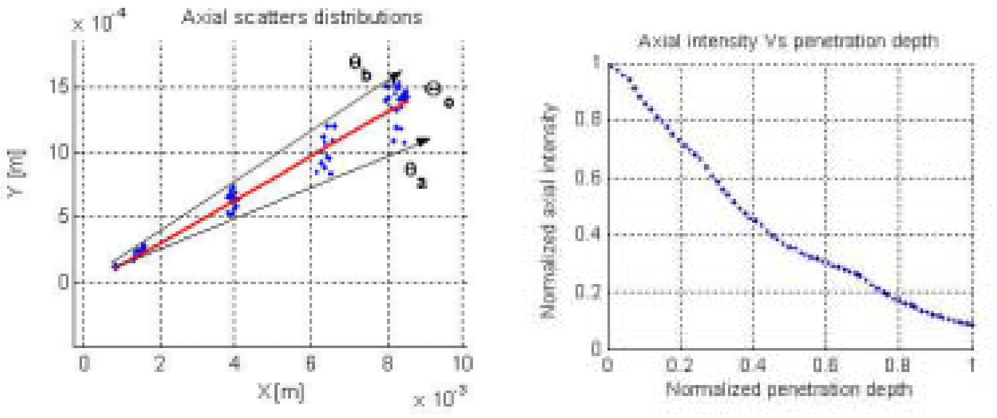

(a) (b)

Figure 3.19: The 1D echogram is obtained by fixing the angular position $\Theta_0 = \overline{\Theta}$ of the ultrasound beam (a). The total signal $S(t)$ is only generated by the scatterers N_Θ located in the angular position between $\Theta_a \leq \Theta_0 \leq \Theta_b$. The intensity distribution decreases with the depth penetration and the scatterers numbers N_Θ through the beam way (b).

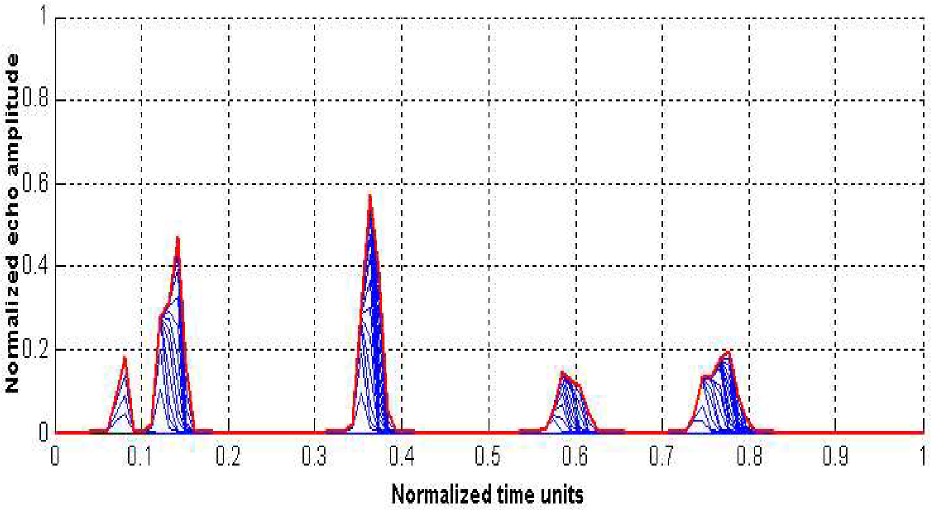

Figure 3.20: The corresponding echoes are finally transformed to normalized echo amplitude and then to grey level scale vs time or penetration depth.

$$S(t,\Theta_0) = \sum_{i=1}^{N_R}\sum_{j=1}^{N_{\Theta_i}} \frac{\sigma(R_i,\Theta_0 \pm \Theta_j)\Gamma(t,\delta_i)}{|R_i|} \tag{3.19}$$

$$S(t,\Theta_0) = C_0 \sum_{i=1}^{N_R}\sum_{j=1}^{N_{\theta_i}} \frac{\sigma(R_i,\Theta_0 \pm \Theta_j)}{|R_i|} \exp\left(\frac{-(t-\delta_i)^2}{2\sigma^2}\right)\sin(\omega t - \delta_i) \tag{3.20}$$

where $\Theta_0 = (\Theta_a + \Theta_b)/2$, C_0 defines the transducer constant parameters and N_{Θ_i} is the total scatterer number in the angular position between $\theta_a \leq \Theta \leq \theta_b$ for a radial position R_i. The sum only operates on the scatterers located between the angular position $\theta_a \leq \Theta \leq \theta_b$ that is the focal transducer zone (Fig. 3.7 (b) and Fig. 3.11). Therefore, N_Θ is the total scatterers number in this region. Eq. (3.19) can be written as a function of the penetration depth, replacing $t = x/c$. Eq. (3.19) can be rewritten on grey-level scale as:

$$S(t,\Theta_0) = \frac{256}{max(S(t))} C_0 \sum_{i=1}^{N_R}\sum_{j=1}^{N_{\theta_i}} \frac{\sigma(R_i,\Theta_0 \pm \Theta_j)}{|R_i|} \exp\left(\frac{-(t-\delta_i)^2}{2\sigma^2}\right)\sin(\omega t - \delta_i) \tag{3.21}$$

where $\delta_i = 2R_i/c$ and $S(x)$ is the 1D echogram generated by a set of N_Θ scatterers located in $(R_i, \Theta_a \leq \Theta_i \leq \Theta_b)$. The overall distribution backscattering cross section, $\sigma_i(R_i, \Theta_i \pm \delta\Theta)$ is given by (Eq. 3.16).

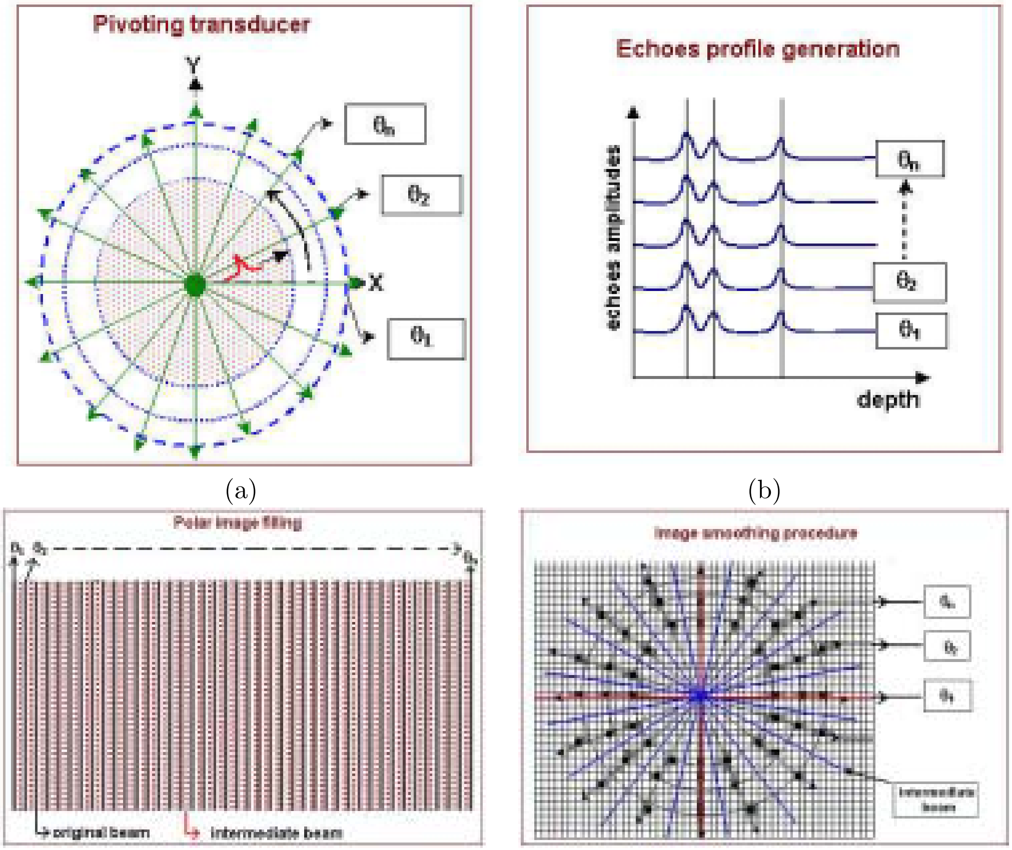

(a) (b)

(c) (d)

Figure 3.21: The transducer emits from the artery center (a), echo profile transformed into penetration depth (b), the echo profiles are transformed to a polar image (c), empty pixels filled and the final IVUS image is smoothed (d).

3.5.3 2D Echogram Generation.

The procedure to obtain the 2D simulated IVUS is the following: A rotatory transducer at angular velocity, ω (Fig. 3.21 (a)) is located at the center of the simulated arterial configuration given by Eq. (3.16). The transducer emits a ultrasound pulse radially focused at frequency, f_0 along angular direction, θ_1 (Fig. 3.21 (a)). The pulse progressively penetrates each one of the layers of the simulated arterial structure according to Eq. (3.13). Each one of the layers generates a profile of amplitude or echoes in the time, that can be transformed into a profile of amplitude as a function of the penetration depth (Fig. 3.21 (b)). Therefore, the depth can be calculated by Eq. (3.1). As the penetration depth is coincident with the axial beam direction, the radial coordinate, R is thus determined. This procedure is made n-times for the angles, $(\theta_1, ..., \theta_n)$ and the 2D image is generated. The generated echo profiles are transformed to a polar image, and the intermediate beams are computed (Fig. 3.21(c)). The image is transformed to cartesian form and the empty pixels are filled (Fig. 3.21(d)).

Using the ultrasound reflected signal $S(t, \Theta)$ for a finite set of N reflecting scatterer with coordinates (R, Θ, Z) and spatial distribution of the differential backscattering cross-section, $\sigma(R, \Theta, Z)$, the 2D echo signal $S(t, \Theta)$ can be written as:

$$S(t, \Theta) = C_0 \sum_{i=1}^{N_R} \sum_{j=1}^{N_{\theta_i}} \frac{\sigma(R_i, \Theta \pm \theta_j)\Gamma(t, \delta_i)}{|R_i|} \tag{3.22}$$

where $S(t, \Theta)$ is the temporally generated signal by a set N_R of scatterer which are localized in angular position θ, $\theta \in [\theta_a, \theta_b]$, N_{θ_i} is the total scatterer number in the angular position between $\theta_a \leq \overline{\Theta} \leq \theta_b$ for a radial position R_i. We consider two forms of $\overline{\Theta}$:

- by no uniform distributed scatterers:

$$\overline{\Theta} = (\theta_a + \theta_b)/2 \tag{3.23}$$

- by uniform distributed scatterers:

$$\overline{\Theta} = \frac{1}{N_R} \sum_{j=1}^{N_R} \Theta_j \tag{3.24}$$

3.5.4 Final Image Processing.

The actual image obtained only with the original beams is very poor, we must explore several smoothing procedures to improve the image appearance. The procedures to obtain the final simulated image are as follows:

1. The echoes are obtained by the pivoting transducer (Fig. 3.21 (a)).
2. Each echo profile is ordered according to the angular position (Fig. 3.21 (b)).
3. The original image is transformed to a polar form (Fig. 3.21 (c)).
4. Secondary beams are computed between two original neighbor beam (Fig. 3.21 (c)).
5. The image is smoothed by a 2 × 2 median filter.
6. The image is again transformed to cartesian form. As result of this transformation a significant number of pixels will be empty (Fig. 3.21 (d)).
7. The empty pixels are filled in a recursive way form, using for this an average of the eight nearest neighbors (Fig. 3.21 (d)).

8. An image reference reticle is added and a gaussian filter is applied.

Fig. 3.22 shows the scatterers distribution for a concentric arterial structure and an axial ultrasound beam position (a), and its corresponding echo profiles (b). Each axial echo is positioned by an angular position (c). In this way, the 2D echogram is constructed (d). The procedure of image smoothing is described in section 3.5.4.

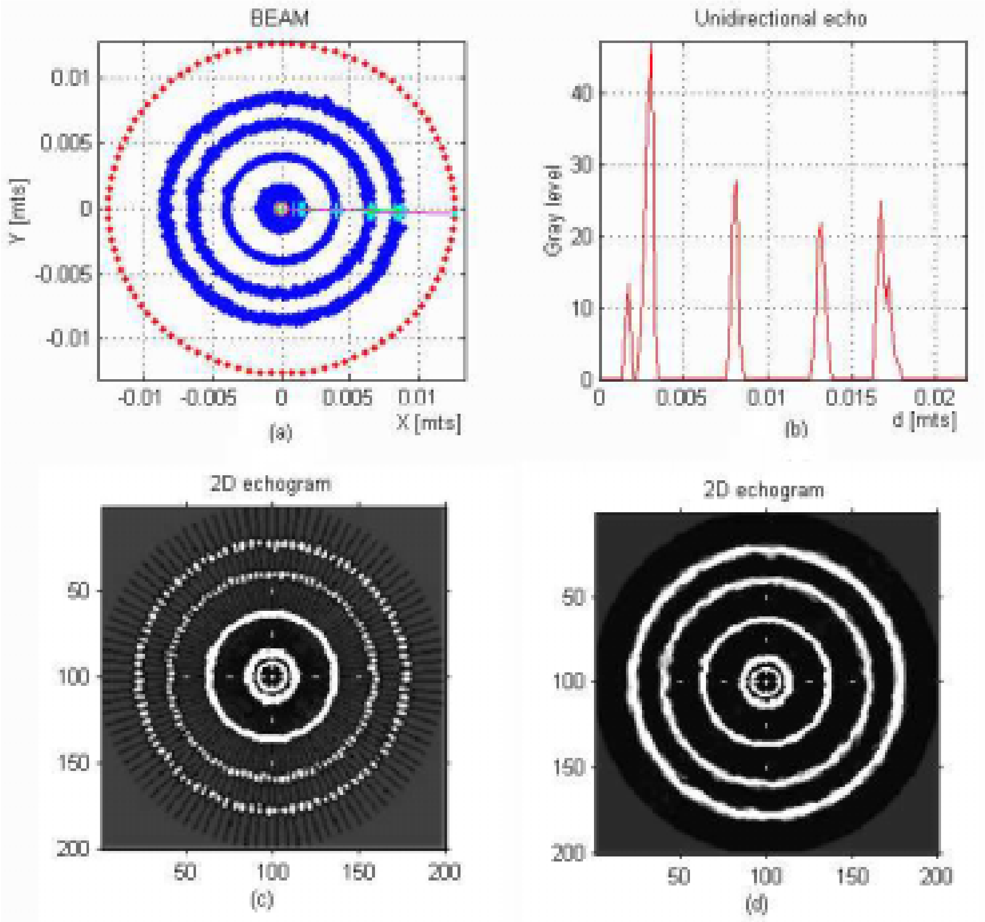

Figure 3.22: The scatterers distribution (a), the corresponding 1D echoes (b), 2D echogram is constructed (c) and the image is smoothed (d).

3.6 Validation of the Image Simulation Model.

Once defined the generic basic model of IVUS image formation, we need to compare it to real images contrasting the expert opinion to test its use. To this purpose, we defined procedures to extract quantitative parameters that permit to measure the global and local similarity of the images obtained. The main goal of this simulation is to give a general representation of the principal characteristics of the image. The comparison of real and simulated images should be done on the global image descriptors. We concentrated on the distribution of the grey levels. Data such as transducer dimensions (Fig. 3.12), the catheter as well as the reticle location, operation frequency, band width, original and secondary beam number used for the simulation are standard values used from Boston Sci. [31]. However, the optimal values of frequency and attenuation coefficient are obtained by the cross validation procedure [23]. The dimensions, scatterer number, and the backscattering cross section of the simulated arterial structures were obtained from different literature [46, 12, 13, 19, 22, 31]. Typical values of the RBC's "voxel" numbers took into account the typical hematocrit percentage [13] (section 3.4.4). Instrumental and video noise has been incorporated into the simulated image, due to electronics acquisition data, and the acquisition and processing to the video format.

The zones of greater medical interest (lumen, lumen/intima, intima/media and media/adventitia) were simulated for several real IVUS images. The smoothing image protocol is not known so that the corresponding tests were done until finding the maximal similarity to the real images based on the use of 3 progressive methods. 1) The empty pixels are filled using the average of eight neighbors. 2) A median filter is used, and 3) A gaussian filter is applied in order to find the noise reduction. The quantitative parameters used for the image comparison were directed for global and local image regions, being this:

1. ***Grey level average projection,*** p_x ***and*** p_y, horizontal and vertical image projection, are defined for an $m \times n$ image I as [24]:

$$p_{x(i)} = \frac{1}{m}\sum_{j=1}^{m} I_{ij} \ , \ p_{y(j)} = \frac{1}{n}\sum_{i=1}^{n} I_{ij} \tag{3.25}$$

2. We define a global linear ***correlation*** between real (x) vs simulated (y) data as follows:

$$y = mx + b \tag{3.26}$$

   where m and b are the linear correlation coefficients.

3. ***Contrast to Noise Ratio Signal*** (CNRS) as figure of merit, defined as [25]:

$$CNRS = \frac{(\mu_1 - \mu_2)^2}{\sqrt{\sigma_1^2 + \sigma_2^2}} \tag{3.27}$$

   where μ_1, μ_2, σ_1 and σ_2 are the mean and the standard deviation inside the regions of interest (ROIs).

3.6.1 Scatterer Radial Distribution.

The radial scatterer distribution is an important factor for a good image simulation. The scatterers under consideration in this simulation are: the transducer sheath, blood, intima, media and adventitia. We can obtain the arterial structure configuration from an emulated form and from a real validated IVUS image. For the study of the synthetic images we have used two procedures:

1. **Standard Data**. Typical geometric arterial parameters and its interfaces: lumen/intima, intima/media and media/adventitia are obtained from standard literature.
2. **Validated Data**. Geometrical parameters are obtained from a manually segmented IVUS images.

In order to investigate the image dependencies of IVUS parameters (frequency, attenuation coefficient, original beam number, secondary beam and smoothing procedures), we have used a standard data procedure, using for this modality a concentric scatterer distribution. To compare simulated images to real data, we use manually segmented real images, that correspond to the validated data procedure. In a manually delineated structures of IVUS images, we extract the position radius R_k of lumen, intima, media adventitia and transducer sheath. Figure 3.23 shows typical 2D spatial scatterer distributions obtained from standard procedure for the most important arterial structures and the scatterer artifact caused by the transducer sheath.

The radial scatterer distributions play a crucial role in the definition of the IVUS images because they define the ultrasound attenuation in the axial direction. Medical doctors have special interest in grey level transition in the interface of two media. For instance, the lumen/intima transition defines the frontiers of the lumen. These transitions can only be found through a good radial scatterer distribution.

The radial scatterers distribution of the typical arterial structures and the transducer sheath are shown in Fig. 3.24.

3.6.2 DBC Distribution

The k-layers DBC_k values for a typical simulated arterial structure are shown in Fig. 3.25 and Fig. 3.26. There the count of scatterers of each tissue is shown as a function of the cross section of scatterers. The numerical values are given in Table 3.3 [26].

3.6.3 IVUS Image Features.

Spatial Resolution.

A good spatial resolution gives the possibility of improving the visualization of the lumen/intima transition and studying the structures that means an important information for medical doctors. Typical numerical parameters such as: *Scatterer number* N_k, k-layer average radial position $\overline{R}_k$, its standard deviation η_k, the DBC k-layer mean μ_k, and its standard deviation σ_k are given in Table 3.3. The typical IVUS parameters used in this simulation are given in Table 4.1. The typical cell nuclear size was obtained by Perelman et al [22]. In Fig. 3.27 we can observe the dependency of

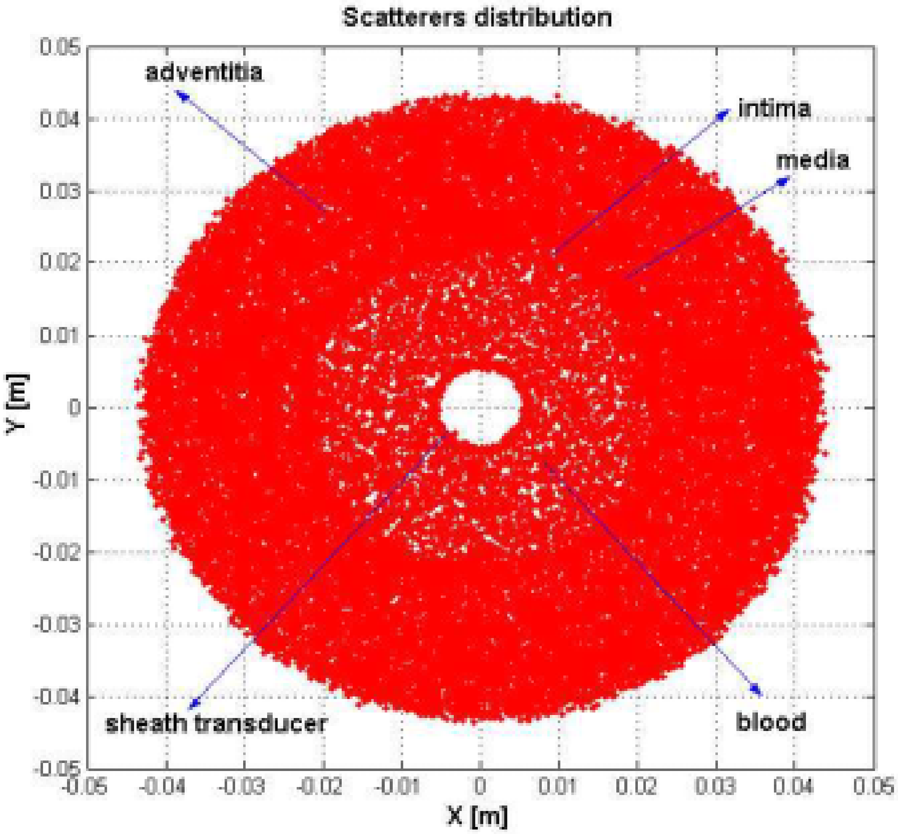

Figure 3.23: Typical concentric 2D scatterer distribution for the most important simulated arterial structures (blood, intima, media, and adventitia) and the scatterer artifact generated by the transducer sheath.

axial resolution and the ultrasound frequency. To illustrate this, four IVUS simulated images are shown. *Low frequency* ranging from 10 to 20 MHz correspond to an axial resolution from 154 to 77 μm, *intermediate frequency* from 20 to 30 MHz gives axial resolution from 77 to 51 μm. In these cases, it is possible to visualize accumulations around 100 RBC's *High frequency* from 30 to 50 MHz lead to 51 to 31 μm of axial resolution. Moreover, it is now possible to visualize accumulations of tens RBC's. The IVUS appearance improves when the frequency increases, allowing that different structures and tissue transition interfaces are better detected.

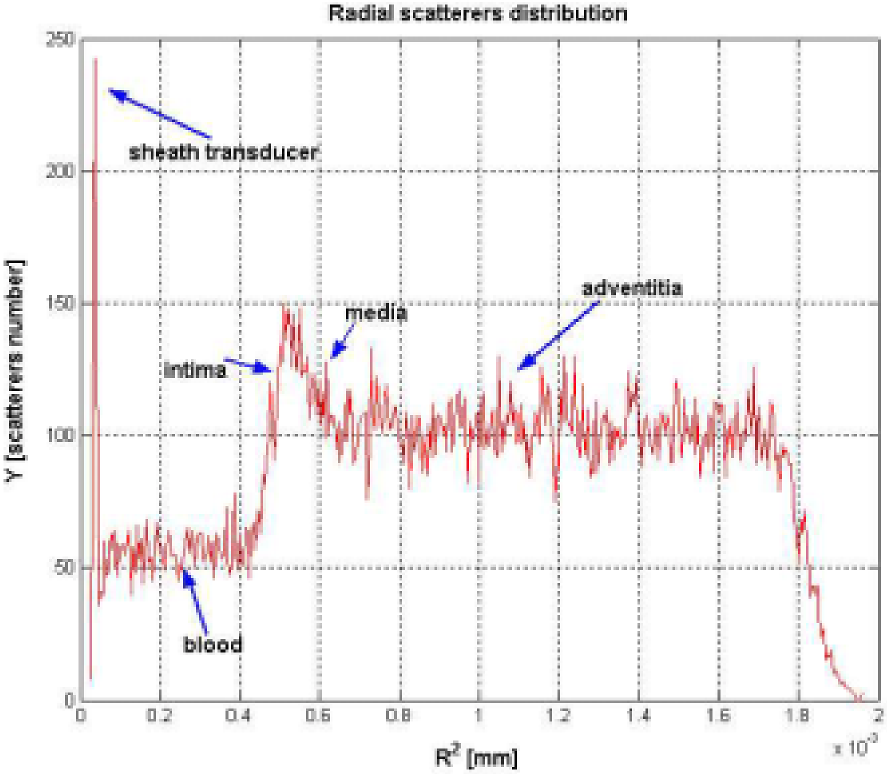

Figure 3.24: Radial scatterer distribution for the arterial structure: blood, intima, media, adventitia, and the transducer sheath.

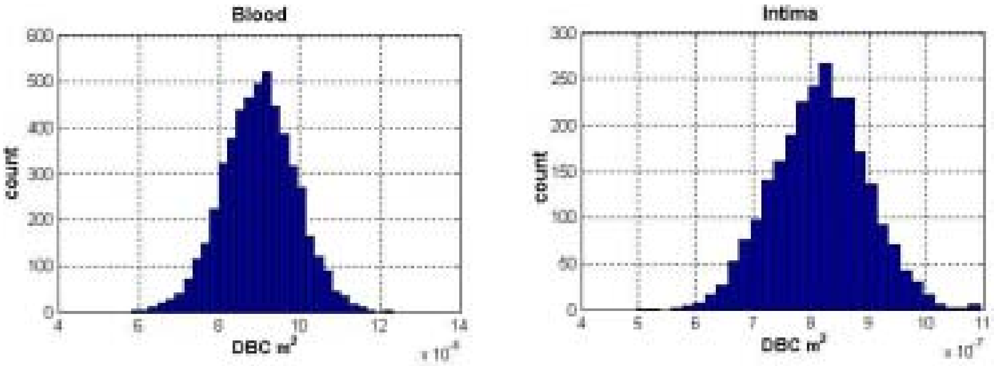

(a) (b)

Figure 3.25: DBC distributions of simulated arterial structures, blood (a) and intima (b).

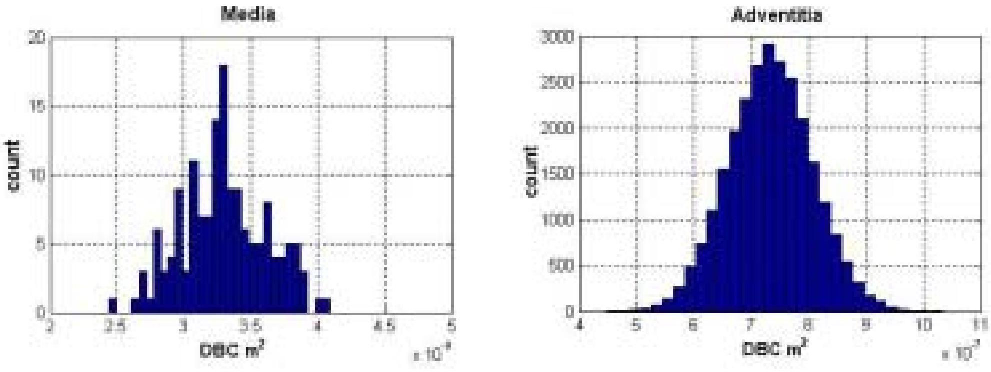

(a) (b)

Figure 3.26: DBC distributions of simulated arterial structures, media (a) and adventitia (b)

k	**structure**	N_k	$\overline{R}_k$ $[mm]$	η_k $[mm]$	$(DBC)\mu_k$ $[m^2]$ $\times e-6$	σ_k $[m^2]$ $\times e-6$
0	Transducer	475	0.59	0.05	7.2e-1	2.68e-2
1	Blood	6204	1.57	1.22	9.0e-2	9.48e-1
2	Intima	729	2.18	0.25	8.2e-1	2.86e-2
3	Media	150	2.38	0.35	3.3e-3	1.82e-1
4	Adventitia	25794	3.44	3.02	7.3e-1	2.71e-2

Table 3.3: An example of simulated values of arterial structures: N_k is the scatterer number, $\overline{R}_k$ is the mean radial position, η_k is the radial deviation, μ_k is the backscattering cross section and σ_k is the DBC deviation.

Optimal Ultrasound Frequency.

In order to validate our model, we compare synthetic to real images. We generated synthetic images for a great rank of frequency and used cross validation method [23] to find out the most similar image to the real one generated by Boston Sci. equipment at 40 MHz of frequency. The sum square error (SSE) from the real to the simulated images for each ultrasound simulated frequency is computed. Fig. 3.28 (a) shows the SSE versus ultrasound frequency. The optimal frequency is located in the interval of 40 to 50 MHz. Note that the central frequency of Boston Sci. equipment is 40 MHz, therefore it can be considered as an evidence to show the correctness of the method.

Optimal Attenuation Coefficient.

We have emulated synthetic IVUS images with different attenuation coefficients, the optimal attenuation coefficient was tested by applying the cross validation method of

parameter	**magnitude**
Ultrasound sound speed	1540 m/s
Maximal penetration depth	$2e-2$ m
Transducer angular velocity	1800 rpm
Transducer emission radius	$3e-4$ m
Attenuation coefficient Γ	0.8 dB/[MHz cm]
Ultrasound frequency	10 to 50 [MHz]
Beam scan number	160 to 400
Video noise	8 [grey level]
Instrumental noise	12.8 [grey level]
beta parameter	β=38.5 [ad]

Table 3.4: Typical IVUS simulation magnitudes

the synthetic images vs the real images. Fig. 3.28 (b) shows SSE vs attenuation coefficient Γ, the optimal attenuation coefficient obtained was 0.8 $dB/[MHz\ cm]$. There is a range of suboptimal attenuation coefficient values for a fixed ultrasound frequency; it is due to the great axial variability of scatterers. However, the attenuation coefficient can be taken as constant for each simulated region [32], although in the transition zones (lumen/intima, intima/media and media/adventitia) the attenuation gives great variability. For this reason, we must average the attenuation coefficient value. It is very important to find out that the optimal frequency is approximating the standard central ultrasound frequency 40 MHz and that the attenuation coefficient is near to the standard values of biological tissues being this from 0.5 to 1 $[dB/MHz\ cm]$. This result can be used in different ways: First, to check the used simulation parameters in the case of ultrasound frequency, and second to find structures of interest when the attenuation coefficient is known.

The Beam Number Influence.

Fig. 3.29 shows the appearance of several simulated IVUS images when the original and intermediate beam numbers are changed. Using the cross validation method we obtained the best IVUS appearance when the original beam number was 252 (Fig. 3.28 (c)). We can see that the IVUS appearance in the tangential direction is affected significantly by the beam number change. The total beams for the standard IVUS equipment is 256 [31, 60].

Initial Beam Intensity I_0 Influence.

Certainly, the synthetic image brightness is an open problem of the image formation model. A simplest approach is to variate it by modifying the original intensity, I_0 of the ultrasound beam, similar to the offset of the image acquisition system. Fig.

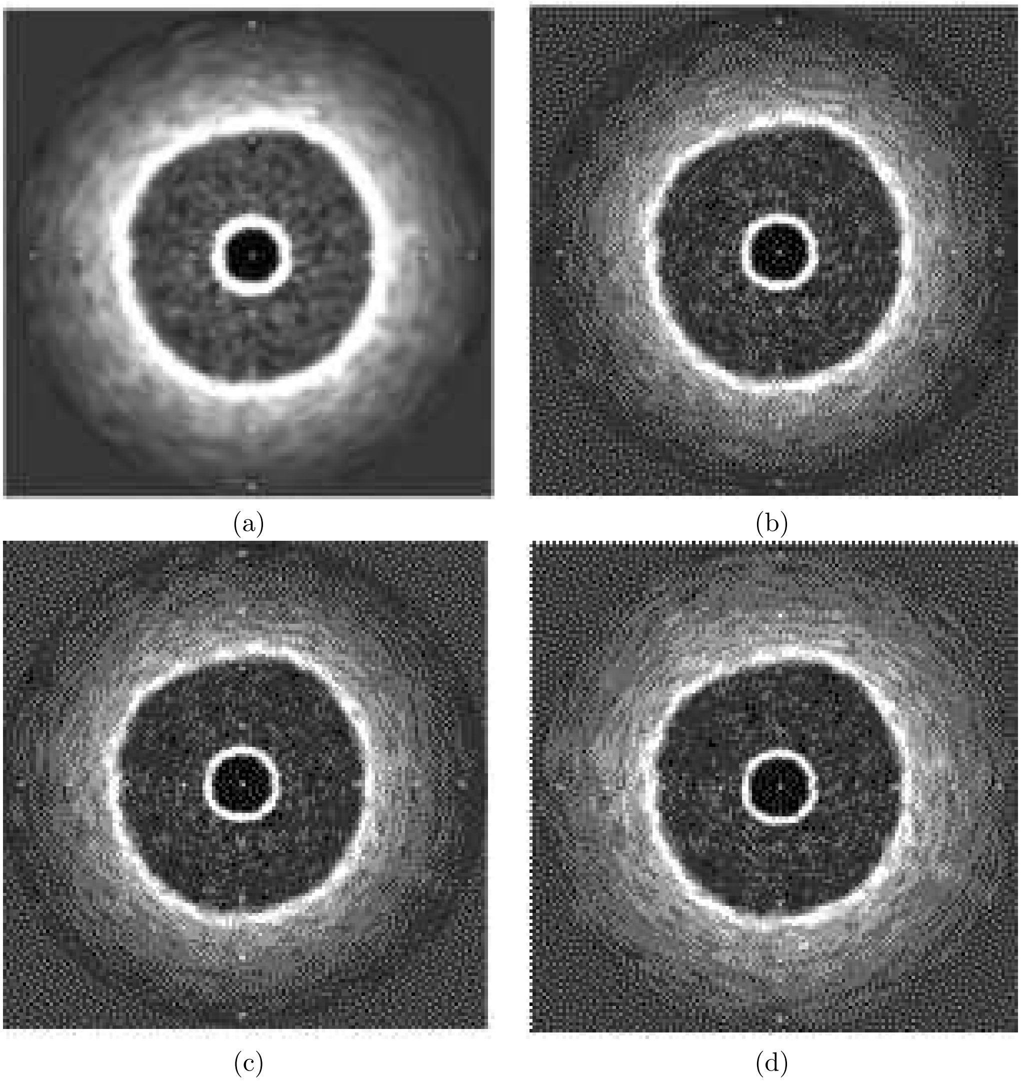

(a) (b)

(c) (d)

Figure 3.27: Synthetic images generated by low frequency: 10 MHz (a) and 20 MHz (b), intermediate frequency of 30 MHz (c) and high frequency of 50 MHz (d).

3.30 (left) shows a progressive reduction of the beam intensity I_0. Fig. 3.30 (right) show a standard Canny edge detector for each progressive reduction of the beam intensity as expected. We can observe that a small reduction of the initial intensity of the ultrasound beam, makes that the lumen/vessel transition zone, can not be detectable.

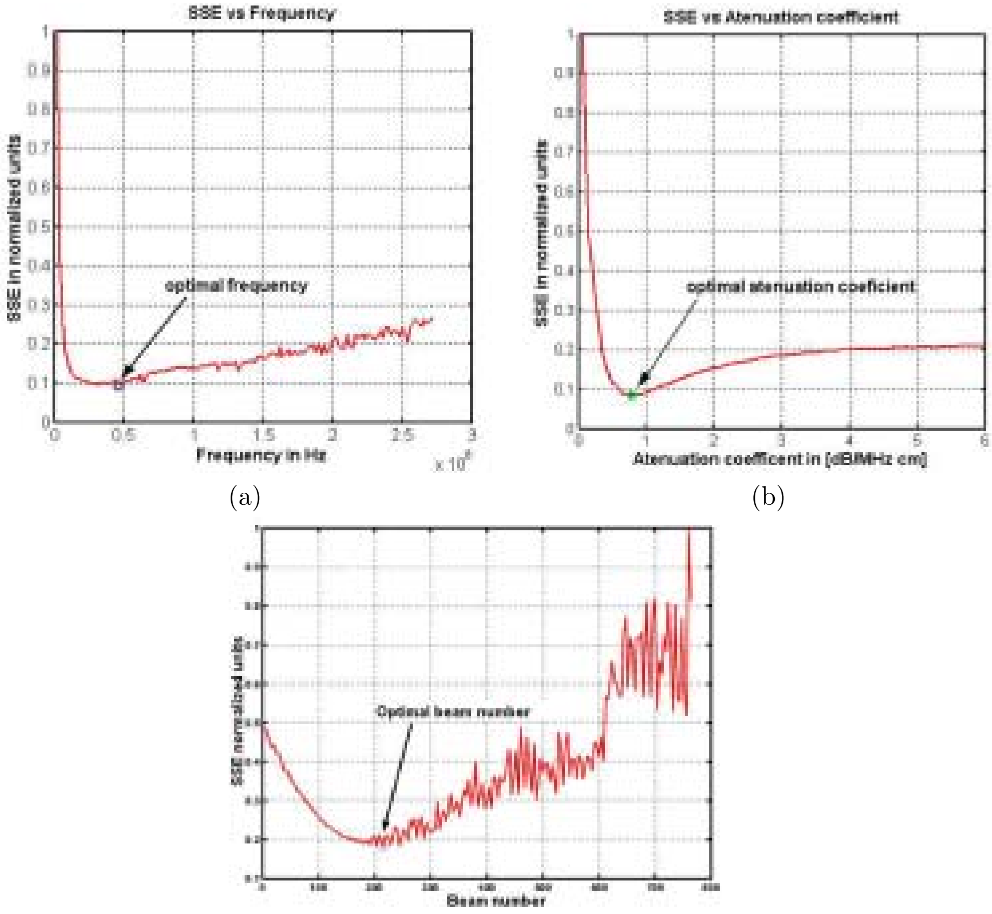

(a) (b)

(c)

Figure 3.28: The optimal ultrasound simulation frequency $f_0 \approx 46MHz$ (a), the optimal attenuation coefficient $\Gamma \approx 0.8dB/(MHz\ cm)$ (b) and the optimal beam number $NH = 252$ (c) are obtained by the cross validation method.

3.6.4 Real Versus Simulated IVUS.

In order to compare the real and simulated IVUS images, we have generated 20 synthetic images with morphological structures corresponding to the structures of a set of real images. We have used a real IVUS image with manually delimited lumen, intima, and adventitia to obtain the average radius location, $\overline{R}_k$ for each arterial structure. We applied the optimal frequency of 46 MHz and attenuation coefficient 0.8 [dB/MHZ cm]. Figure 3.31 (a) shows an IVUS real image of right coronary artery, obtained by a 40 MHz Boston Sci. equipment. Fig. 3.31 (b) shows a simulated image obtained at the optimal ultrasound simulation frequency 46 MHz. In the real image,

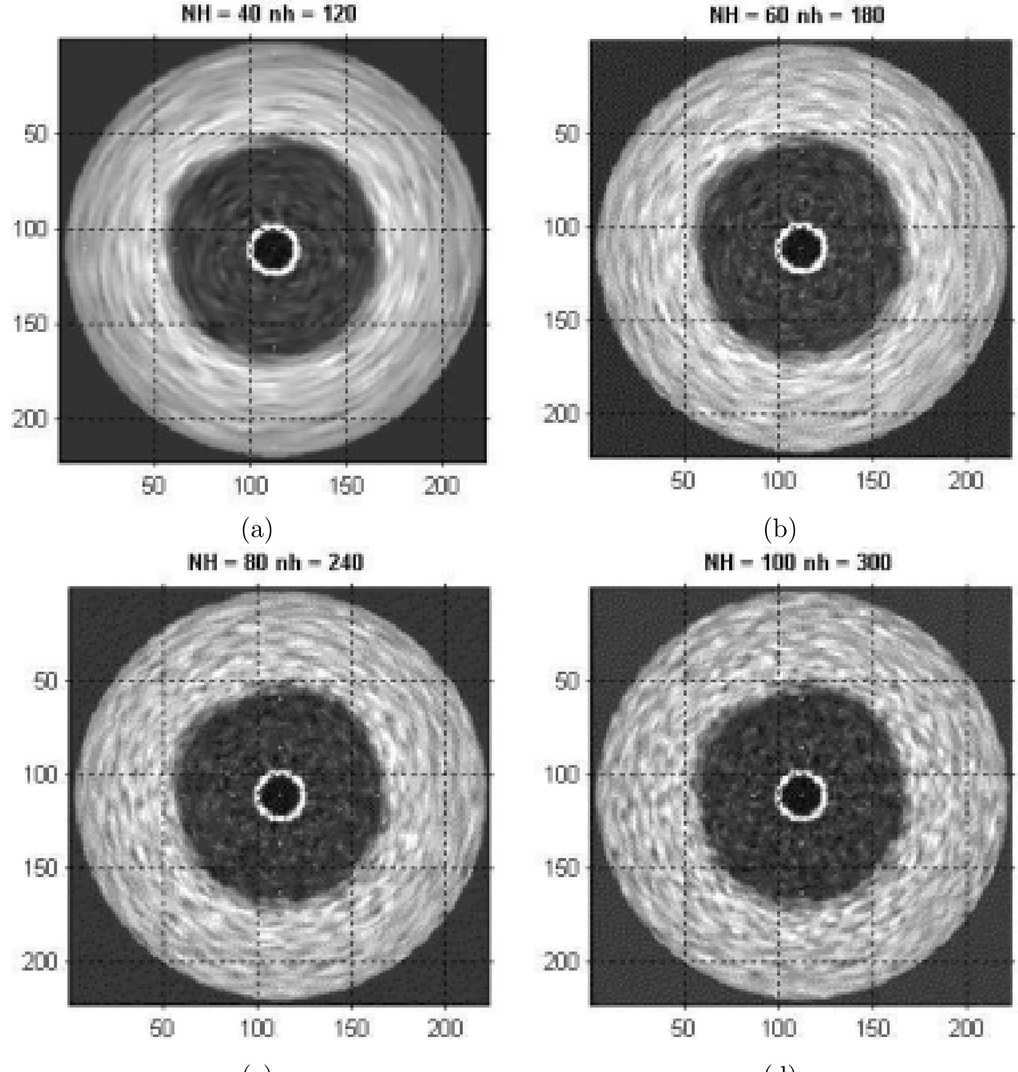

(a) (b)

(c) (d)

Figure 3.29: Different combinations of original (NH) and intermediate (nh) beams yield different IVUS appearance.

we can observe a guide zone artifact (12 to 1 o'clock) due to the guide presence; this artifact will not be simulated at this study. The horizontal ECG base line appears as an image artifact on the bottom of the real image. The global appearance of each image region (lumen, intima, media and adventitia) and their corresponding interface transitions (lumen/intima, intima/media and media/adventitia) are visually well contrasted, compared to the real image. A good quantitative global measure for comparison is the average grey level projection that allows a simple form to find

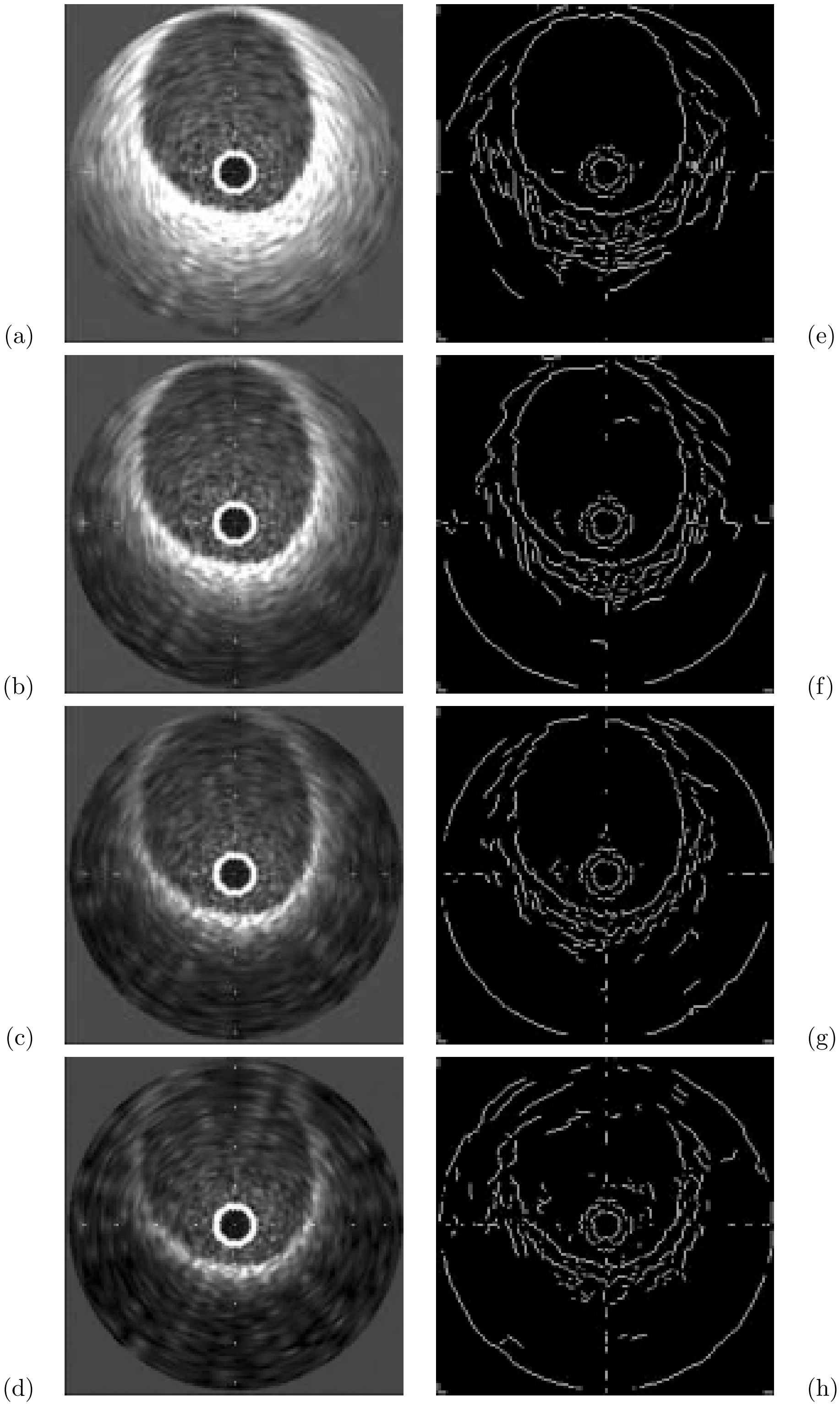

Figure 3.30: IVUS images at 30 MHz varying the beam initial intensity I_0 from $(1, 1/2, 1/4, 1/8)$ (a,b,c,d) respectively and their corresponding Canny (e, f, g, h)

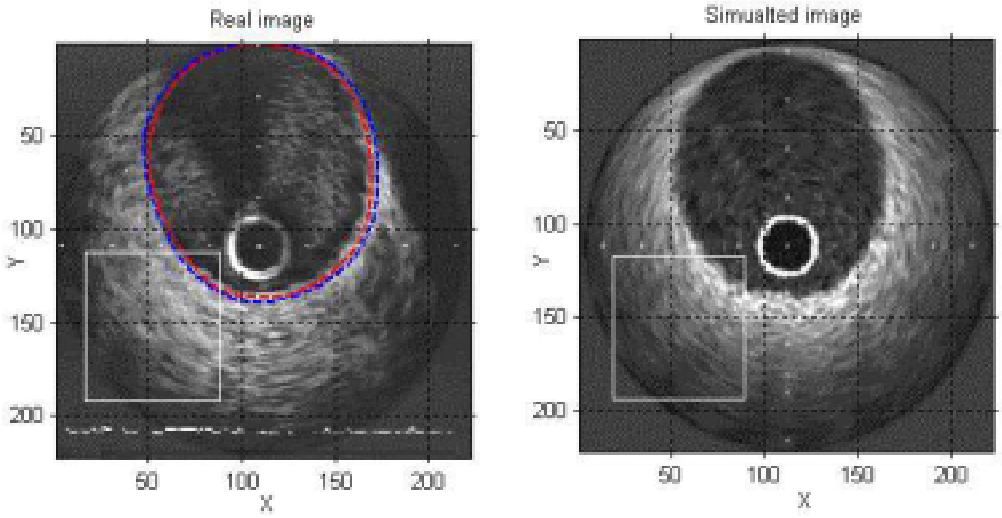

(a) (b)

Figure 3.31: Real (a) and simulated (b) IVUS images segmentation. ROI's are given as squares. Manual segmentation of the vessel is given in (a).

the main image correlated characteristics in an 1D shape grey level profile. Grey level base line, video noise, instrumental noise, reticle influence and the main grey level distribution incoming from the main arterial structures are roughly visible from the grey level average projection. The average grey level projection gives a global measure of similarity between real and simulated images. The similarity measured can be computed for example by the local attenuation coefficient of the projection profile of each ROI [32]. Fig. 3.32 gives the projections in the horizontal and vertical direction for the real (Fig. 3.31(a)) and simulated (Fig. 3.31(b)) IVUS images. The correlation coefficients, m and b (Fig. 3.33) for the grey level average projection in the horizontal ($m = 0.63, b = 13.53$) and vertical ($m = 0.75, b = 9.07$) directions, show a positive correlation between the real and simulated data. Fig. 3.34 shows two selected regions of interest, of the real (Fig. 3.31 (a)) and simulated (Fig. 3.31 (b)) image. We can see a good grey level distribution and a soft grey level decay from the center to the peripheries of the IVUS image, produced by the inverse relation between the ultrasound intensity and the penetration depth. The other reason is that the normal attenuation is caused by the scattering intensity given by the tissue impedance. The Fig. 3.35 show grey level average profiles in vertical direction Fig. 3.35 (a) and (c) and horizontal direction Fig. 3.35 (b) and (d) of the selected ROI's from Fig. 3.31 (a) and (b). The linear correlation coefficients, m and b (Fig. 3.36) for the grey level average projection in the horizontal direction ($m = 0.87, b = 4.91$) and vertical direction ($m = 0.85, b = 5.79$), show a significant grey level correspondence between the real and simulated ROI's image.

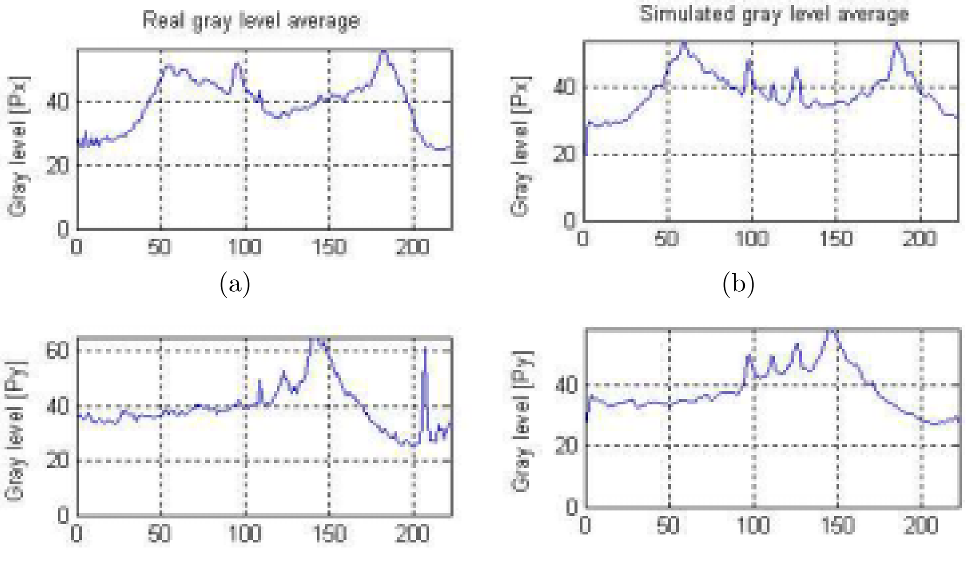

(a) (b)

(c) (d)

Figure 3.32: Horizontal (a) and (b) and vertical direction (c) and (d) grey level profile average projections, from real (Fig. 3.31 (a)) and simulated (Fig. 3.31 (b)) IVUS images.

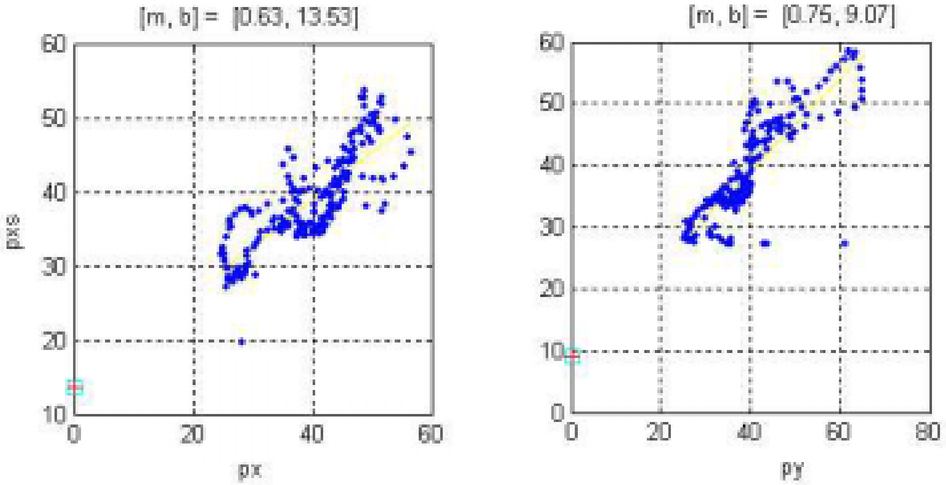

(a) (b)

Figure 3.33: We obtain the horizontal correlation using (a) vs (b) from Fig. 3.32 and the vertical global correlation using (c) vs (d) from the same figure.

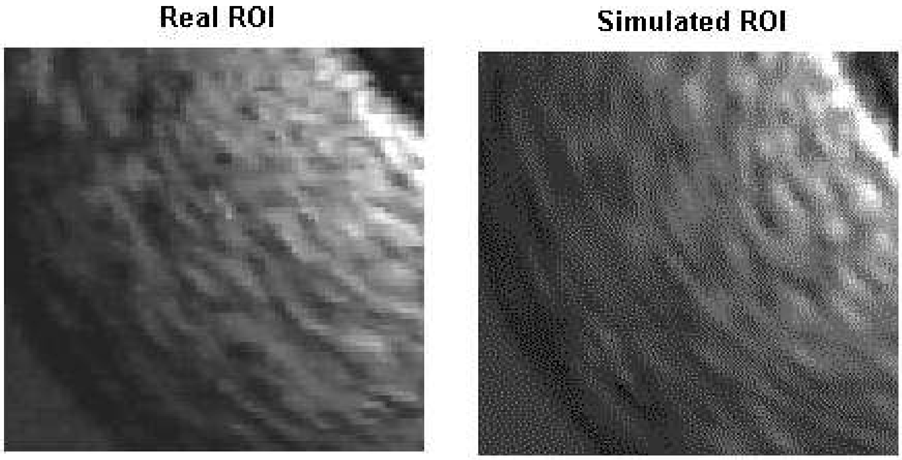

(a) (b)

Figure 3.34: Real (a) and simulated (b) IVUS image ROI's

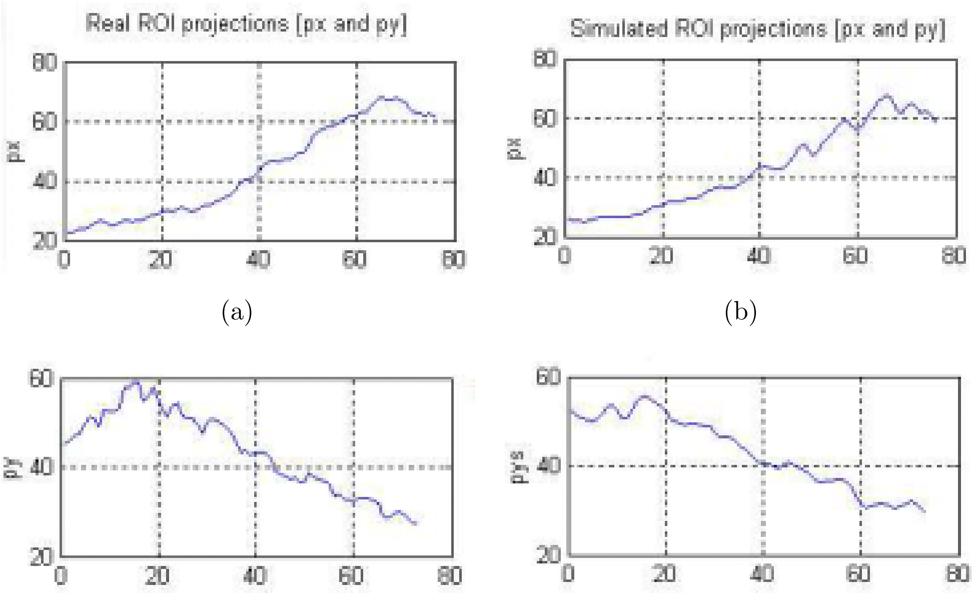

(a) (b)

(c) (d)

Figure 3.35: Horizontal (a) and (b) and vertical (c) and (d) projections of (Fig. 3.34(a)) and simulated (Fig. 3.34(b)) ROIs IVUS images.

3.6.5 Polar Images.

A polar representation of IVUS images offer several advantages: 1) The ROI's to study are very easy to be selected. 2) We can compare the artifact generated by

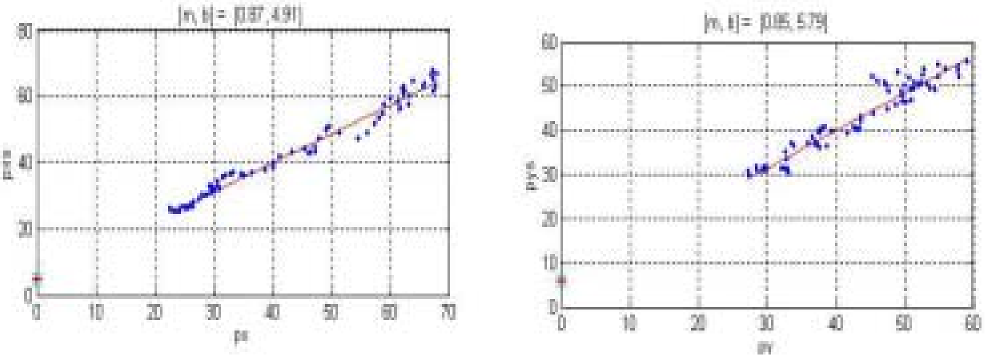

(a) (b)

Figure 3.36: Grey level average correlation, horizontal projection simulated (pxs) vs real(px), obtained from Fig. 3.35 (a) vs (b) and vertical simulated (pys) vs real (py) data, from Fig. 3.35 (c) vs (d).

the smoothing procedures. 3) Radial and angular comparison are totally separated, therefore the transition zones in each directions are very easy to be observed. Fig. 3.37 shows a real (a) and simulated (c) cartesian IVUS images and the corresponding real (b) and simulated (d) polar transformations. A ROI was selected from the real and simulated polar images and the correlation coefficients were obtained. Figure 3.38 (a) shows the grey level average vertical projection for the real and simulated ROI's data (delineated in red in Fig. 3.37). We can see that the grey level profile of the transition of arterial structure in the lumen/intima, intima/media and media/adventitia are very well simulated, being the linear correlation coefficients $m = 0.93$ and $b = 1.61$ (Fig. 3.38 (b)). The ***global horizontal profile*** of the polar images along the projection θ (Fig. 3.39 (a) and (b)) gives a very important and comparative information about the real and simulated grey level average of arterial structures. The information that can be extracted is relative to the global grey level distribution. The histogram (Fig. 3.39 (b)) of grey level differences between the horizontal profile of real and simulated data, indicates a very good correspondence (mean $\mu = 8.5$ and deviation $\sigma = 10.2$). Fig. 3.40 (a) shows the global projection in the radial direction (the vertical profile). We can see a very good correspondence between the grey level shape profiles (mean $\mu = 5.7$ and deviation $\sigma = 8.5$). The histogram (Fig. 3.40 (b)) of grey level difference confirms the good correlation between the real and simulated IVUS data.

The maximal difference profiles are localized in the transducer sheath grey level distribution, and the base line of the transducer sheath inner region. These differences can be smaller increasing the video and instrumental noise. The high frequency oscillations in the grey level profiles come from the concentric arterial structures. We can also observe the gradual reduction of the grey level magnitude from intima/media interface to adventitia, caused by the ultrasound intensity attenuation.
Next step of the validation of the model is to show the significant correspondence between real and simulated grey level distribution data in the medical zones of inter-

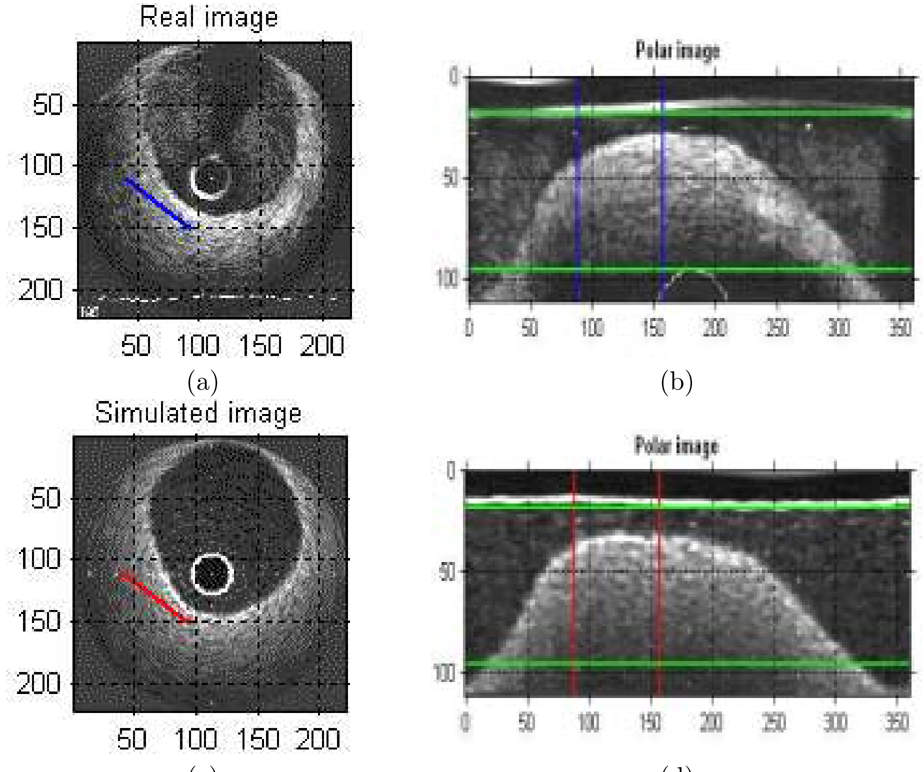

(a) (b)

(c) (d)

Figure 3.37: Real (a) and simulated (c) cartesian images and their corresponding real (b) and simulated (d) polar transformation.

est. To this purpose, 20 validated real IVUS images and their corresponding ROI's were selected. The spatial boundaries of the morphological structures of the real data are kept in the synthetic data. Fig. 3.41 (a) shows 10 real and their corresponding simulated (b) synthetic images. The polar images are shown in figure 3.42.

Figure 3.43 shows the simulated vs real grey level correlation for the polar ROI's images selected as shown in Fig. 3.37. The linear correlation coefficients show a good grey levels correspondence, being these m=0.90 and b=1.42. The best correspondence is located by low grey levels (20 to 40 grey levels), lumen scatterers, lumen/intima transition, and adventitia. The transition of intima/media and media/adventitia (45 to 60 grey levels) indicate a gradual dispersion. The CNRS average presents a significative uniformity values, $\mu = 6.89$ and $\sigma = 2.88$, for all validated frames. The contrast to noise ratio CNRS as figure of merit for each arterial validated region is shown in Fig 3.44. The CNRS region mean, standard deviation, and the SSE values referring to the 20 image frames are summarized in table 3.5. The lumen is a good simulated region, mean, $\mu = 0.46$ and deviation $\sigma = 0.42$. The explanation is that the lumen is not a transition zone, the attenuation ultrasound intensity in this region

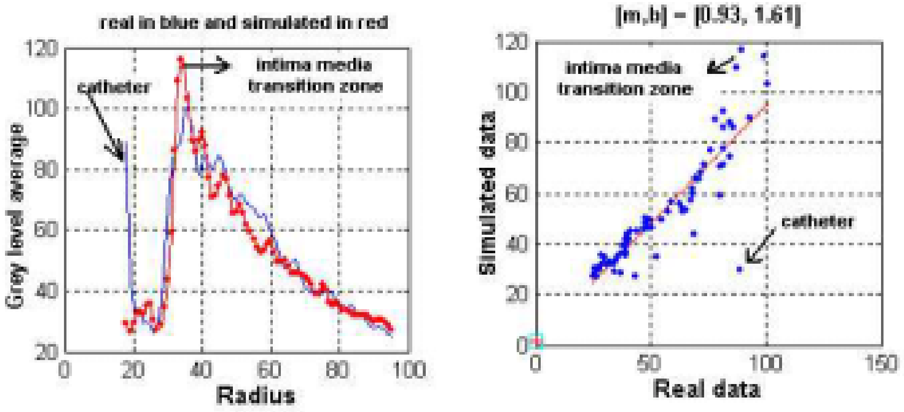

(a) (b)

Figure 3.38: Real(in blue) and simulated (in red) grey level vertical profile (a) of ROI's of Fig. 3.37 (b) and data correlation (b).

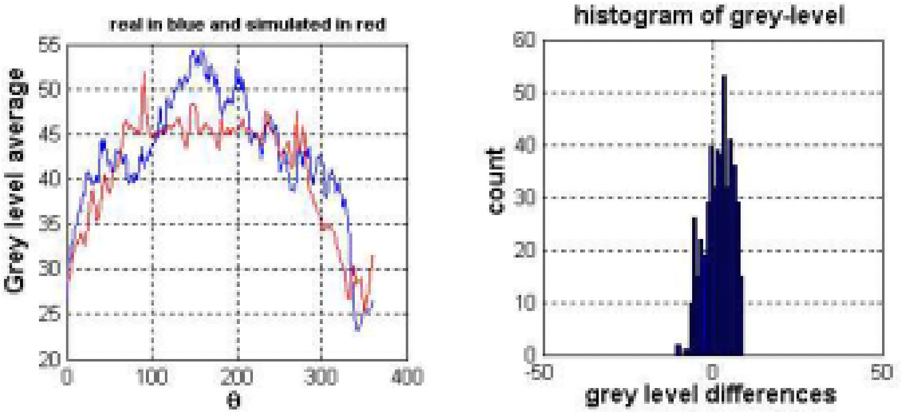

(a) (b)

Figure 3.39: Global projections in direction θ (a), from Fig. 3.37 (b) and (d), the corresponding histogram grey level differences (b).

ROI	***mean***	***std***	***SSE***
Lumen	0.46	0.42	47.68
Intima	10.0	4.38	12.63
Media	9.91	5.14	15.05
Adventitia	7.21	2.76	4.28

Table 3.5: CNRS mean, standard deviation (std) and sum square error for different tissues structures.

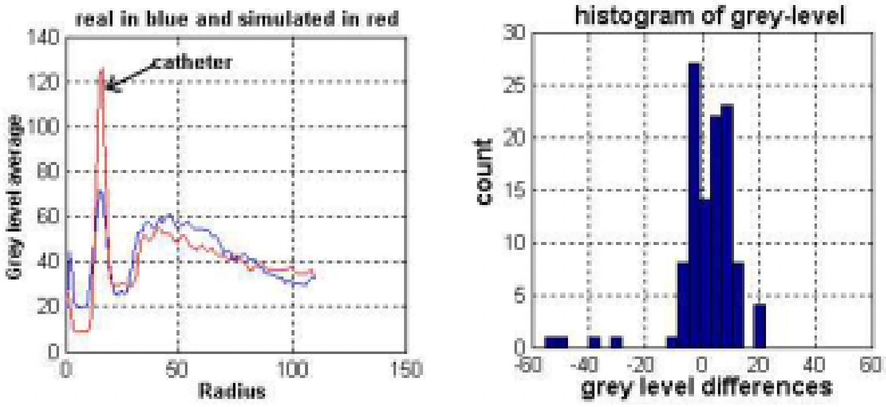

(a) (b)

Figure 3.40: Global projection in R direction (c), from Fig. 3.37 (b) and (d), the corresponding histogram grey level difference are shown in (b).

is very poor (1 to 2%), which determines a simple grey level profile.

The histogram grey level differences for each region of interest in the 20 validated frames are displayed in Fig. 3.45 and Fig. 3.46. Table 3.6 explains the distribution center, μ and the standard deviation, σ for the grey level difference distribution for each simulated region. The minus sign in the mean values means that the simulated images are brighter than the real images. A symmetric Gaussian can be seen in the lumen grey level differences distribution, with mean $\mu = -2.44$ and deviation $\sigma = 15.13$. The intima distribution has a mean of $\mu = -18.56$ and deviation of $\sigma = 24.01$, and the media region has a mean of $\mu = -17.82$, and a deviation of $\sigma = 22.62$. The grey level differences distribution displays a light asymmetry. As a result, the simulated image tends to be brighter than the real image. The adventitia grey level differences values show a symmetric distribution with a center of $\mu = -13.30$, and a deviation of $\sigma = 14.27$.

ROI	μ	σ
Blood	-2.44	15.13
Intima	-18.56	24.01
Media	-17.82	22.62
Adventitia	-13.30	14.27

Table 3.6: Mean and deviation of the ROI's grey level differences referred to histogram from Fig. 3.45 and Fig. 3.46.

It is very important to note that the grey level difference distribution exhibited Gaussian distributions for all regions of interest. Real and simulated grey level distributions for each region of interest are shown in Fig. 3.47 and Fig. 3.48. We can note the great similarity in the grey level distributions profile. Figure 3.49 shows the grey level histogram of the different tissues structures that appear in IVUS images. As

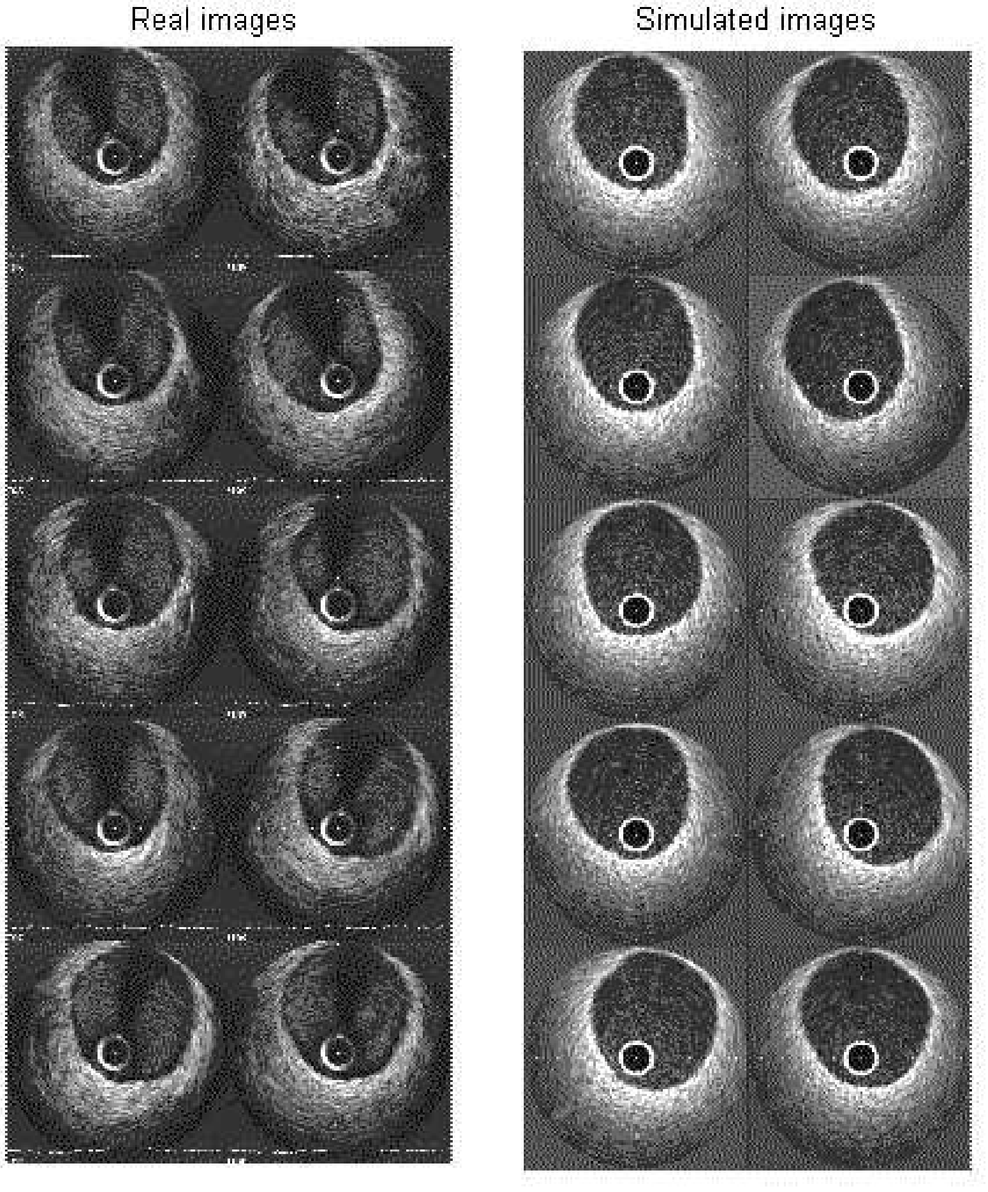

(a) (b)

Figure 3.41: 10 original IVUS images (a) and the corresponding simulated (b) images.

expected, it can be seen that the grey level the distributions of different structures overlap and as a result it is not possible to separate the main regions of interest in IVUS images, using only the grey level distributions as image descriptors.

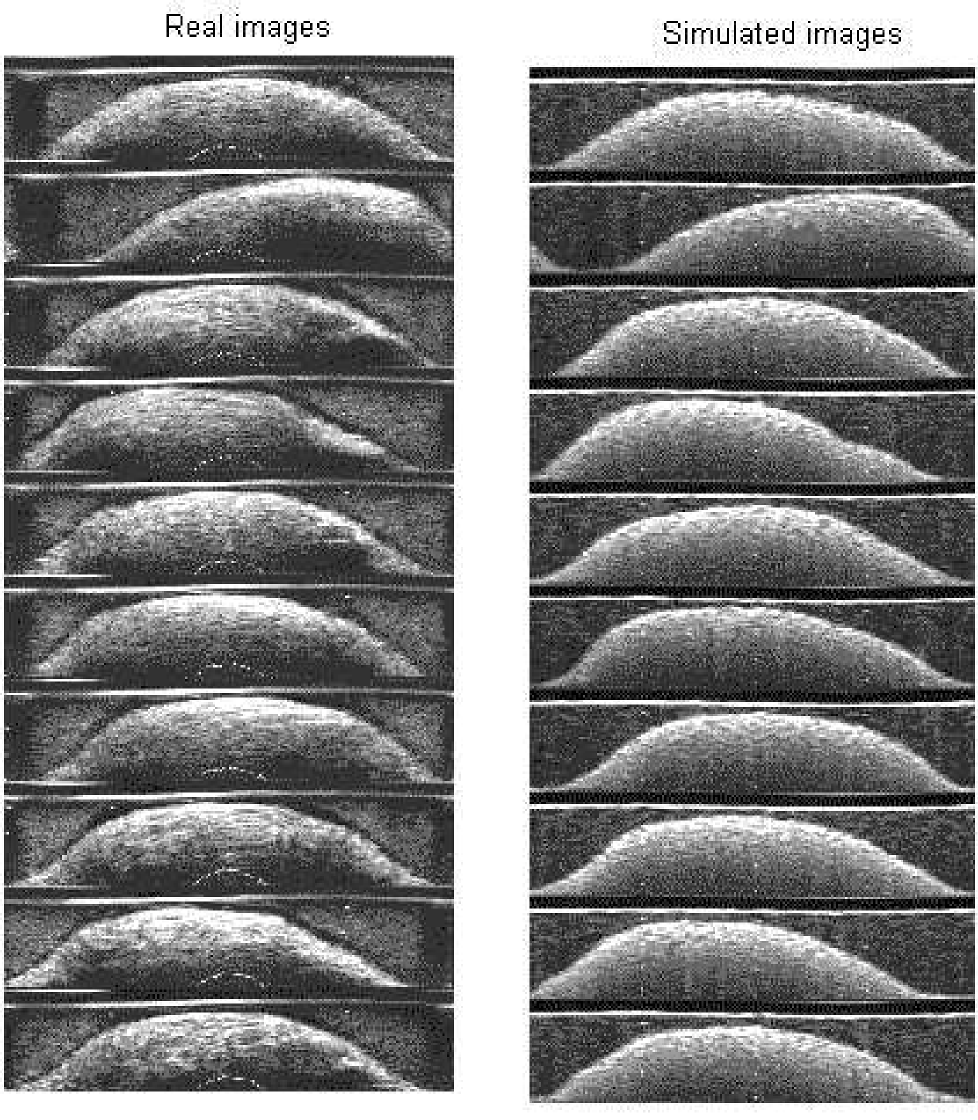

(a) (b)

Figure 3.42: 10 polar real images (a) and the corresponding simulated (b) images.

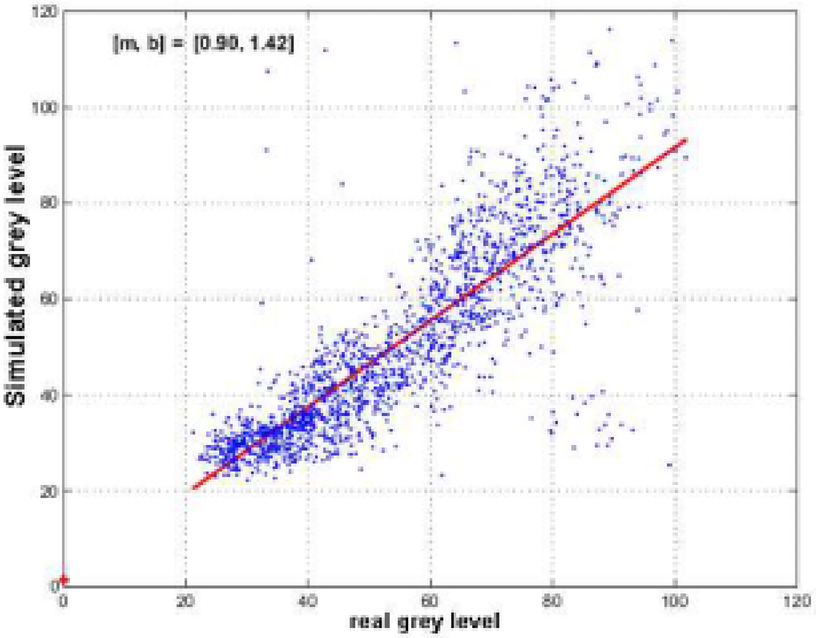

Figure 3.43: Simulated vs real grey level values for 20 ROI's comparing pixel grey level and the regression line.

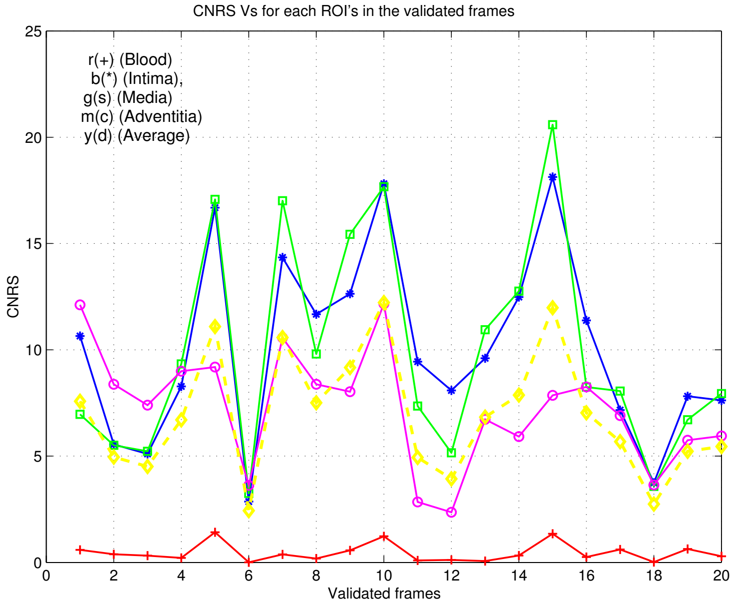

Figure 3.44: CNRS values for each ROI's of 20 manually segmented image frames.

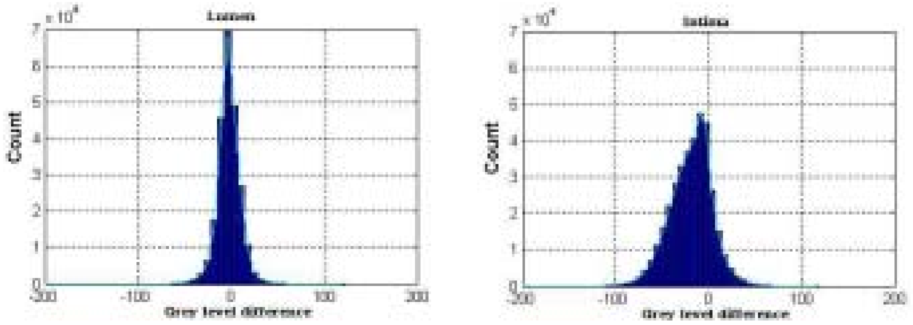

(a) (b)

Figure 3.45: Histogram of grey level differences for lumen (a) and intima (b).

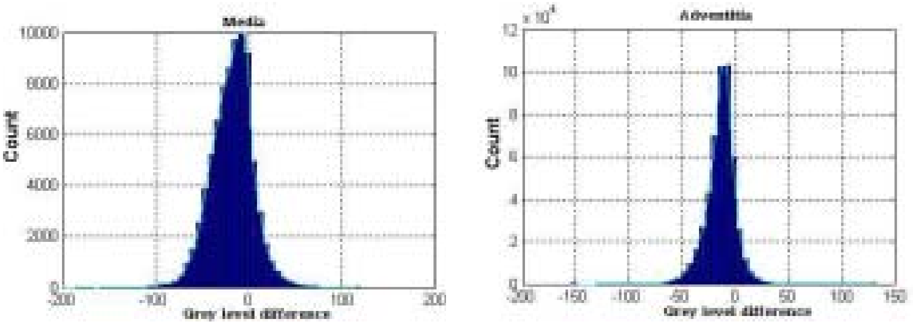

(a) (b)

Figure 3.46: Histogram of grey level differences for media (a) and adventitia (b).

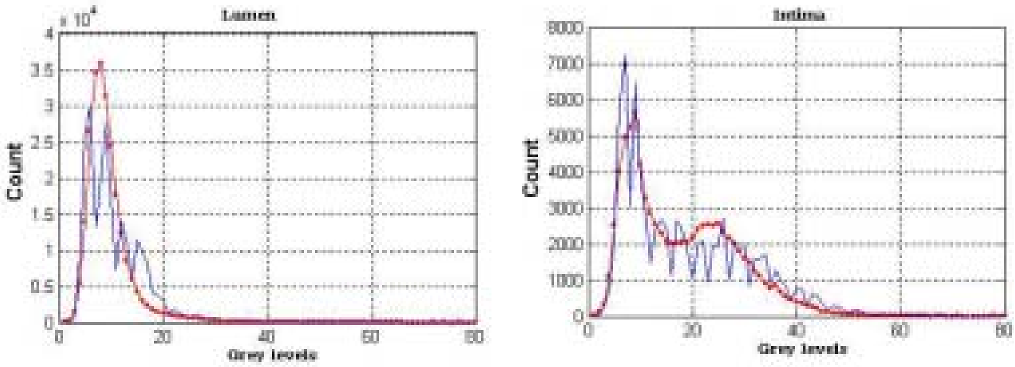

(a) (b)

Figure 3.47: Real (in blue) and simulated (in red) grey level distributions for lumen (a) and intima (b)

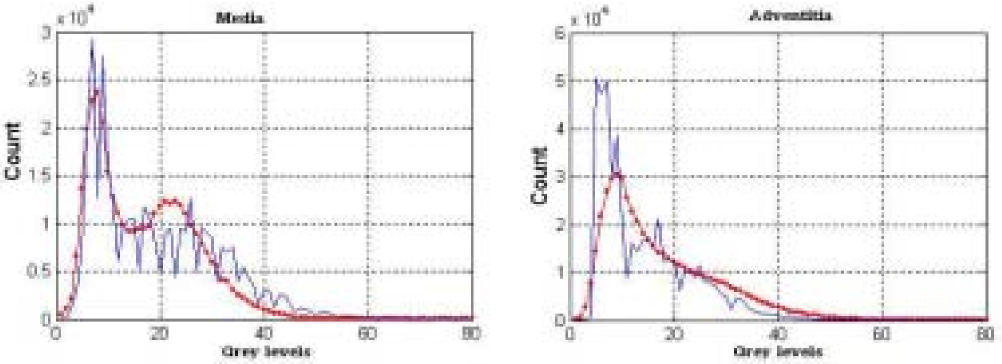

(a) (b)

Figure 3.48: Real (in blue) and simulated (in red) grey level distributions for media (a) and adventitia (b)

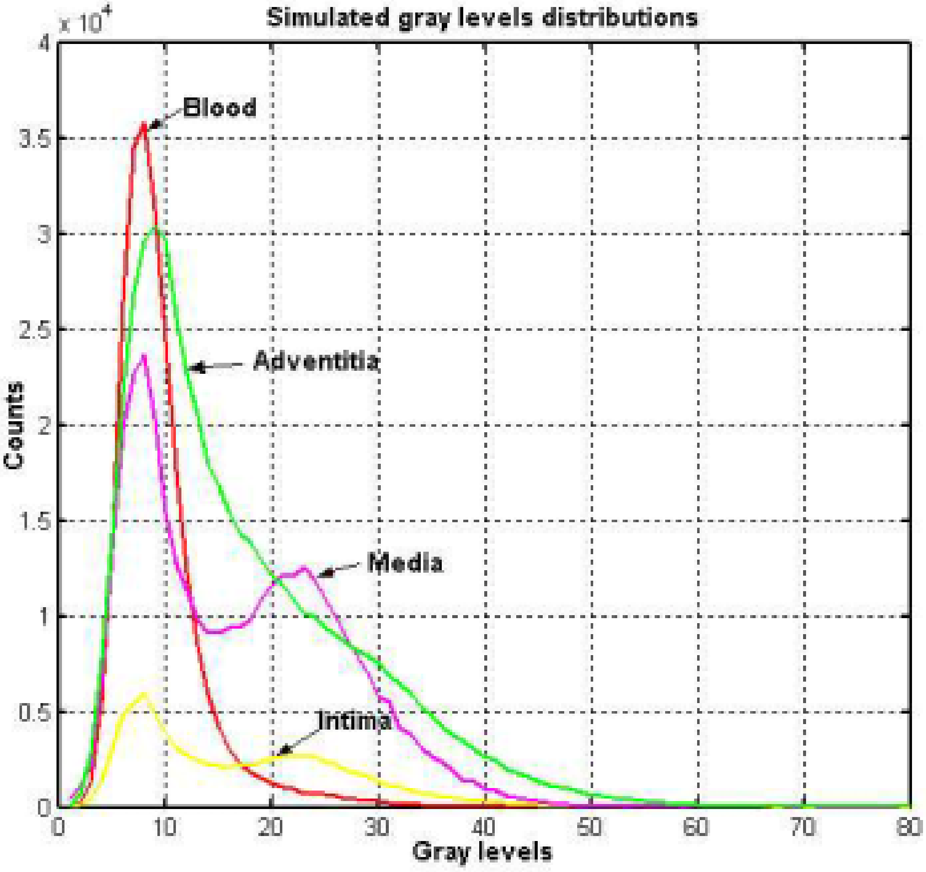

Figure 3.49: Simulated grey level distributions for blood, intima, media and adventitia.

Chapter 4

IVUS as a Geometric and Kinematic System.

The IVUS sequences images can be studied as a result of the assemblage and interaction of vessel properties that depend on vessel curvature and tortuosity, dynamical properties that depend on heart movement, blood pressure, catheters factors and image processing procedures (See Fig. 4.1). A general model that explain the explicit dependence between: geometric, dynamical and processing factors that allow to obtain the principal characteristics of an IVUS sequence, can be very complex to develop. A more simple way to explain the vessel wall shape dependence due to dynamical factors influence, is to assume that we can separate dynamical from geometrical contributions obtaining the Fourier decomposition on the geometric pa-

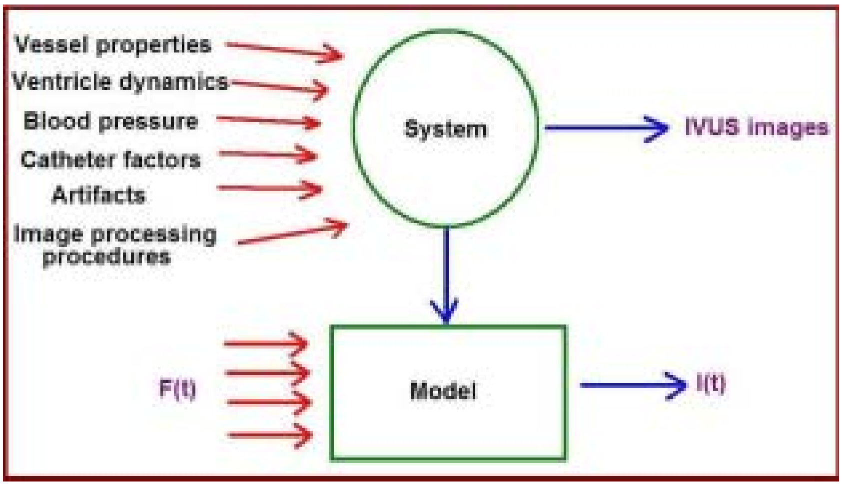

Figure 4.1: Generic model of IVUS data generation.

rameters implicated in an IVUS sequence. Next section we explain and modelled each one of this factors, in order to obtain an approximated model that explain the temporal evolution of the vessel wall.

4.1 General Assumptions and Methodology

The spatial time dependence of a coronary artery is mainly governed by the myocardium dynamic evolution, blood pressure and intrinsic geometric vessel properties [19, 48, 59, 71]. The first order approximation to vessel dynamics is given by a linear transformation combining translation, rotation and scaling [40]. In the particular case of an IVUS sequence some simplifications can be assumed. In order to determine the general assumptions that the formulation of IVUS motion admits, we have analyzed dynamics profiles extracted from real data. The training data used for determining the formulation of our model is an IVUS pullback of 2090 images corresponding to 45 mm long vessel segment from a pathological right coronary artery (See Fig. 4.2). The data were acquired using a Boston Sci. equipment at 40 MHz at constant pullback speed of 0.5 mm/sec. We will study separately rigid (translation and rotation) and non rigid (scaling) dynamics. Usually it is considered that a dynamic parameter can be neglected when the measurements have a standard deviation $< 20\%$ [41].

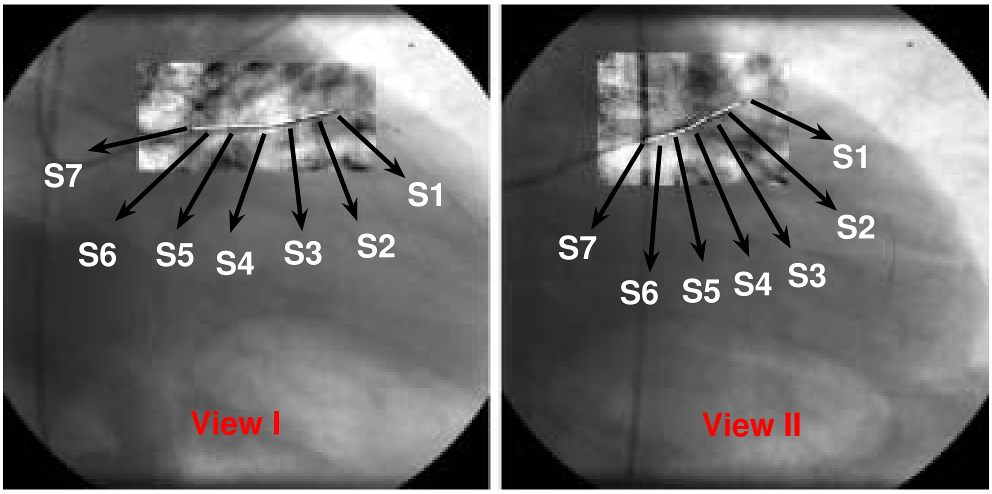

Figure 4.2: Right coronary artery angiography views.

4.1.1 Isotropic Radial Deformation.

Assuming laminar axisymmetric flow within the vessel and neglecting the nonlinear terms in the Navier-Stokes equations [19] the pulsatile radial pressure $P(s,t)$, on

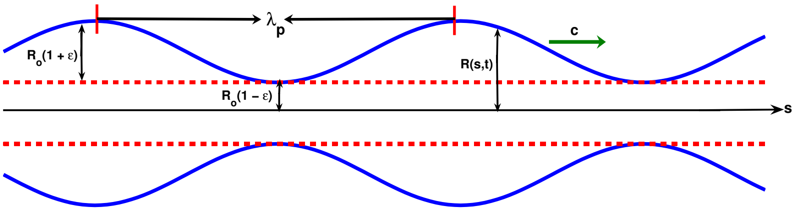

Figure 4.3: $R(s,t)$ vessel wall radius deformation

vessel wall can be written as:

$$P(s,t) = \sum_{-\infty}^{\infty} p_n(s,t) \times exp(\frac{i2\pi nt}{T}) \tag{4.1}$$

$$p_n(s,t) = \int_0^T P(s,t) \times exp(\frac{i2\pi nt}{T})dt \tag{4.2}$$

The spatial and temporal dependence of the radial deformation $R(s,t)$ of an elastic tube, may be described by:

$$R(s,t) = R_0(1 + \epsilon P(s,t))$$

Using (Eq. 4.1) $R(s,t)$ can be rewritten as:

$$R(s,t) = R_0(1 + \epsilon sin(2\pi/\lambda_p(s - ct))) \tag{4.3}$$

where ϵ is the amplitude ratio that gives the vessel wall elastic modulus, $\lambda_p = 2\pi/T$, is the wave length of the blood pulse, and T, is the period of one cardiac cycle, c its wave speed and R_0 is the undeformed radius at blood pressure equal to zero. Figure 4.3 gives the geometric parameters of the vessel wall profile radial deformation. We can see from (Eq. 4.3) that the radial deformation of cardiac arteries is mainly due to blood pressure and vessel wall elastic properties. By Hooke's law, the radial increment, ∇r, is proportional to the gradient of blood pressure, ∇P via the relation [19, 59, 57, 58]:

$$\nabla r = (\epsilon \Delta p/\pi)^{1/2}$$

Assuming standard values [53] of $\epsilon = (0.010 \pm 0.020)\ mm^2/mmHg$, $\Delta p \approx 40\ mmHg$ yield that $\nabla r \approx 0.35\ mm$. Taking into account that the radii of coronary segments [56] is in the range $r = 2.64 \pm 0.3\ mm$, we have that the relative radial deformation induced by blood pressure scaling is $\delta r = (\nabla r/r) \times 100 \approx 13\%$. Because under 20% of max inter-observer variation [41], radial scaling will be dropped from our model.

4.1.2 Vessel Wall Translation and Rotation.

Vessel displacement along the sequence is reflected by the vessel wall profile in longitudinal cuts. Two orthogonal cuts $C1$ and $C2$ (Fig. 4.4 (a) and (b)) respectively were

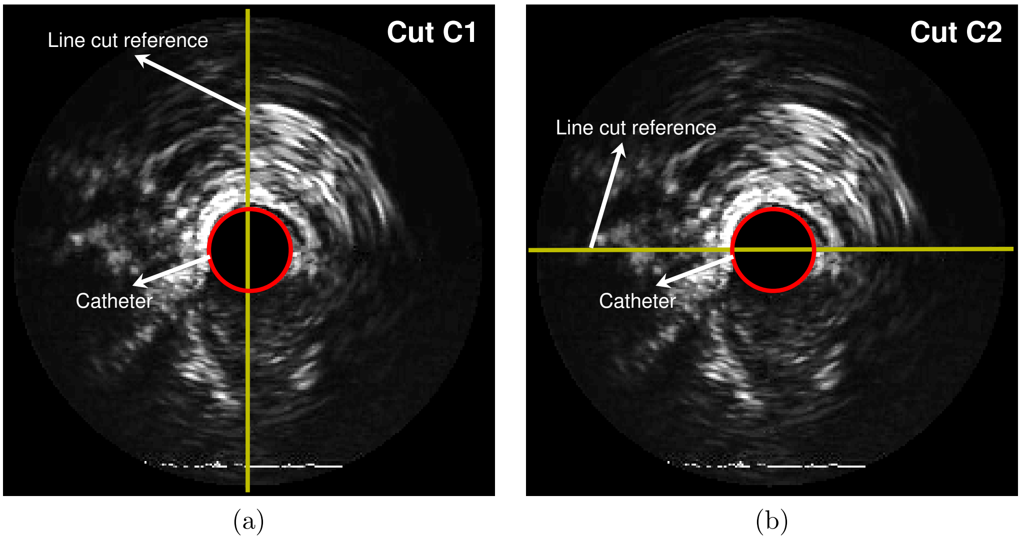

Figure 4.4: Two orthogonal IVUS cuts $C1$ (a) and $C2$ (b)

obtained in order to study vessel wall evolution in temporal direction. Figures 4.5 and 4.6 show that there are two mains contributions to the shape profile of the vessel wall kinematics behavior. A pulsatile wavy profile (blue and red sinusoidal lines) due to heart dynamics contribution and a systematic contribution (green base-line) due to the vessel geometry. In order to obtain computationally treatable data and to analyze vessel displacement, the segmented sequence has been divided into seven subsequences (S1 to S7)(see Figs. 4.2 and 4.5) of 300 images each one. Assuming

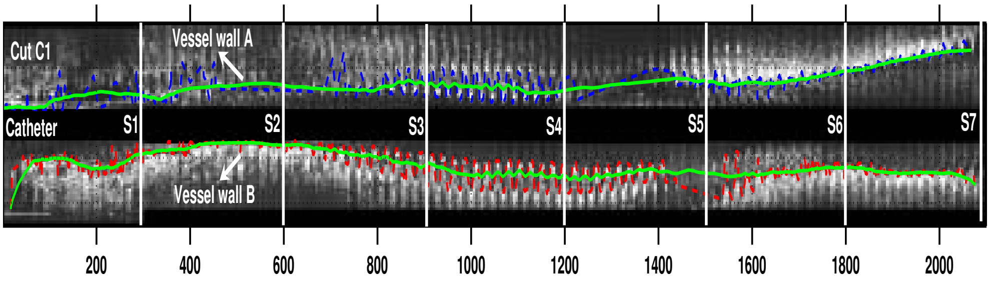

Figure 4.5: IVUS longitudinal cut $C1$.

isotropic elastic properties of the vessel wall, we take the lumen center temporal evolution along the sequence as the main descriptor of vessel displacement. The lumen centers were estimated as the centers of an elliptical approximation to the vessel wall points. Figure 4.7 shows the grey level average in temporal direction from subsequences S4 and S5 and their corresponding lumen center temporal evolution. The

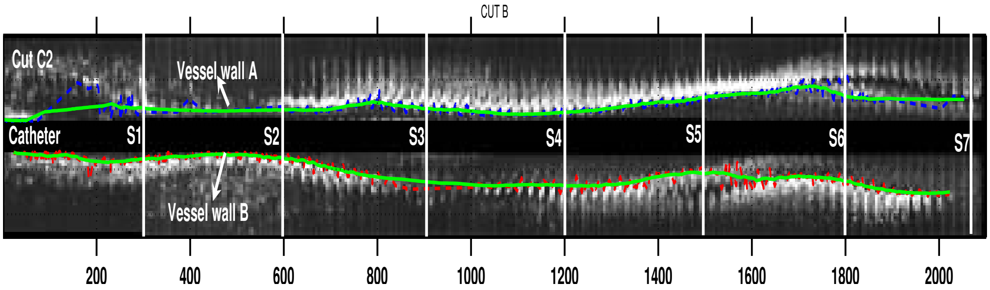

Figure 4.6: IVUS longitudinal $C2$.

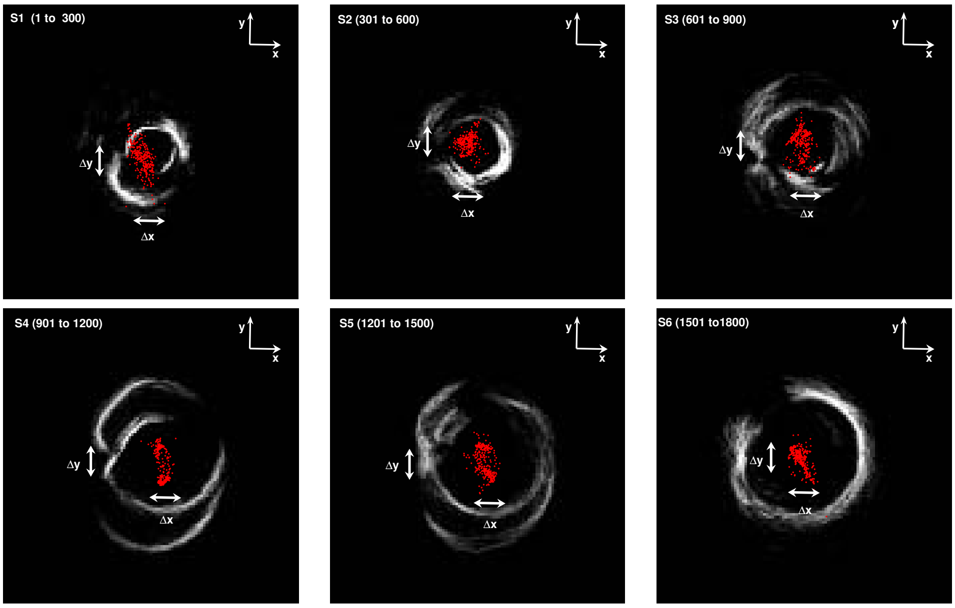

Figure 4.7: Grey level average and lumen center coordinates $(\Delta x, \Delta y)$ evolution along segments $S1$ to $S6$

lumen center spatial variation, $(\Delta x, \Delta y)$, is a main geometric measure that provides with relevant information on heart dynamics and geometric contributions to the IVUS rotation effect. Figures 4.8 (a) and (b) show the spatial evolution of the lumen center coordinates temporal evolution, Δx and Δy respectively. As in the profile of Fig. 4.5, the evolution profile of the vessel center also decomposes into two main curves: the cardiac periodic oscillation (blue line) and the base curve (red thick line) representing vessel wall position. Their corresponding power spectral density Fig. 4.8 (c) and (d) reflects these two main phenomena, as there are two predominant frequency ranges. Low frequencies in the range $[0.02, 0.33]$ Hz correspond to the systematic lumen center spatial evolution coming from the vessel morpho-geometric characteristics.

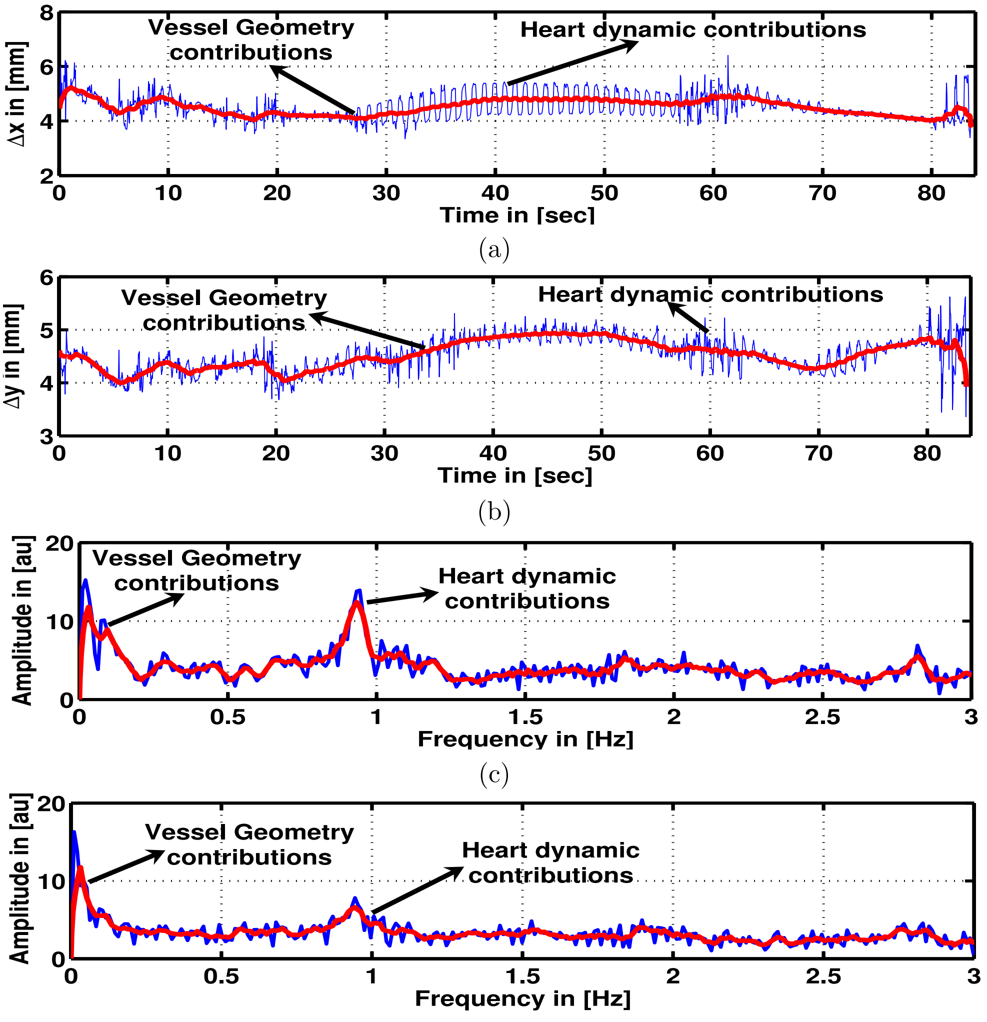

(a)

(b)

(c)

(d)

Figure 4.8: Lumen center Δcx and Δcy coordinates temporal evolution ((a) and (b)) and their corresponding Fourier spectrum ((c) and (d)). The geometric contributions and the heart dynamic contributions are displayed in red and blue respectively.

Meanwhile, those frequencies in located at $[0.78, 0.91]$ Hz are the heart dynamics contributions. By the above considerations, we conclude that the lumen center temporal evolution $(\Delta cx, \Delta cy)$ admits a linear decomposition into geometric and dynamical contribution terms:

$$\Delta cx = \Delta cx_g + \Delta cx_d \quad , \quad \Delta y = \Delta cy_g + \Delta cy_d \tag{4.4}$$

where Δcx_g,Δcy_g, Δcx_d, Δcy_d are the geometrical and dynamical spatial and temporal evolution of the lumen center respectively. Furthermore, each term can be written as a Fourier series:

$$\Delta cx_g(t) = \sum_{n=n_1}^{n=n_2} \big(A_n^x cos(n\omega t)+B_n^x sin(n\omega t)\big),\ \Delta cy_g(t) = \sum_{n=n_1}^{n=n_2} \big(A_n^y cos(n\omega t)+B_n^y sin(n\omega t)\big) \tag{4.5}$$

$$\Delta cx_d(t) = \sum_{n=n_3}^{n=n_4} \big(C_n^x cos(n\omega t)+D_n^x sin(n\omega t)\big),\ \Delta cy_d(t) = \sum_{n=n_3}^{n=n_4} \big(C_n^y cos(n\omega t)+D_n^y sin(n\omega t)\big) \tag{4.6}$$

where $(A_n^x, B_n^x, C_n^x, D_n^x, A_n^y, B_n^y, C_n^y, D_n^y)$ are the Fourier coefficients in the selected range intervals $[n_1, n_2)$ by geometric contributions and $[n_3, n_4]$ by heart dynamics contributions and ω is the fundamental frequency corresponding to cardiac frequency. Since the above argumentations also apply to vessel rotation, the angle of rotation, $\Delta\alpha$, will also be decoupled into geometric and dynamic terms:

$$\Delta\alpha_g(t) = \sum_{n=n_1}^{n=n_2} \big(A_n^\alpha cos(n\omega t) + B_n^\alpha sin(n\omega t)\big) \tag{4.7}$$

$$\Delta\alpha_d(t) = \sum_{n=n_3}^{n=n_4} \big(C_n^\alpha cos(n\omega t) + D_n^\alpha sin(n\omega t)\big) \tag{4.8}$$

These Fourier coefficients give the heart dynamics and geometric contributions amplitudes to vessel motion and play a central role in the simulation of vessel dynamic profiles (see experimental Section 4.4).

4.1.3 Vessel Wall Eccentricity and Catheter Obliquity.

Current IVUS techniques assume that the vessel is circular, the catheter is located in the center of the artery, and the transducer is parallel to the long axis of the vessel. However, both transducer obliquity and vessel curvature can produce an image giving the false impression that the vessel is elliptical. The transducer obliquity is especially important in large vessels and can result in an overestimation of dimensions and a reduction in image quality [35]. In order to find the catheter obliquity influence over the vessel wall eccentricity, we segmented an IVUS sequence of 2090 frames. An elliptical fitting to the vessel wall point find out by the Neural Network procedure, was made applying the algorithm described by [52]. The eccentricity of adjusted ellipses, was calculated as:

$$\epsilon = \sqrt{(a^2 - b^2)/a^2} \tag{4.9}$$

where a and b are the major and minor ellipse radii respectively. The change induced by the catheter obliquity on real vessel wall eccentricity, can be observed in an evolution profile of vessel wall eccentricity. Figure 4.9 (a) shows that the eccentricity ϵ exhibits a profile that can be written as:

$$\epsilon = \epsilon_g + \epsilon_d$$

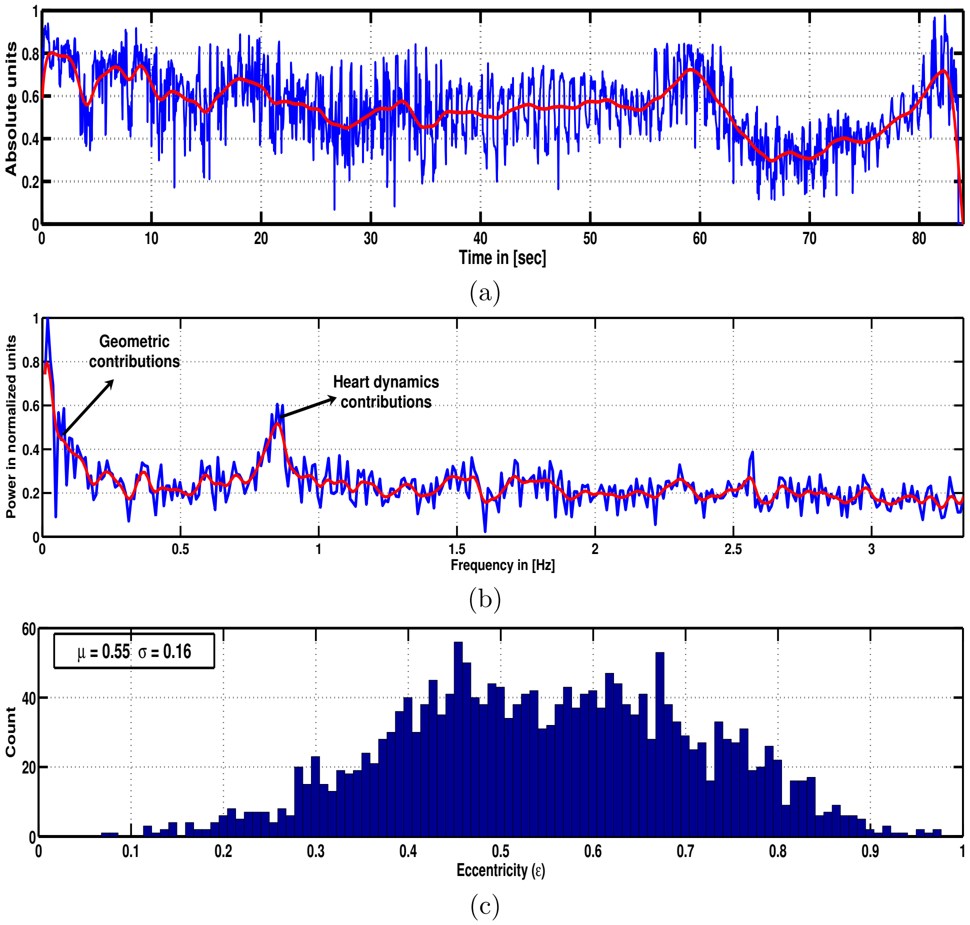

(a)

(b)

(c)

Figure 4.9: Eccentricity ϵ (a) temporal evolution its spectral density (b) and its corresponding histogram (c)

modelled as a Fourier series:

$$\epsilon_g(t) = \sum_{n=n_1}^{n=n_2} \left(A_n^{\epsilon} cos(n\omega t) + B_n^{\epsilon} sin(n\omega t)\right) \tag{4.10}$$

$$\epsilon_d(t) = \sum_{n=n_3}^{n=n_4} \left(C_n^{\epsilon} cos(n\omega t) + D_n^{\epsilon} sin(n\omega t)\right) \tag{4.11}$$

$\epsilon_g(t)$ and $\epsilon_d(t)$, are the principal eccentricity components corresponding to real vessel wall eccentricity, that come from vessel wall geometric properties and the pulsatile eccentricity induced by the catheter oscillating obliquity respectively. Fig. 4.9 (b) shows a spectral density, where it is possible to observe that the geometric contribution ϵ_g given by low frequencies in the spectrum, being its range values $[n_1, n_2]$,

$(0.02 \leq f \leq 0.33)$ Hz, and the dynamical contribution ϵ_d ranges $[n_3, n_4]$ is given in the frequency interval $(0.78 \leq f \leq 0.91)$ Hz, coincident with typical values of heart rate. The Fourier coefficients A_n, B_n, C_n, D_n are obtained directly from spectral density of experimental data.

The eccentricity histogram (Fig. 4.9 (c)) shows a symmetric temporal distribution of ϵ. This result means that the evolution of the real vessel wall eccentricity performs a pulsatile movement around mean value $\mu \approx 0.55$, with a standard deviation of σ 0.15, due to the heart dynamics contributions. With these results we can estimate the importance relative between the pulsatile eccentricity ϵ_d and the real eccentricity ϵ_g, as: $\eta = (\sigma/\mu) \times 100 \approx 27\%$ for a large sequence of a patient.

We extended this analysis to 30 patients of 300 frame each one which were segmented using the neural network procedure. The vessel wall ellipses approximation was applied using the procedure described by [52] and compared their major (a) and minor (b) radii magnitude by defining the absolute difference between major and minor ellipse radii as $\Delta R = |a - b|$ and the relative importance $\eta = |\sigma/\mu| \times 100$ in percentage. Figure 4.10 gives the histogram of absolute difference ΔR. The mean value of the absolute difference is $(\mu = 0.32 \pm 0.19)$ mm or $\approx (8 \pm 5)$ pixels. The ϵ histogram shows a normal distribution (See Fig. 4.11), centered at $\mu \approx 0.51$ and standard deviation $\sigma \approx 0.13$, consequently the relative importance between ϵ_g and ϵ_d is given by, $\eta = |\sigma/\mu| \times 100 \approx 26\%$. We can conclude that the oscillating variability on the

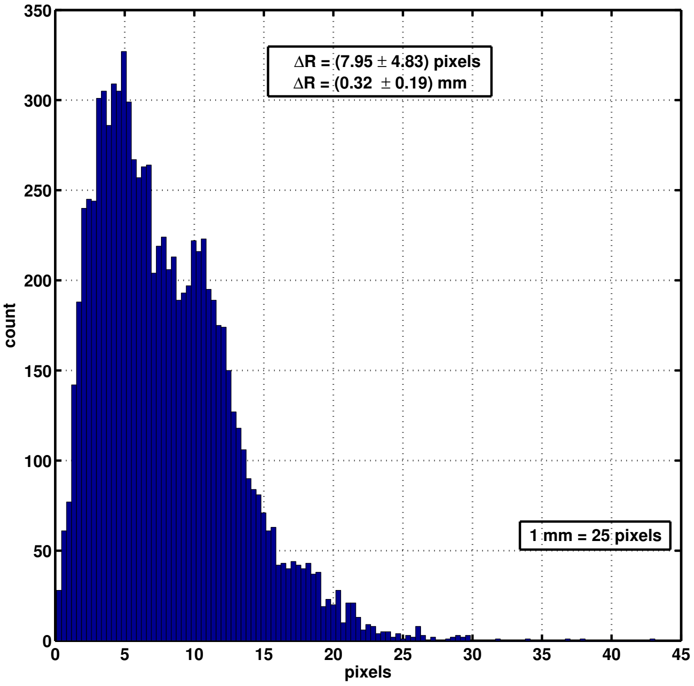

Figure 4.10: Histogram of absolute differences (ΔR), between major and minor vessel wall radii of adjusted ellipses.

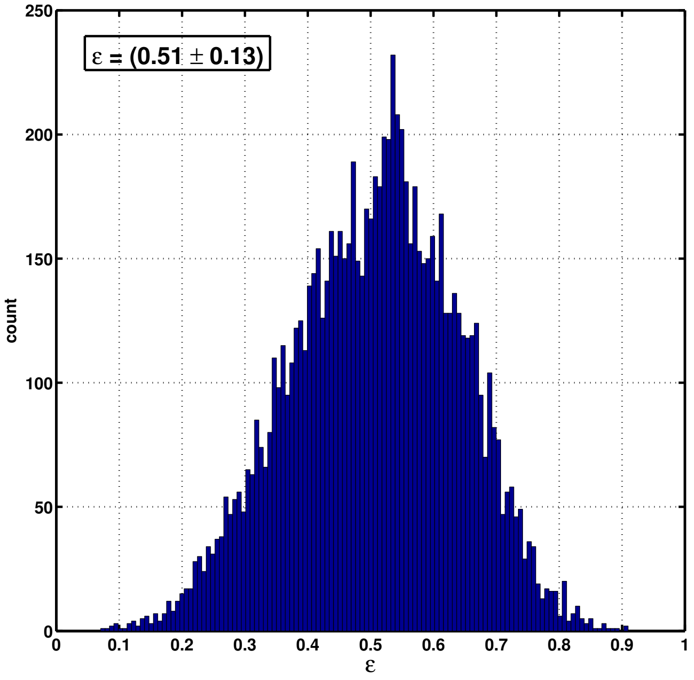

Figure 4.11: Ellipses eccentricity (ϵ) distribution

real vessel eccentricity ϵ, caused by changing the catheter obliquity, has a significative influence on the geometric description of the vessel wall temporal evolution. Therefore this pulsatile effect can not be neglected.
Due to the functional dependence between ellipse eccentricity ϵ and ellipses axis (See Eq. 4.9), we can use the eccentricity temporal behavior to describe the temporal evolution of major $a(t)$ and minor $b(t)$ ellipses axis as follows:

$$a(t) = a_g(t) + a_d(t) \quad , \quad b(t) = b_g(t) + b_d(t) \tag{4.12}$$

where ($a_g(t)$,$b_g(t)$) and ($a_d(t), b_d(t)$) are the major and minor geometrical and dynamical ellipses axis temporal evolution. These contributions are given as a Fourier series:

$$a_g(t) = \sum_{n=n_1}^{n=n_2} \left(A_n^a cos(n\omega t) + B_n^a sin(n\omega t)\right) \tag{4.13}$$

$$b_g(t) = \sum_{n=n_1}^{n=n_2} \left(C_n^b cos(n\omega t) + D_n^b sin(n\omega t)\right)$$

$$a_d(t) = \sum_{n=n_3}^{n=n_4} \left(A_n^a cos(n\omega t) + B_n^a sin(n\omega t)\right) \tag{4.14}$$

$$b_d(t) = \sum_{n=n_3}^{n=n_4} \left(C_n^b cos(n\omega t) + D_n^b sin(n\omega t) \right) \tag{4.15}$$

The Fourier coefficients $(A_n, B_n, C_n, D_n, A_n^\epsilon, B_n^\epsilon, C_n^\epsilon, D_n^\epsilon, A_n^a, B_n^a, C_n^a, D_n^a, A_n^b, B_n^b, C_n^b, D_n^b)$ in the range interval $[n_1, n_2]$ for geometrical contributions and $[n_3, n_4]$ for dynamical contributions, are obtained from a similar analysis realized to $a(t)$ and $b(t)$ temporal evolution using its power spectral density such is displayed in Fig. 4.9 (b).

4.2 A Geometric and Dynamical Vessel Motion Modelization.

By the analysis of the evolution profiles extracted from real data we can assume that the overall dynamics of vessel wall shape come from internal factors due to vessel intrinsic properties, external factors due to ventricle dynamics, and dynamical factors due to catheter movement. The main assumptions in the proposed model are the following:

1. The catheter oscillating obliquity given by (Eq. 4.14 and 4.15) will not be taken into account.
2. Radial deformation caused by blood pressure is negligible, compared to the vessel radius.
3. If scaling is negligible, vessel wall shape evolution can be described as a rigid transformation, that is, a rotation plus a translation.

Besides, the Fourier decomposition of the real data profiles shows that there are two relevant contributions to the motion of IVUS images:

- **A periodic motion** that comes from heart dynamics and periodically changes the lumen center.
- **A systematic motion** caused by vessel geometry properties. The systematic rotation changes progressively the lumen center with respect to the catheter, considered as its center origin of coordinates.

The above assumptions on vessel dynamics and the elliptical shape of vessel cross sections simplify the formulation of vessel motion to describing a rigid transformation of an elliptical vessel wall shape. Figure 4.12 (a) show the geometric parameters used to describe a vessel wall temporal evolution. The vessel wall at time t_1, $\gamma_1 = (x_1, y_1)$, can be written as follows:

$$x_1 = a(t_1)cos(\theta + \delta_1) + cx_1 \ , \qquad y_1 = b(t_1)sin(\theta + \delta_1) + cy_1$$

where $0 < \theta \leq 2\pi$, determines the angular position of the corresponding point on the ellipse, $(a(t_1), b(t_1))$ are the minor and major radii of the ellipse at time t_1, given by

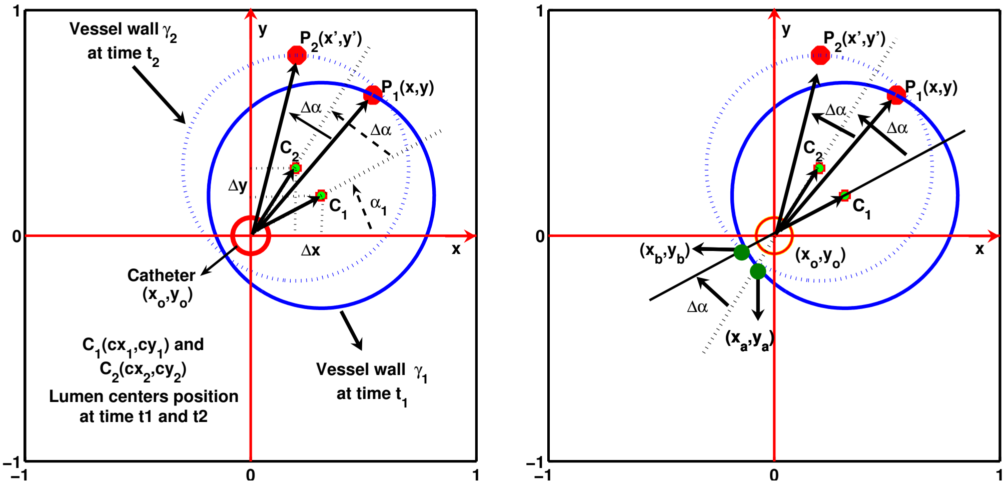

(a) (b)

Figure 4.12: Geometric parameters used in the model (a). Rotation angle α estimation method (b)

(Eq. 5.5), δ_1 is its orientation and $C_1 = (cx_1, cy_1)$ its center. We assume that the lumen center C_1 of γ_1 can be changed from position (cx_1, cy_1) at time t_1 to C_2 with position (cx_2, cy_2) at time t_2 due to the periodic heart movement. Therefore, the new center position C_2 of the elipse at time t_2 can be written as:

$$cx(t_2) = cx(t_1) + \Delta x_1, \;\; cy(t_2) = cy(t_1) + \Delta y_1 \tag{4.16}$$

where Δx_1 and Δy_1 gives the geometric and dynamical change induced by the vessel geometry and heart pulsatile contribution on the lumen center spatial and temporal evolution, given by equations (4.5 and 4.6). When changing to the new lumen center, a new rotated vessel wall $\gamma_2(x_{k+1}, y_{k+1})$ is given, whose coordinates have changed an angle α, using the catheter as rotational center. The new vessel wall coordinates can be written as:

$$\begin{pmatrix} x_{k+1} \\ y_{k+1} \end{pmatrix} = \begin{pmatrix} cos(\alpha(t_k)) & sin(\alpha(t_k)) \\ -sin(\alpha(t_k)) & cos(\alpha(t_k)) \end{pmatrix} \begin{pmatrix} x_k \\ y_k \end{pmatrix} \tag{4.17}$$

From figure 4.12 (b) we can see that $\alpha(t)$ can be written as $\alpha(t) = \alpha(t_1) + \Delta\alpha$. Where $\Delta\alpha$ is given by:

$$\Delta\alpha = \alpha_2 - \alpha_1 \tag{4.18}$$

From figure 4.12 (a) we can see that, $\alpha_1 = \arctan(cy_1/cx_1)$ and $\alpha_2 = \arctan(cy_2/cx_2)$.

4.3 Procedure for Rotation/Displacement Suppression of IVUS Images.

In order to quantify the rotation-displacement effect, an elliptical approximation to vessel wall should be found using the methodology described by [52]. In this section we describe the general procedures for computation of such vessel geometric representation and its use in the estimation of dynamical parameters.

4.3.1 Geometric Parameters. A Neural Network Approach to Detect the Vessel Wall.

For the computation of a vessel elliptical representation, structures on vessel wall along the sequence must be located. The detection of the vessel wall is based on physical parameters that characterize the intima, media and adventitia layers. Such descriptors are defined by global and local image grey-level properties obtained from IVUS images in polar form [51] with the origin at the catheter center. In this coordinate system, the image intensity, namely I, depends on the pixel distance (radius r in polar coordinates) to the ultrasound transducer [45, 32]:

$$I(r) = I_0 exp\big(-\zeta N_\theta f r\big)$$

The decrease in the initial beam intensity, I_0, is exponentially proportional to the absorption coefficient ζ, the frequency of the ultrasound ,f and the particle size or scatterer number, N_θ, located along the ultrasound beam path. The absorption coefficient gives the rate of diminution with respect to the distance along a transmission path [45] and it is locally obtained from the regression line slope [32] of the image profile (Fig.4.13). The set of characteristics chosen to find points on the vessel wall are the absorption coefficient ζ, image pixel grey level $I(r)$ and radial standard deviation σ and mean μ of the data. The absorption coefficient gives local information about the lumen-vessel transition acting as an edge detector. The statistics considered (σ and μ) contains global information on vessel structures: σ gives the global textural information and μ gives the baseline of global grey level intensity. In order to find potential candidate structures on vessel wall, a Perceptron Multilayer Neural Network

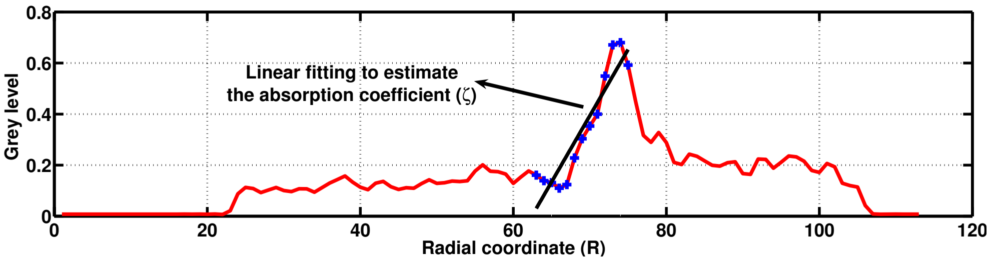

Figure 4.13: Radial grey level intensity to estimate the absorption coefficient ζ

(60 : 50 : 60 : 30) was trained using a standard Back Propagation Algorithm [30]. Figure 4.14 shows an example of positive (+) corresponding to intima and negative (-) patterns, corresponding to blood, adventitia, shadows and artifact zones. Finally, the elliptical approximation to the vessel wall points found by the Neuronal Network was adjusted using the method described in [52]. Figure 4.15 shows some of the vessel models obtained. Yellow points correspond to points found by the Neural Network segmentation and the solid red line to the fitted ellipse. The catheter center has been labelled with C and the ellipse centers with Lc (See Fig. 4.15). In order to analyze the neuronal network segmentation results, the quadratic error ϵ defined as the Euclidean distance, $\epsilon = ((x^m - x^r)^2 + (y^m - y^r)^2)^{1/2}$ between manual spatial location (x^m, y^m) of intima and spatial location (x^r, y^r) determined by the Neural Network algorithm has been computed for 4 validated sequences. Figure 4.16 (a) shows the quadratic error between validated spatial position of vessel wall (intima and media) and the spatial position estimated by the neural network algorithm. Figure 4.16 (b) gives the quadratic error between adjusted ellipse points and the spatial points determined by the neural network from figure 4.15. The mean error is $\mu \approx 8.5$ pixels (≈ 0.34 mm) and a standard deviation of ≈ 9.1 $pixels$ (≈ 0.36 mm). The estimated mean of error between ellipse fitting and vessel wall point determined by the neural network is $\mu \approx 4$ pixels (≈ 0.16 mm) with a standard deviation $\sigma \approx 4.0$ pixels (≈ 0.16 mm). Although the above results indicate that our segmentation is far from vessel wall detection algorithms accuracy, it serves to correct vessel motion. The main reason is that for estimation of vessel dynamics, it suffices to study the global motion of the structure which is mechanically fixed to the vessel wall. The vessel structures comprised in the intima-adventitia borders range are, approximately $10-15$ pixel thick. Therefore our model lies within the range admitted in our geometric-physical modelization of vessel dynamics.

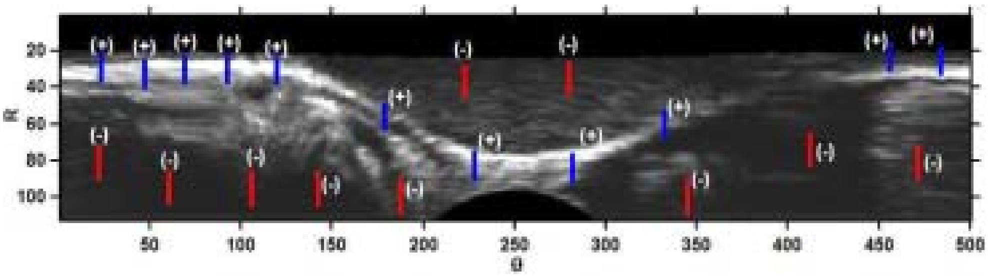

Figure 4.14: Polar IVUS image used to extract positive (+) and negative (-) patterns.

4.3.2 Motion Parameters.

Once defined the catheter as rotation center of the sequence, it is necessary to estimate the angular rotation profile of vessel wall structure. In a rotation, it is sufficient to provide the temporal evolution of a single point on the vessel wall structure [42, 44], to measure the angular difference between two consecutive frames. The ultrasound

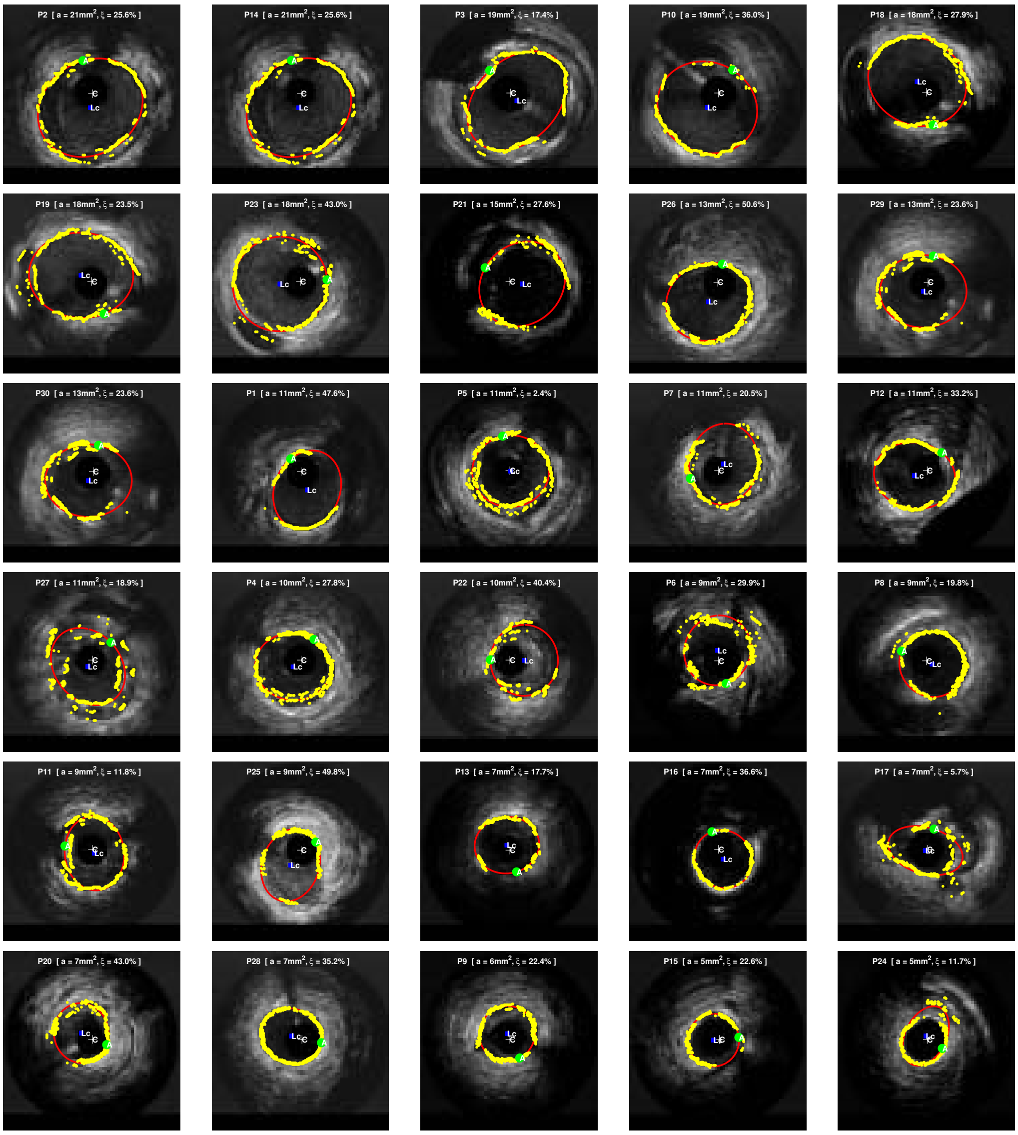

Figure 4.15: Neuronal network segmentation results of 30 patients. *Lc* is lumen center, *C* catheter center and *A* ellipse point located at minimal distance to the catheter. a is the lumen area and ξ is the catheter eccentricity.

intensity decrees gradually in radial direction, also the best visibility structure point on the vessel wall are the points nearest to the catheter center [43, 51]. Therefore, spatial location of this reference point was determined as the position (x_k^a, y_k^a) in frame k and (x_{k+1}^a, y_{k+1}^a) in frame $k+1$ on the vessel structure (See Fig. 4.12 (b)), that has

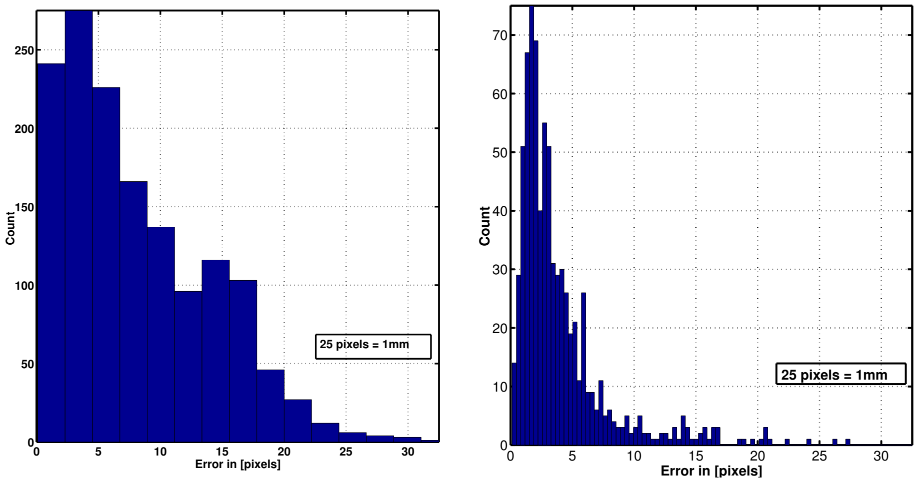

(a) (b)

Figure 4.16: Error (ϵ) between vessel wall spatial position done by an expert and vessel wall spatial position determined by neural network procedure (a). Error (ϵ) between adjusted ellipse and vessel wall point (Fig. 4.15) determined by the neural network (b).

minimal Euclidean distance to the catheter center $C-->(x_o,y_o)$. The distance criterion can be written as follows:

$$(x_k^a, y_k^a) = argmin_{ij}((x_o - x_{k,i})^2 + (y_o - y_{k,i})^2)^{1/2}$$

where (x_0, y_0) are the catheter coordinates, and $x_{k,i}, y_{k,i}$ are the vessel wall coordinates given by Eq. 4.17. The rotation profile can be written as:

$$\alpha(t_k) = \alpha_0 + \Delta\alpha_k \tag{4.19}$$

where $\alpha_0 = \arctan(y_0^a/x_0^a)$ is the reference angle corresponding to initial frame, and $\Delta\alpha_k = \arctan(y_k^a/x_k^a)$, is the rotation angle for frame k.

4.3.3 IVUS Rotation Suppression.

The suppression of the rotation is given by the following linear transformation: The actual image frame $I_k(x,y)$ (Fig. 4.17 (a)) is translated by (cx_k, cy_k) to center the ellipse on the catheter center, following by a rotation through an angle $-\alpha_k$:

$$\begin{pmatrix} x_k' \\ y_k' \end{pmatrix} = \begin{pmatrix} cos(-\alpha_k) & sin(-\alpha_k) \\ -sin(-\alpha_k) & cos(-\alpha_k) \end{pmatrix} \left(\begin{pmatrix} x_k \\ y_k \end{pmatrix} - \begin{pmatrix} cx_k \\ cy_k \end{pmatrix} \right) \tag{4.20}$$

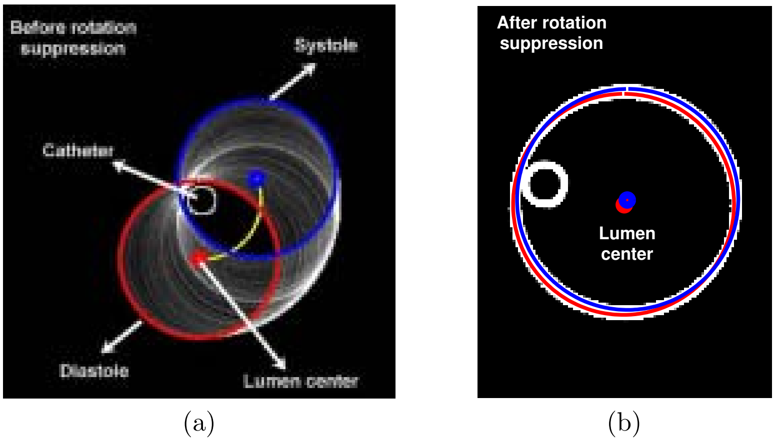

(a) (b)

Figure 4.17: The original image (a) is translated to center the ellipse in the catheter center and rotated through an angle $-\alpha_k$ (b).

where (x'_k, y'_k) and (x, y) are the new and old cartesian image coordinates, α_k is the rotation angle and (cx_k, cy_k) is the elliptical center. By applying sequentially this equation, we align all frames with the first frame of reference (Fig. 4.17 (b)). Summarizing, the procedure for rotation suppression consists of:

- Vessel wall detection by the Neural Network and its elliptical approximation
- Reference point detection and estimation of its rotation along the image sequence
- Correction of image rotation and displacement using the extracted parameters of the elliptical approximation

4.4 Validation and Results

Given that the intention of our work is to use the geometric model to explain the "saw-tooth-shaped" longitudinal vessel appearance in IVUS data and to remove it from the image sequences, we plan the following set of experiments:

1. Robustness of the estimation of motion parameters.
2. Determining a reliable quantification of movement suppression in real data.
3. Assessment of our geometric model in real data.
4. Healthy and pathological rotation profiles.

4.4.1 Robustness of the Estimation of Motion Parameters.

In real data, goodness of motion correction can not be assessed by straight difference methods. The existent bibliography and our previous study of vessel profiles (Section4.1) selects longitudinal cuts shape as the best candidate to quantify the degree of vessel movement in real sequences. Shape appearance of a longitudinal IVUS cuts depends on vessel wall geometry and catheter eccentricity caused by the catheter movement and the heart dynamics contributions.

The obtained parameters values from real IVUS sequences, can be used in our model to obtain in simulated form the influence of heart dynamics and vessel geometry contributions to the image rotation effect (See section 4.2). The first intention of this work is to use our geometric model to explain the longitudinal IVUS cut shape appearance, and finally to remove it from the image sequences. The summarized values necessary to simulate the data using our model are presented in table 4.1.

Parameter	**Units**	**Value**
Minor axis (a)	mm	3
Major axis (b)	mm	3
Orientation (δ)	degrees	0
Catheter center (cx)	mm	0
Catheter center (cy)	mm	0
Fourier coefficient in (x) (A_n^x, B_n^x, C_n^x, D_n^x)	mm	1
Fourier coefficient in (y) (A_n^y, B_n^y, C_n^y, D_n^y)	mm	1
Heart frequency (ω)	Hz	0.80

Table 4.1: Geometric and dynamic parameters used in the simulation model.

Steps to Obtain Vessel Wall Evolution.

When the catheter oscillating obliquity is neglected the vessel wall temporal evolution from catheter point of view can be described by the following steps:

1. An initial vessel wall using the catheter center (x_o, y_o) as origin of coordinates is generated (See Fig. 4.18 (a)).

2. A rotation profile $\alpha(t)$ given by (Eq. 4.19) (Fig. 4.19 (a) and (b)) is created as follows: Assuming a Fourier frequency at 0.8 Hz and fixed parameters A_n^x, B_n^x, C_n^x, D_n^x, A_n^y, B_n^y, C_n^y, D_n^y, we generated Δx and Δy (See Eq. 4.4)). It allows to determine the center position of our elliptical approximations using (Eq. 4.16). Finally, the rotation profile is obtained using equations (4.18) and (4.19). The result of adding heart dynamics contributions to vessel geometry is the sinusoidal blue line and the resulting geometric profile due to the catheter pullback in a straight vessel Fig. 4.19 (a) and tortuous vessel Fig. 4.19 (b) displayed by the red solid line. We generated the ellipses corresponding to the different temporal frames and obtained the vessel profiles in the simulated lon-

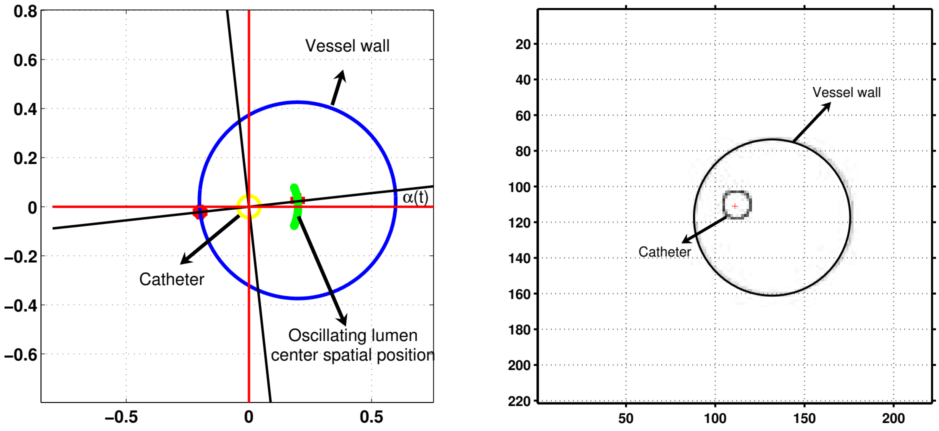

(a) (b)

Figure 4.18: The rotation profile $\alpha(t)$ give a spatial oscillation of the lumen center position (a). The generated vessel wall at time t is transformed into an image format (b)

gitudinal IVUS cuts. The parameters used in the simulation are given in table 4.1.

3. The vessel wall spatial evolution is obtained by applying the Eq. 4.17.

4. Once obtained the vessel wall position it is transformed into an image format (Fig. 4.18 (b)).

In this work, we are interested in the following cases:
A.- Straight vessel. In Figure 4.19 (a) only a sinusoidal rotation profile due to heart dynamics contribution is considered. The lumen center follows a parallel straight line to the catheter center. This case corresponds to two situations: First one, the catheter is static and second one the vessel is straight.
B.- Curved vessel. More realistic situation is displayed in figure 4.19 (b). In this case we consider mixed contributions: geometry and heart dynamics are simulated, the geometric contribution comes from catheter movement in a tortuous vessel.
A.-Straight vessel. Validation of rotation removing was done by analyzing the temporal evolution of rotation angles. It is considered that the rotation has been removed if the rotation angle profile after correction is constant to zero. There are several ways of testing the former hypothesis. **a.-** Longitudinal cut appearance. **b.-** Spatial evolution of the lumen center. **c.-** Rotation profile before and after rotation suppression. In next section the three ways are analyzed.

Longitudinal Cut Shape Appearance Before Rotation Suppression.

Shape appearance of a longitudinal IVUS cut depends on vessel wall geometry and catheter eccentricity caused by the catheter movement and the heart dynamics contributions. Figure 4.20 (a) and (b) show two simulated vessel wall images indicating the line reference that allows to obtain a longitudinal cuts views. Figure 4.20 (c) and (d) display two longitudinal cut views corresponding to a straight vessel, when the catheter eccentricity is 35 %. If the vessel is straight, a monotonic pulsatile longitudinal shape appearance in longitudinal cut $C1$ (a) can be observed. The oscillating shape profile is caused by the heart dynamics contributions. Figure 4.20 (e) and (f) display a view of the vessel wall shape in a longitudinal cut when a curved vessel and heart dynamics contribution are considered. In order to study the longitudinal cut shape appearance, before and after rotation suppression, 10 sequences (Fig. 4.21 first row) were simulated, varying the catheter eccentricity in the interval corresponds to $(0 \leq \xi \leq 1)$. The rotation profile $\alpha(t)$, used in this simulation, appears in Fig. 4.19 (b). The angle variation amplitudes correspond to a range of $-20 \leq \alpha \leq 20$ degrees. In (Fig. 4.21 first row) the positions $p1$ and $p10$ correspond to $\xi = 0.95$. Second row from figure 4.21 shows the grey level mean trough the temporal direction from catheter position $p1$ to position $p10$. One can observe an oscillating vessel shape that use the catheter as the rotation center. Position $p5$ corresponds to $\xi = 0$. In third and fourth rows two orthogonal cuts are displayed as shown in figure 4.20 (a) and (b). Vessel wall appearance in the longitudinal cut shows a sinusoidal profile whose frequency depends on the pulsatile rotation profile, but the amplitude depends on the catheter eccentricity, being this maximal when $|\xi| = 0.95$ and minimal when $|\xi| = 0$.

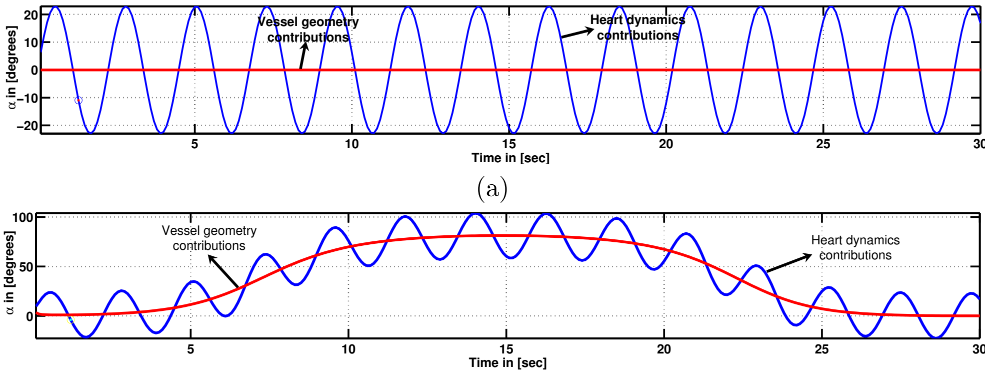

(a)

(b)

Figure 4.19: The sinusoidal rotation profile α(t) (a) only consider the pulsatile contribution that come from heart dynamics. A mixed rotation profile (b) that consider the vessel geometry and heart dynamics contributions.

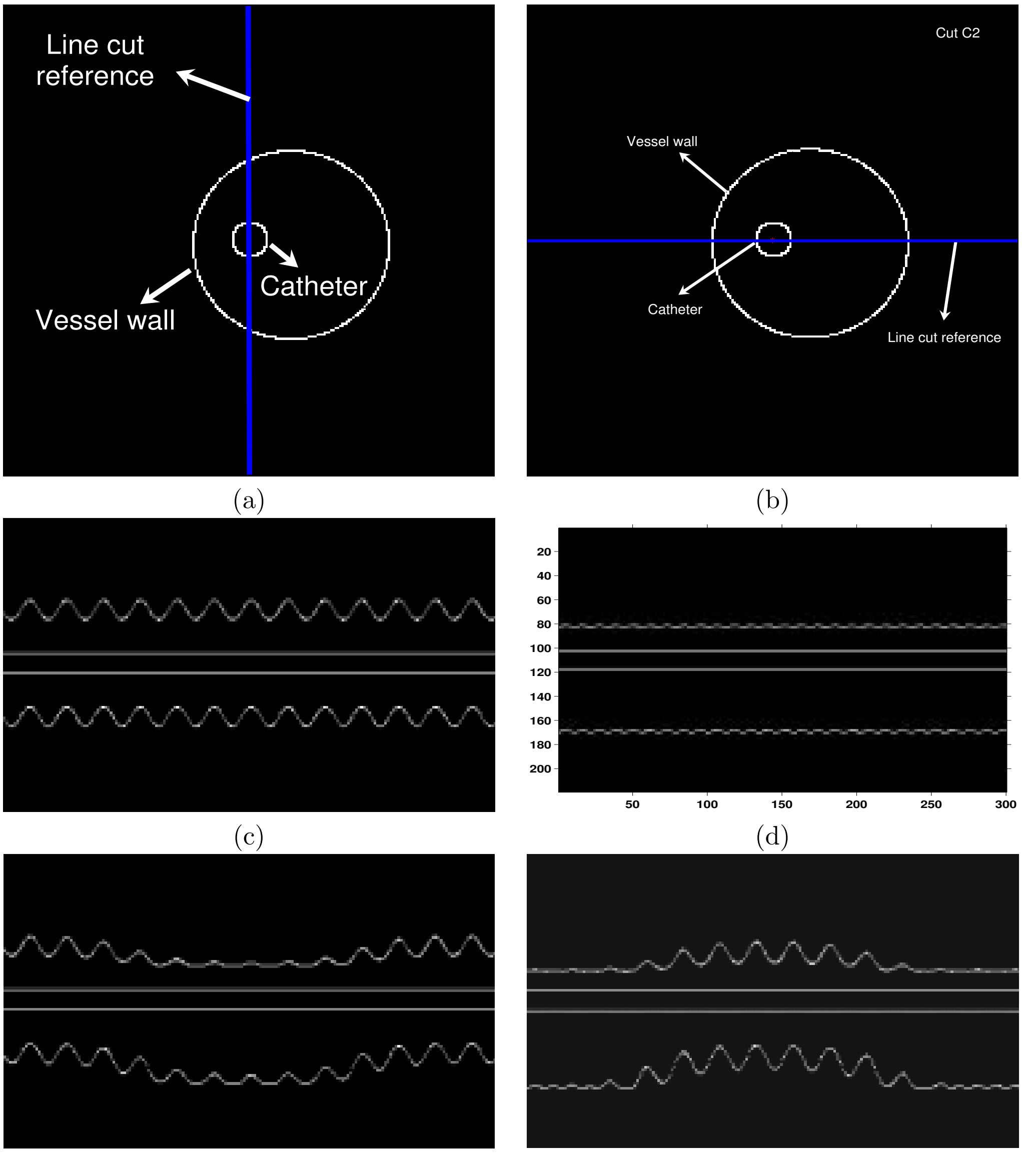

(a) (b)

(c) (d)

(e) (f)

Figure 4.20: Simulated vessel wall (a) and (b). Orthogonal cuts views considering a straight vessel (c) and a pulsatile heart dynamics contributions (d). Longitudinal cut shape appearance (e) and (f) when the vessel geometry and heart dynamics are considered.

Longitudinal Cut Shape Appearance After Rotation Suppression.

The rotation suppression method can be divided in two steps: **I.-** Once generated the simulated sequences we applied the procedure to estimate the rotation center,

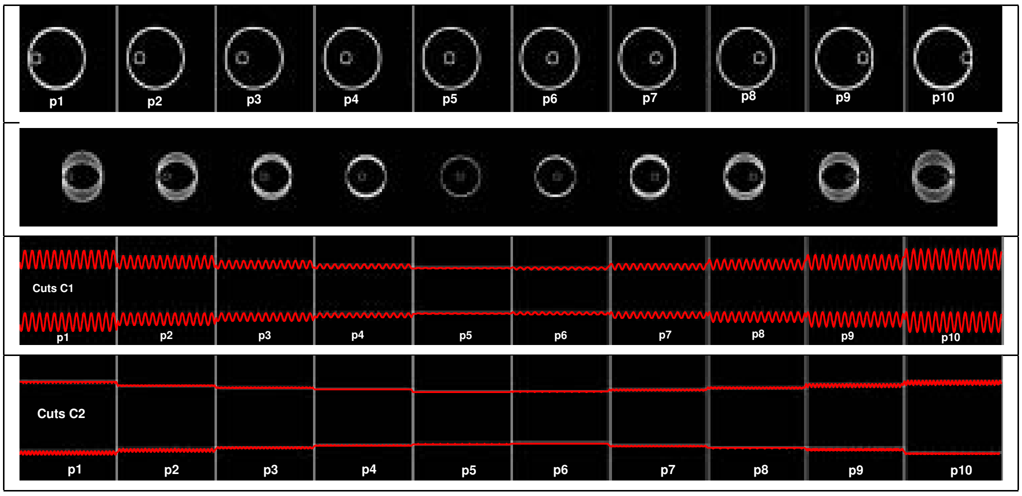

Figure 4.21: Before rotation suppression: Catheter spatial positions from position $p1$ to $p10$, first row. Row(2) are the grey level projection in temporal direction. Row(3) and (4) are longitudinal cuts before rotation suppression, referred to Fig. 4.20 (a) and (b).

according to section 4.3.2. To this purpose we generated 73 sequences of 300 images each one. The sequences were generated with different catheter eccentricity ξ values, being the range $0\% \leq \xi \leq 95\%$. We use the method to estimate the rotation angle in order to compare the estimated angle using the procedure described in section 4.3.2, versus the theoretic angle (Fig.4.22 (a)). Figure 4.22 (b) shows the linear coefficient m versus catheter eccentricity ξ. When the catheter is near to the lumen center $0 \leq \xi \leq 10$ % the linear coefficient m has a singularity due to the equidistance between the catheter center and the vessel wall points. Therefore the reference point used to estimate the rotation angle makes no sense. In this case it is necessary to use a complementary method based on a discrete description of vessel wall, that takes into account the total energy of vessel wall border [27] (See appendix A). Figure 4.22 (c) shows the error in degrees versus catheter eccentricity ξ. We can see that the error of estimating the angle, increments significatively when ξ is near to zero. **II.-** When the rotation profile is estimated, we applied the transformation described in section 4.3.3 in order to remove the rotation from the simulated sequences. Figure 4.23 first row from $p1$ to $p10$ permits to see the mean grey level images in temporal direction after rotation suppression.

4.4.2 Determining a Reliable Quantification of Movement Suppression.

In order to compare the method efficiency we compare the vessel wall shape before and after rotation suppression. Figure 4.24 (a) and (b) shows the longitudinal cut

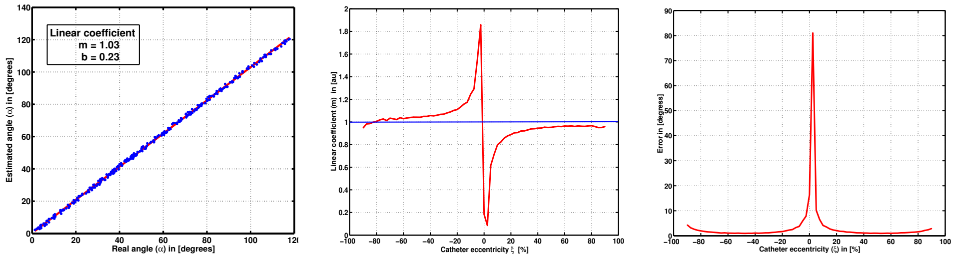

(a) (b) (c)

Figure 4.22: Theoretical vs. estimated rotation profile $\alpha(t)$ given by $\xi = 37.5\%$ (a). Linear coefficient m vs catheter eccentricity ξ (b). Error in degrees vs. catheter eccentricity ξ (b).

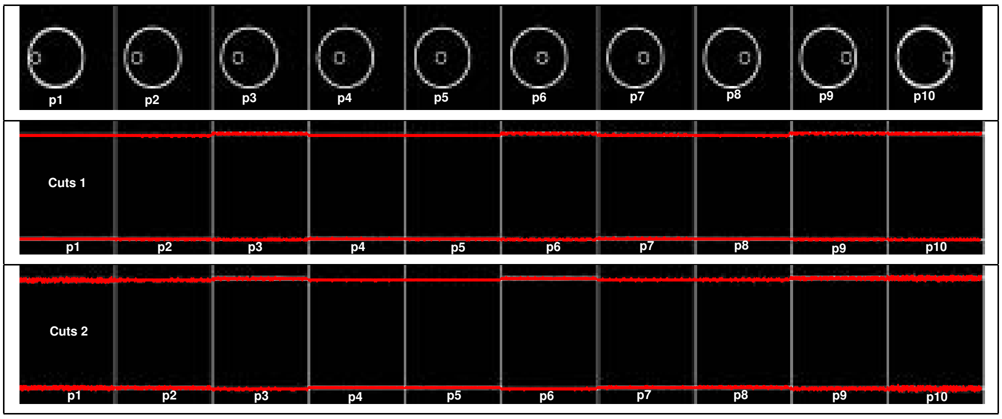

Figure 4.23: After rotation suppression. Mean of sequences in temporal direction, first row, second and third row longitudinal cuts referred to Fig. 4.20 (a and b).

before and after rotation suppression respectively. We define a quantitative measure based on Euclidean distance to verify that the rotation effect has been removed. The orthogonal Euclidean distance, Δd between the linear fitting to each one of vessel wall points was calculated (See Fig. 4.24 (a) and (b)). Figure 4.24 (c) and (d) display the corresponding Δd histogram before and after rotation suppression respectively. Before the rotation suppression the distance distribution Δd shows a great dispersion ≈ 0.5 mm standard deviation, after rotation suppression the standard deviation decrements to ≈ 0.1 mm, therefore the sinusoidal vessel wall shape has disappeared.

We have special interest to observe the behavior of Δd distribution when the catheter eccentricity changes. To this purpose the method described in 4.4.1 was used. Figure 4.25 (a) shows a mean of 300 images sequence in temporal direction by catheter eccentricity $\xi = 95\%$ before rotation suppression. The selected rotation profile $\alpha(t)$ in this particular case, only takes into account the heart contributions. The lumen center spatial position follows a circular segment, which after rotation suppression

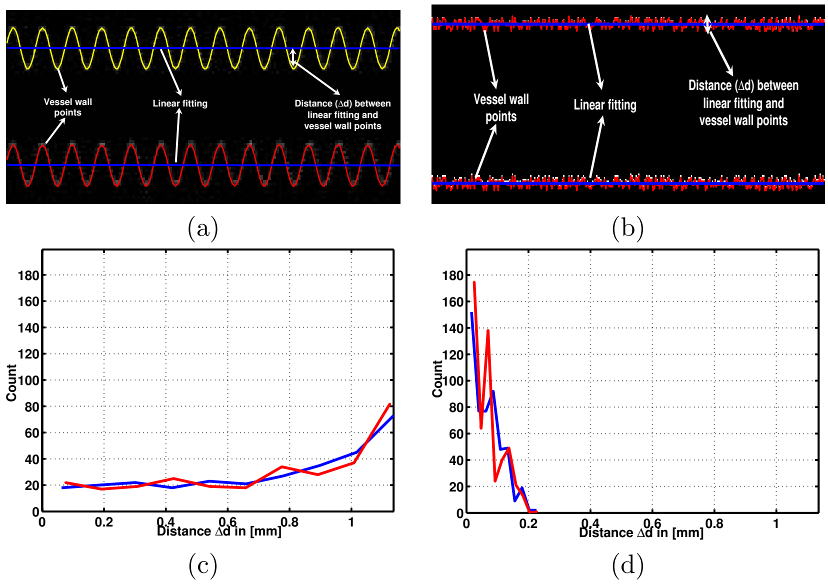

(a) (b)

(c) (d)

Figure 4.24: Longitudinal cuts before (a) and after (b) rotation suppression. The parameter Δd is defined as the Euclidean distance between the linear fitting and the vessel wall points. Δd histogram before (c) and after (d) rotation suppression.

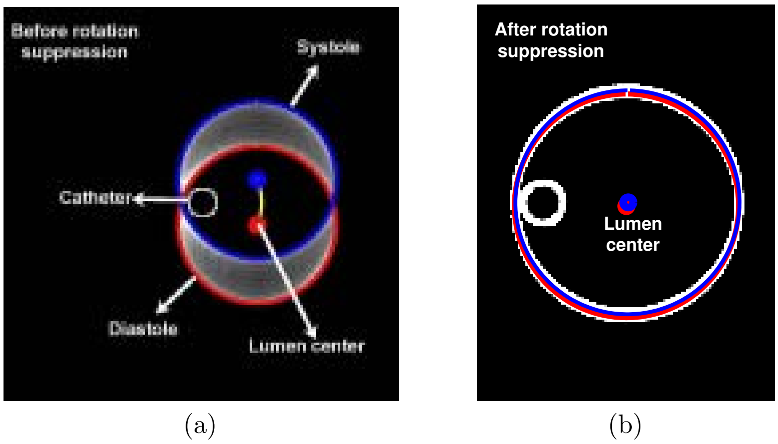

(a) (b)

Figure 4.25: Vessel wall before (a) and after (b) rotation suppression respectively.

(b) has a small spatial dispersion. The distance Δd versus catheter eccentricity ξ, before and after rotation suppression, is displayed in 4.26 (a). In this figure we can see that there is a linear dependence between the distance Δd and the catheter eccentricity ξ (See Appendix B). Using this result we would hope, that the IVUS rotation effect should be negligible when $\xi \approx 0$. This is an important result that

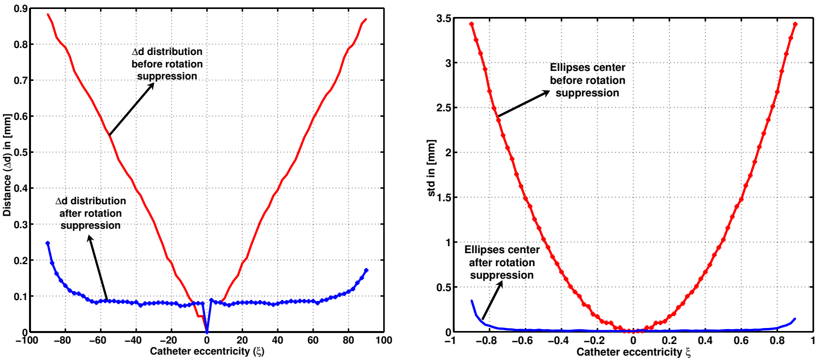

(a) (b)

Figure 4.26: Δd versus catheter eccentricity ξ (a) and lumen center spatial deviation, before and after rotation suppression respectively (b).

has physiological implications related to the vessel micro-architecture (See section 2.1). IVUS image rotation by $\xi \approx 0$ comes from intrinsical vessel rotation. Other quantitative measure that allows verifying that the rotation artifact has been removed, is the spatial evolution of lumen center before and after rotation suppression. Fig. 4.26 (b) shows the standard deviation of lumen center versus catheter eccentricity before and after rotation suppression. We can observe a quadratic dependence of lumen center standard deviation respect to the catheter eccentricity ξ.

Although we have not considered in this particular simulation, the catheter obliquity and the radial vessel wall inflation due to the blood pressure, a similar behavior is observed in real case (See Fig. 1.5 (a)).

B.-Curved vessel. In order to see a more realistic situation we consider a synthetic example where the geometric and dynamic contributions to the rotation profile $\alpha(t)$ are taken into account. We consider the rotation profile from figure 4.19 (b) that has a sinusoidal profile as dynamic contribution and a gaussian profile as geometric contribution.

Fig. 4.27 first row from position $p1$ to $p10$ shows 10 catheter spatial positions. Row(2) are the grey level projections of vessel wall in temporal direction for catheter position $p1$ to $p10$. Row(3) are the longitudinal cuts $C1$ and $C2$ before rotation suppression, refereed to Fig. 4.20 (a) and (b). Figure 4.28 displays longitudinal cuts $C1$ before (a) and after (b) rotation suppression. Δd histogram before and after rotation suppression are presented in (a) and (b) respectively. Figure 4.30 shows vessel wall before (a) and after (b) rotation suppression, Δd versus catheter eccentricity ξ (c) and lumen center spatial dispersion, before and after rotation suppression. Figure 4.31 show the behavior of the longitudinal cut appearance after rotation suppression. Row (1) display the mean of the sequences in temporal direction varying the catheter eccentricity, second and third row longitudinal shows the cuts $C1$ and $C2$ refers to Fig. 4.20 (a) and (b). We can see in this figure the decreasing of the oscillating behavior caused by the heart movement.

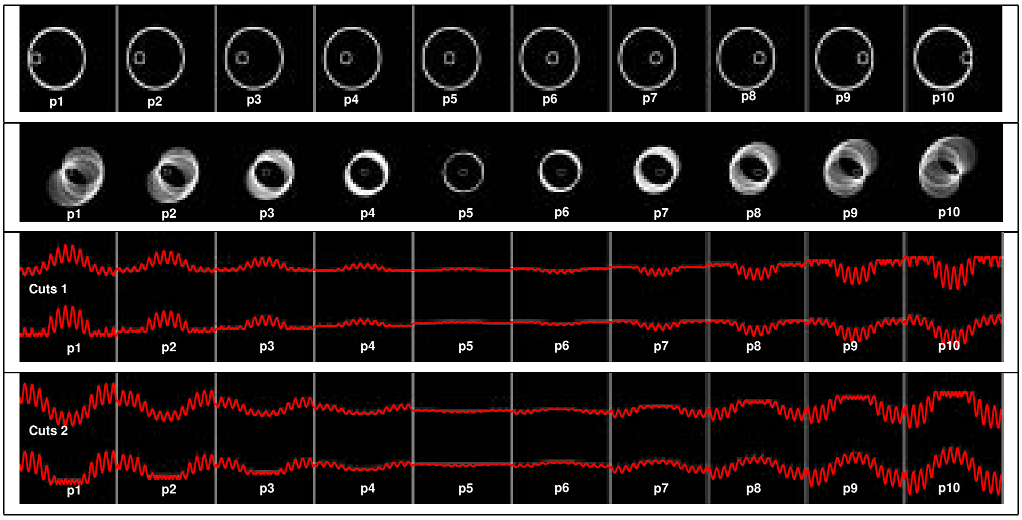

Figure 4.27: Catheter spatial positions $p1$ to $p10$ first row. Second row are the grey level mean sequences in temporal direction. Row(3 and 4) longitudinal cuts before rotation suppression, refereed to Fig. 4.20 (a and b).

4.4.3 Assessment of Our Geometric Model in Real Data.

In order to study the behavior of the reported motion suppression strategy we have analyzed 30 patients sequences of 300 images each one. Figure 4.32 displays the adjusted vessel wall ellipses and their corresponding centers before and after rotation suppression respectively. We note that the lumen center spatial variation has significantly reduced after image correction. Longitudinal cuts before and after rotation elimination are exhibited in Fig. 4.33. The first row shows 6 orthogonal longitudinal cuts of 300 images each before rotation suppression. The second row shows the corresponding longitudinal views after rotation suppression. The grey level shift decremented significantly so that bright structures stay still and the vessel wall shape appearance exhibits in some cases a straight line, in contrast to the wavy shape of original cuts. Our statistical analysis focuses on checking the robustness in parameter estimation as well as degree of movement removing. Robustness in the estimation procedure is assessed by computing parameters to original and corrected images.
The temporal evolution of the rotation angle before and after rotation suppression for 4 patients before and after removing the rotation artifact are shown in Fig. 4.34 and Fig. 4.35. We can observe in all cases that the rotation suppression has been very well removed, remaining only the rotation dispersion due to the segmentation algorithm precision. Figure 4.34 gives a case where only heart pulsatile contributions occur: a sinusoidal monotonic rotation profile is observed. Figure 4.35 display two cases where the pulsatile heart influence and the vessel geometric contributions are given. Before rotation suppression it is to observe a periodic and systematic rotation profile, caused by pulsatile heart contribution and vessel wall geometry. These rota-

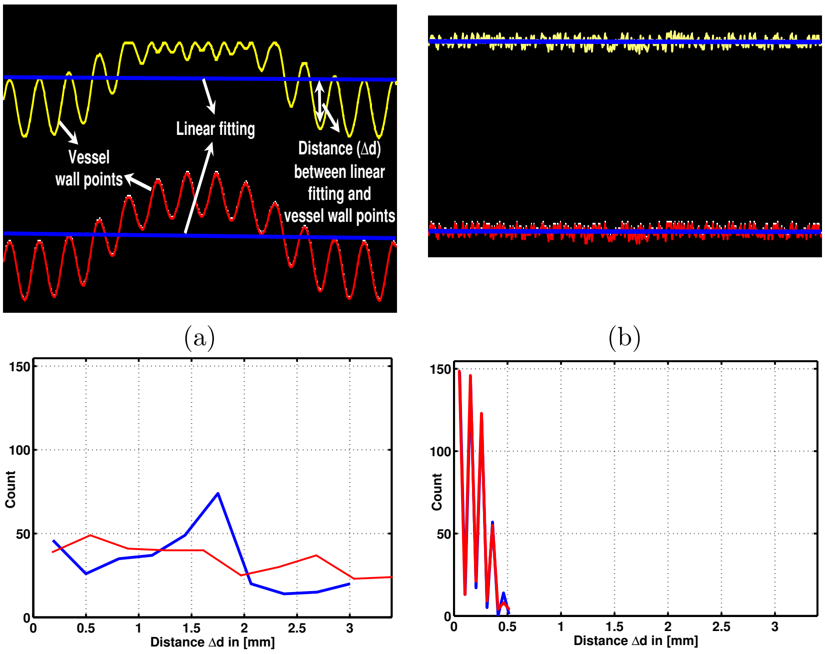

(a) (b)

(c) (d)

Figure 4.28: Longitudinal cut $C1$ before (a) and after (b), Δd histogram before (c) and after (d) rotation suppression respectively.

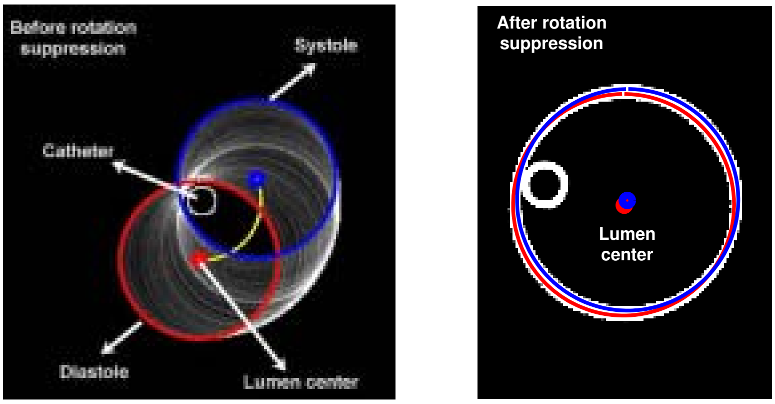

(a) (b)

Figure 4.29: Vessel wall (a) and after (b) before and after rotation suppression respectively.

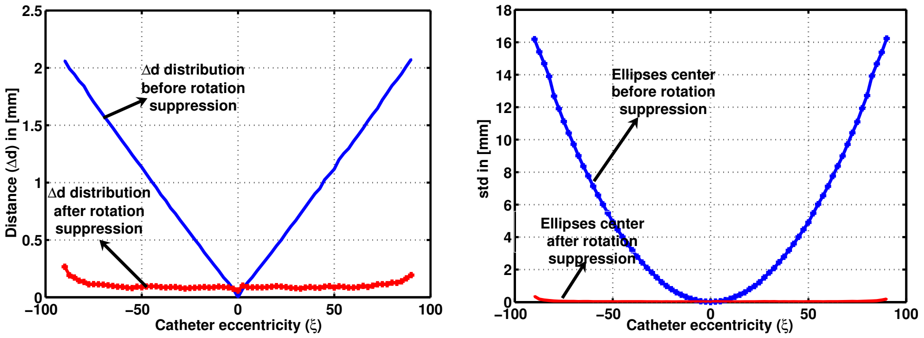

(a) (b)

Figure 4.30: Δd versus catheter eccentricity ξ (a) and lumen center spatial deviation (b), before and after rotation suppression respectively.

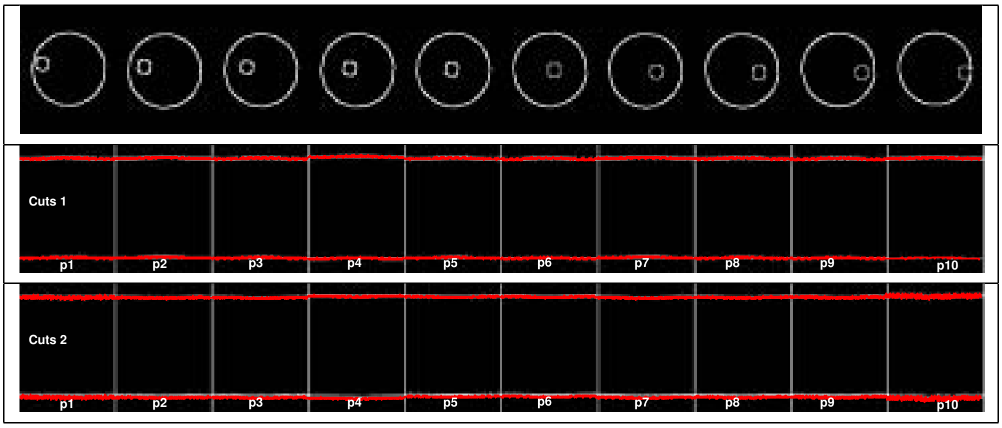

Figure 4.31: After rotation suppression. Row (1) mean of sequences in temporal direction, second and third row longitudinal cuts $C1$ and $C2$ referred to Fig. 4.20 (a and b).

tion profile behavior disappear when the rotation suppression procedure is applied. In next figures we summarize the reliability in parameter estimation for the 30 patients. The more important parameters to be evaluated are the following: lumen center evolution, deviation and average of rotation profile before and after rotation suppression, and distance distribution Δd. The standard deviation (Fig. 4.36) of the radial position of lumen centers, presents a significative decrement for all cases of $\Delta r \approx (2.3 \pm 3)\ mm$ to $\Delta r \approx (0.5 \pm 0.3)\ mm$. The standard deviation of rotation profile for 30 patients (Fig. 4.37 (a)) shows a decrement from $\sigma \approx (50 \pm 20)$ degrees before, to $\sigma \approx (18 \pm 8)$ degrees, after rotation suppression. The rotation mean (Fig. 4.37 (b)) show a decrement from $\mu \approx (30 \pm 10)$ degrees before, to $\mu \approx (5 \pm 5)$ degrees after rotation suppression. These results are a quantitative measure of goodness of